

Thermal Cycling Reliability of Doped SnAgCu Solder Alloys after Long-Term Aging

by

Francy John Akkara

A dissertation submitted to the Graduate Faculty of
Auburn University
in partial fulfillment of the
requirements for the Degree of
Doctor of Philosophy

Auburn, Alabama
May 1, 2021

Keywords: lead-free solder, reliability, thermal cycling, electronic assembly

Copyright 2021 by Francy John Akkara

Approved by

Sa'd Hamasha, Chair, Associate Professor of Industrial and Systems Engineering
John Evans, Charles D. Miller Endowed Chair of Industrial and Systems Engineering
Michael Bozack, Professor Emeritus of Physics Department
Gregory Harris, Associate Professor of Industrial and Systems Engineering
Vishwani Agrawal, Professor Emeritus of Electrical and Computer Engineering

Abstract

Eutectic SnPb (Tin-Lead) solder has been used in electronics since early days. This universal alloy combination was used in all soldering applications because it had good mechanical and electrical properties and hence had good reliability. But, by the end of 20th century, harmful effects of lead were identified. Since then the industry has been pushing toward lead free electronics. In 2000, the European Union put forward two directives towards lead free electronics. The Waste of Electrical and Electronic Equipment (WEEE) directive stipulated that lead should be removed from all electrical and electronic components at the end of life. The Restriction of Hazardous Substances (RoHS) directive prohibits the use of lead in electrical and electronic components manufactured after July 1, 2006. As a result of these and similar directives, the industry went through an intense search for replacements. Research led to a series of near eutectic alloys based on tin (Sn)-silver (Ag)-copper (Cu), commonly known as SAC solder alloy.

With the advent of new materials, the reliability of solder joints became a major concern, especially in harsh environment. In electronics, the reliability is typically limited by the fatigue failure of a single solder joint. Aging makes the situation worse by altering the mechanical and physical properties of the solder material. The precipitate coarsening and the growth of the brittle intermetallic compound layer over time weakens the solder joint and hence deteriorates the reliability. Several elements such as bismuth, nickel, antimony, cobalt and indium have been microalloyed with the SAC based solder alloy to mitigate the adverse effects of aging.

In this study, thermal cycling reliability of aged SAC based solder alloys is examined. Twelve solder pastes from the leading manufacturers with three solder spheres, namely, SAC105, SAC305 and match (where solder paste is same as solder sphere) and three surface finishes (ENIG, ImAg and OSP) are examined. For certain solder pastes, matching spheres could not be used due to their unavailability. The test vehicle consists of three $15\text{mm} \times 15\text{mm}$ CABGA208s,

three $6\text{mm} \times 6\text{mm}$ CABGA36s, three $5\text{mm} \times 5\text{mm}$ MLFQFNs and a bank of six 2512SM resistors connected in series. A printed circuit board was made of four layers of FR-4 glass epoxy substrate with non solder mask defined pads. Several boards were aged at 125°C for a period of twelve months starting immediately after the assembly. The aged boards were subjected to thermal cycling in a temperature range -40°C to $+125^{\circ}\text{C}$ with 15 minutes dwell at $+125^{\circ}\text{C}$ and 10 minutes dwell at -40°C . The profile had a ramp time of 50 minutes, which corresponds to a rate of about 3.3°C per minute. The components were continuously monitored throughout the test. The failure data collected was used for statistical analysis using Weibull and DOE-ANOVA methods. After the test, the failed components were cross-sectioned and analyzed using optical and scanning electron microscopes to have an understanding about different failure modes.

From the study, it could be concluded that SAC based alloys with elements such as Bi, Sb, and Ni had better fatigue resistance and therefore better reliability than SAC305 alloy. ENIG finish with its Ni layer performed better than the other surface finishes. It could also be concluded that the reliability depends on the combination of different factors considered in the study (solder paste, sphere and finish). For example, just because of the fact that ENIG performs better than ImAg and OSP, it does not guarantee that ENIG has better reliability in all combinations of solder paste/sphere/finish as the material properties of the whole solder joint vary with the combination (interaction effect of factors).

Acknowledgments

First, I would like to thank Dr. Sa'd Hamasha for his patient guidance and support without which this work would not have been possible. His knowledge and enthusiasm in research have always inspired me to set high goals in life. His friendly and approachable nature made my academic life much easier and he has always provided opportunities to nurture my skills and abilities. I would like to extend my gratitude to Dr. John Evans for several opportunities and for his help throughout this doctoral program. Also like to extend my sincere gratitude to Dr. Michael Bozack who was always there to help me with his technical expertise. I thank Dr. Gregory Harris for being on my committee. I offer my sincere gratitude to Dr. Vishwani Agrawal for helping me throughout my graduate life at Auburn and for being the university reader.

I would like to extend thanks to my friends and lab mates: Dr. Thomas Sanders, Dr. Cong Zhao, Dr. Sharath Sridhar, Dr. Seth Gordon, Dr. Sinan Su, Dr. Anto Jeson Raj, Dr. Raed Alathamneh, Dr. Muhammed Abueed, Dr. Ming Hong, Xin Wei, Muhamed Belhadi and Palash Vyas. It was a pleasure working with you all on different projects.

I would like to thank my parents for their sacrifices and great support throughout my academic life in this foreign country. Last but not the least, I would like to thank the Almighty for his guidance and unwavering support throughout my life.

Table of Contents

Abstract	ii
Acknowledgments	iv
List of Abbreviations	xvii
1 Introduction	1
1.1 Application Challenges	1
1.2 SnPb Based Solder	2
1.3 SnAgCu Based Solder	3
1.4 Reliability	4
1.5 Problem Statement	6
1.6 Research Objectives	8
1.7 Dissertation Organization	9
2 Electronic Packaging and Reliability	10
2.1 Electronic Packaging	10
2.2 Electronic Assembly: Components	11
2.2.1 Through Hole Mount Technology (THMT) Components	12
2.2.2 SMT (Surface Mount Technology) Components	12
2.2.3 Leaded Components	13
2.2.4 No-Lead (Leadless) Components	13
2.2.5 Area Arrays	15

2.2.6	BGA (Ball Grid Array)	16
2.2.7	PGA (Pin Grid Array)	19
2.2.8	LGA (Land Grid Array)	19
2.3	Electronic Assembly: Substrate	20
2.3.1	Substrate Material	20
2.3.2	Solder Mask	21
2.3.3	Surface Finish	22
2.4	Electronic Assembly: Solder Alloy	24
2.4.1	Micro-alloying/Doping	27
2.5	Electronic Assembly: SMT Assembly Process	28
3	Literature Review	34
3.1	Reliability of Pb-Free Solder Joints	34
3.2	Thermal Reliability	34
3.3	Other Reliability Tests	37
3.3.1	Drop Test	38
3.3.2	Vibration Test	39
3.3.3	Low Cycle Fatigue Test	40
3.4	Microstructure Evolution	41
3.5	Effect of Dopants	45
3.5.1	Bismuth (Bi)	46
3.5.2	Antimony (Sb)	47
3.5.3	Nickel (Ni)	48
3.5.4	Cobalt (Co)	50
3.6	Fatigue Models	52
4	Materials and Methods	56

4.1	Test Vehicle Design and Assembly	56
4.1.1	Test Vehicle	56
4.1.2	Test Components	57
4.1.3	Solder Alloys	58
4.1.4	SMT Assembly	59
4.2	Thermal Test	61
4.2.1	Isothermal Aging and Thermal Cycling	61
4.2.2	Data Acquisition System	62
4.2.3	Failure Analysis	63
4.3	Data Analysis	67
4.3.1	Two parameter Weibull plot	67
4.3.2	ANOVA analysis	68
4.3.3	IMC Layer Analysis	69
5	Effect of Surface Finish on Component Reliability	71
5.1	Introduction	71
5.2	Setup and Procedure	72
5.3	Results and Discussion	72
5.4	Conclusion	82
6	Effect of Micro-Alloying New Elements on Thermal Cycling Reliability of Components	84
6.1	Introduction	84
6.2	Setup and Procedure	84
6.3	Results and Discussion	85
6.4	Conclusion	96
7	Effect of Aging on Thermal Cycling Reliability of Micro-Alloyed Solders	97

7.1	Introduction	97
7.2	Setup and Procedure	97
7.3	Results	98
8	Conclusion and Future Work	107
8.1	Conclusion	107
8.2	Future Work	108
	References	109
	Appendices	119
.1	Tables to check for statistical significance	119

List of Figures

1.1	Microstructure evolution [1].	2
1.2	Effects of aging [2].	3
1.3	Weibull analysis for SAC pastes with different Ag content [3].	3
1.4	IMC layer growth [4].	4
1.5	Microstructure evolution for SAC105 during aging at 125°C [5].	4
2.1	Different levels of packaging [6].	11
2.2	THMT components.	12
2.3	Gull wing package [7].	13
2.4	J-lead package [7].	13
2.5	Construction of SMR [8].	14
2.6	Construction of QFN [9].	15
2.7	Area array package [10].	15
2.8	Ball grid array [11].	16
2.9	Cross-section of CBGA component [12].	17
2.10	Cross-section of PBGA component [13].	18
2.11	Cross-section of TBGA component [14].	18
2.12	Comparison of standard BGA with CSP component [15].	19
2.13	PGA package [16].	19
2.14	Comparison of PGA, LGA and BGA packages.	20
2.15	Different types of vias in substrate [10].	20
2.16	Cross sectional view of NSMD and SMD pads [15].	22
2.17	Top view of NSMD and SMD pads [15].	22

2.18	Surface finish applied on copper pads [17].	23
2.19	Tin-Lead binary phase diagram [18].	25
2.20	Market share of lead-free alloys [19].	28
2.21	Typical SMT assembly flow diagram [15].	28
2.22	Solder paste printing process [17].	29
2.23	Squeegee printing solder paste onto a stencil [19].	30
2.24	Outcomes of solder paste printing [19].	30
2.25	Component pick and placement [19].	31
2.26	Typical reflow profile for lead based and lead-free alloys.	31
2.27	Reflow oven [20].	32
2.28	Multiple zones in a reflow oven [21].	32
2.29	Typical SMT assembly production line [22].	33
3.1	Weibull analysis for surface finishes for 2156 I/O BGAs [4].	35
3.2	Package side crack [4].	35
3.3	Weibull analysis for SAC305 PBGA for multiple reflows and temperatures [23].	36
3.4	Weibull analysis for SnPb and SAC solder TBGA assemblies [24].	36
3.5	Weibull analysis for SAC305 BGA for different temperatures [25].	37
3.6	Summary of characteristic life for SAC305 BGA for different aging duration [25].	37
3.7	SAC305 microstructure evolution during 0, 6 and 12 months of aging [25]. . . .	38
3.8	Chip fracture surface after dye test [26].	38
3.9	Effect of solder joint location and Ag content on the crack area [26].	39
3.10	Crack location for different acceleration PSD amplitudes [27].	39
3.11	Weibull analysis for vibration reliability at different temperatures [28].	40
3.12	Characteristic life of individual SAC305 solder joints cycled at 24 MPa vs. strain rate on log-log scale [29].	41
3.13	IMC growth for control sample and tested sample [4].	42

3.14	Microstructure evolution (a,d) as reflowed, (b,e) after thermal cycling and (c,f) after aging [30].	42
3.15	Initial microstructure of SAC solder [31].	43
3.16	Effect of Ag content on ductility [31].	44
3.17	Crack propagation in different alloys subjected to shear fatigue test [31].	45
3.18	Effect of aging on the microstructure of SAC305 [32].	45
3.19	SEM images of Sn-3.5Ag-0.7Cu-xBi solder joints aged at 190°C for 400 hours (a)x=0; (b)x=1.0; (c)x=2.0, (d)x=3.0; (e)x=4.0; (f)x=5.0 [33].	46
3.20	Effect of Bi on activation energy [33].	47
3.21	SEM microstructures of (a)SAC-0.0Bi (b)SAC-1.0Bi (c)SAC-3.0Bi [34].	47
3.22	Effect of %Bi on creep rate [34].	48
3.23	SEM images of top view of IMC layer of Sn-3.5Ag-0.7Cu-xSb solder joints aged at 190°C for 600 hours (a)x=0; (b)x=0.2; (c)x=0.8 [35].	48
3.24	Backscattered SEM micrographs of cross-sectional view of Sn-3.5Ag-0.7Cu-1.0Sb solder joints aged at 190°C for (a) 1 hour, (b) 200 hours, and (c) 600 hours [35].	49
3.25	Different characteristics affected [35].	49
3.26	Comparison of intermetallic morphology (top view), reflow at 250°C for 1 min [36].	50
3.27	SEM images of solder-substrate interface after aging for 0 and 504 hours at 1150°C [37].	51
3.28	Comparison of microstructure as-cast condition [38].	51
4.1	Testboard.	56
4.2	RBS for surface finishes: (a) ENIG, (b) ImAg, and (c) OSP	57
4.3	Schematic of BGA packages.	58
4.4	Assembly line at UAH.	60
4.5	Reflow oven.	60
4.6	Reflow profile.	61
4.7	Thermal cycling profile.	61

4.8	Test boards in thermal cycling chamber.	64
4.9	Schematic design of data acquisition system.	64
4.10	Semi-automated polishing machine.	65
4.11	ZEISS Axio Imager.M2m optical microscope.	65
4.12	Carbon coating system.	66
4.13	Hitachi S-2460N SEM.	66
4.14	Weibull analysis for samples A, B and C.	67
4.15	Comparison of factors 1, 2 and 3.	68
4.16	Percentage failure analysis.	68
4.17	Main effect plot for two factors, each with three levels.	69
4.18	Interaction effect plot for two factors, each with three levels.	70
4.19	IMC layer thickness measurement.	70
5.1	Test vehicle used.	72
5.2	SEM image of SAC-Bi alloy with ENIG surface finish [39].	73
5.3	SEM image of SAC-Bi alloy with ImAg surface finish [39].	74
5.4	SEM image of SAC-Bi alloy with OSP surface finish [39].	74
5.5	Weibull analysis of surface finishes for Innolot alloy.	75
5.6	Summary of characteristic life and B10 life for Innolot alloy.	75
5.7	Weibull analysis of surface finishes for SAC-Bi alloy.	76
5.8	Summary of characteristic life and B10 life for SAC-Bi alloy.	76
5.9	Weibull analysis of surface finishes for SAC305 alloy.	77
5.10	Summary of characteristic life and B10 life for SAC305 alloy.	77
5.11	Summary of characteristic life for all alloys.	77
5.12	Summary of B10 life for all alloys.	78
5.13	IMC layer thickness measurements.	78
5.14	ANOVA analysis for IMC growth.	79

5.15	ANOVA analysis for characteristic life.	80
5.16	SEM image of SAC-Bi solder joint with ENIG finish.	81
5.17	SEM image of SAC-Bi solder joint with ImAg finish.	82
5.18	SEM image of SAC-Bi solder joint with OSP finish.	82
5.19	Comparison of solder joints with different finishes and SAC-Bi alloy.	83
6.1	Test vehicle used.	85
6.2	Typical solder joint.	86
6.3	Recrystallization after thermal cycling.	87
6.4	Comparison of microstructure of different solder alloy.	88
6.5	Weibull analysis for different alloys with ENIG finish.	89
6.6	Summary of characteristic life for different alloys with ENIG finish.	89
6.7	Summary of B10 life for different alloys with ENIG finish.	90
6.8	Weibull analysis for different alloys with ImAg finish.	90
6.9	Summary of characteristic life for different alloys with ImAg finish.	91
6.10	Summary of B10 life for different alloys with ImAg finish.	91
6.11	Weibull analysis for different alloys with OSP finish.	92
6.12	Summary of characteristic life for different alloys with OSP finish.	92
6.13	Summary of B10 life for different alloys with OSP finish.	92
6.14	ANOVA analysis - Main effects plot.	93
6.15	ANOVA analysis - Interaction effects plot.	93
6.16	Cross-section images of different alloys.	94
6.17	Polarized cross-section images of different alloys.	95
7.1	Thermal profile used for test.	98
7.2	Weibull analysis for paste A (SAC305).	99
7.3	Weibull analysis for paste B (Innolot-A).	100
7.4	Weibull analysis for paste C (SAC-6.0Bi).	100

7.5	Weibull analysis for paste D (SAC-5.5Sb-Ni).	101
7.6	Weibull analysis for paste E (SAC-Sb-Bi-In-Ni).	101
7.7	Weibull analysis for paste F (SAC-Bi++).	102
7.8	Weibull analysis for paste G (SAC-Bi).	102
7.9	Weibull analysis for paste H (SAC-Bi-Sb).	103
7.10	Weibull analysis for paste I (SAC-0.5Bi-6.0In).	103
7.11	Weibull analysis for paste J (SAC-Bi).	104
7.12	Weibull analysis for paste K (Innolot-H).	104
7.13	Weibull analysis for paste L (SAC++).	105
7.14	Weibull analysis for paste M (SAC-Bi-Sb-Co).	105
7.15	Weibull analysis for paste N (SAC++).	106

List of Tables

2.1	Types of gull wing and J-lead packages [6, 7].	14
2.2	Engineering properties of FR-4 substrate [15].	21
3.1	Degradation of fatigue life after four years of room temperature aging [40]. . .	41
3.2	Chemical compositions of IMC determined by EPMA [36].	50
4.1	Package specifications.	58
4.2	Solder paste composition.	59
4.3	Component matrix for CABGA208 in aged condition.	62
4.4	Component matrix for SMR2512 in aged condition.	62
4.5	Component matrix for CABGA36 in aged condition.	63
4.6	Component matrix for QFN in aged condition.	63
5.1	Solder alloys in the study.	71
5.2	Test matrix.	72
6.1	Solder alloys used in the study.	85
6.2	Test matrix.	86
6.3	Element content.	93
7.1	Solder alloys in the study.	98
7.2	Test matrix.	98
1	ANOVA analysis table for paste A (SAC305).	119
2	ANOVA analysis table for paste B (Innotot-A).	119
3	ANOVA analysis table for paste C (SAC-6.0Bi).	120
4	ANOVA analysis table for paste D (SAC-5.5Sb-Ni).	120
5	ANOVA analysis table for paste E (SAC-Sb-Bi-In-Ni).	120

6	ANOVA analysis table for paste F (SAC-Bi++).	120
7	ANOVA analysis table for paste G (SAC-Bi).	121
8	ANOVA analysis table for paste H (SAC-Bi-Sb).	121
9	ANOVA analysis table for paste I (SAC-0.5Bi-6.0In).	121
10	ANOVA analysis table for paste J (SAC-Bi).	121
11	ANOVA analysis table for paste K (Innolot-H).	122
12	ANOVA analysis table for paste L (SAC++).	122
13	ANOVA analysis table for paste M (SAC-Bi-Sb-Co).	122
14	ANOVA analysis table for paste N (SAC++).	122

List of Abbreviations

ANOVA Analysis of Variance

BGA Ball Grid Array

CABGA Chip Array BGA

CTE Coefficient of Thermal Expansion

DOE Design of Experiments

ENEPIG Electroless Nickel Electroless Palladium Immersion Gold

ENIG Electroless Nickel Immersion Gold

EPMA Electron Probe Micro-Analysis

HASL Hot Air Solder Leveling

I/O Input/Output

ImAg Immersion Silver

IMC Intermetallic Compound

ImSn Immersion Tin

MLF QFN Micro Lead Frame

NSMD Non-Solder Mask Defined

OSP Organic Solderability Preserve

Pb Lead

PBGA Plastic BGA

PCB Printed Circuit Board

PSD Power Spectral Density

QFN Quad Flat No-lead

QFP Quad Flat Package

RBS Rutherford Backscattering Spectroscopy

RoHS Restriction of Hazardous Substances

SBGA Super BGA

SEM Scanning Electron Microscope

SMD Solder Mask Defined

SMOBC Solder Mask Over Bare Copper

SMR Surface Mount Resistors

SMT Surface Mount Technology

Sn Tin

TAL Time Above Liquidus

TBGA Tape BGA

THMT Through Hole Mount Technology

WEEE Waste of Electrical and Electronic Equipment

Chapter 1

Introduction

Metallurgy has been around for more than 10,000 years and soldering, which is a key metal joining technology would have probably developed 5,000 years ago. Tin (Sn) and lead (Pb) were introduced as solder materials soon after. With the development of electronics, eutectic Sn-Pb solder had been used among the solder materials, especially due to low melting point and high reliability. But, with the evidence pointing towards the adverse health effects, the search for new materials for replacement was on, in the electronics industry and among universities [41]. SnAgCu based alloys were found to be promising candidates to replace lead based solder.

1.1 Application Challenges

Electronic products find applications in all areas, from consumer electronics such as phones to military and aerospace. In areas such as military and aerospace, they are exposed to harsh environments, in terms of temperature, humidity, vibration, etc. From the documentation from some component manufacturers and from some publications such as MIL-STD-883, it could be noted that the components are typically rated for 20g peak sinusoidal vibrations, 500g of shock using a 0.005s (200Hz) half sine shock pulse, and 30,000g of acceleration for small semiconductor devices. In military electronic systems, acceleration levels of 100g or more are quite common [42]. The thermal cycle frequency for semiconductor components range from five cycles per minute in telecommunication equipment to one cycle per day in personal computer systems.

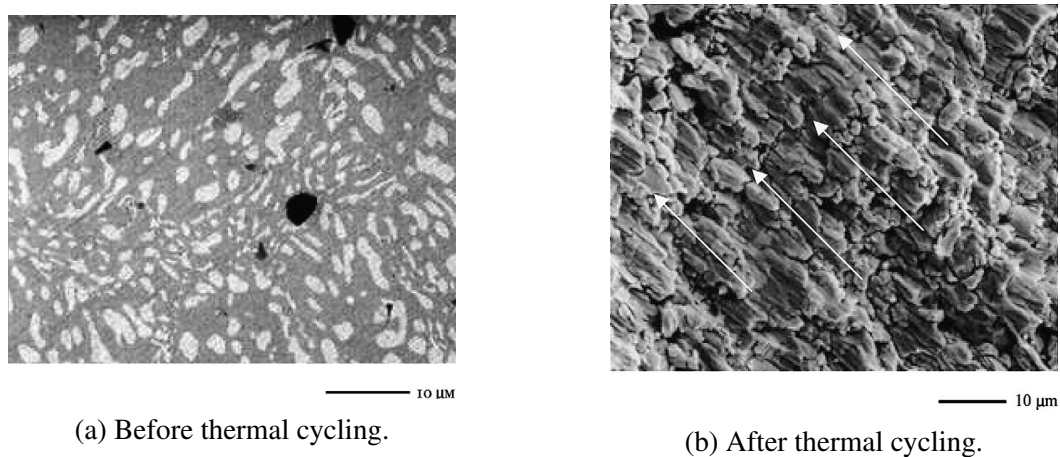
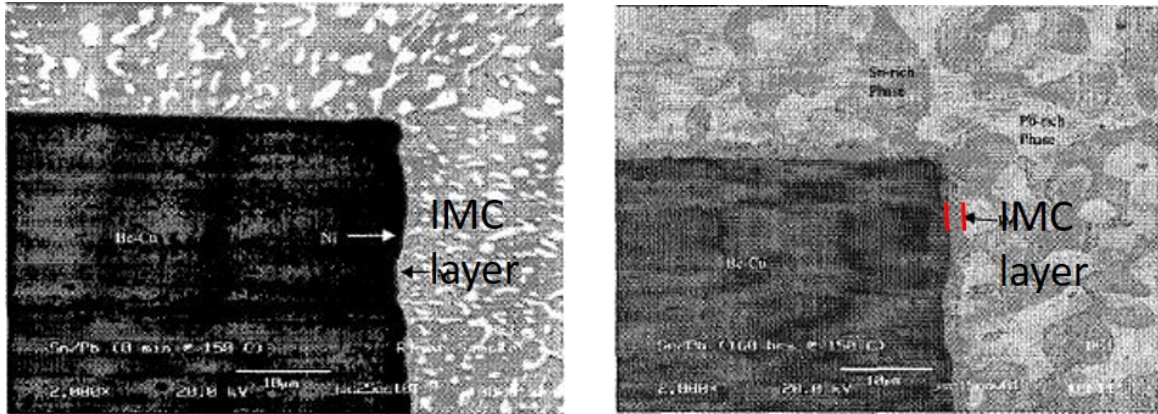


Figure 1.1: Microstructure evolution [1].

1.2 SnPb Based Solder

SnPb based solders were used in electronics extensively till early 2,000s due to their low melting point and favorable mechanical properties. The main requirement of solder joints was to absorb strains arising from the thermal expansion mismatch from different materials [43]. These temperature fluctuations could be from the environment or power cycling. Thermal cycling alters the structural properties of the solder joint. Different failure modes such as fatigue/creep mechanisms and failures due to shear overload were observed in the microstructure after thermal cycling. Figure 1.1a shows the microstructure before thermal cycling and Figure 1.1b shows the structure after the solder joint is exposed to thermal cycling [1].

Soon after the reflow process, copper from the pads dissolves into the bulk solder and form an intermetallic compound at the interface. The IMC layer ensures good metallurgical bonding between the solder and the substrate [2]. This IMC layer keeps on growing since the reflow process, which is detrimental to the strength of the joint due to its brittle nature. To make things worse, aging fuels the growth of IMC layer. Figure 1.2a shows the IMC layer in SnPb solder after reflow in the assembly process. Figure 1.2b shows the IMC layer growth after aging at 150°C for 160 hours [2].



(a) SEM Image of as-reflowed SnPb solder joint. (b) SEM Image of SnPb solder joint after aging.

Figure 1.2: Effects of aging [2].

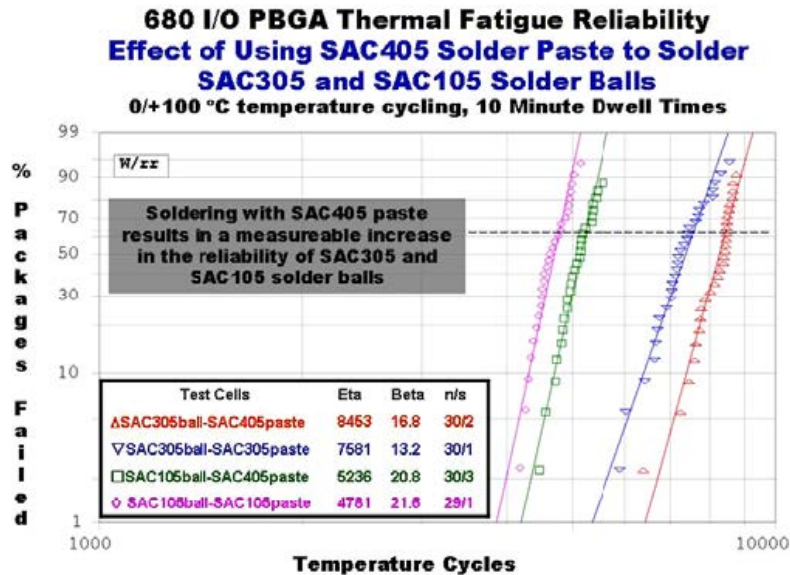


Figure 1.3: Weibull analysis for SAC pastes with different Ag content [3].

1.3 SnAgCu Based Solder

Due to the adverse effects of Pb, new materials were tried in-order to replace the traditional SnPb solder and Tin (Sn)-Silver (Ag)-Copper (Cu) (SAC) based materials showed promising results. It was found that greater the Ag content, better is the reliability in thermal cycling as shown in Figure 1.3 [3]. The increased fatigue life with increased Ag content was attributed to the increased precipitation of Ag_3Sn intermetallic particles at the primary Sn boundaries.

But the continued growth of the brittle IMC precipitates was found to be the cause for lower cycles to failure [4]. Figure 1.4a shows the IMC growth for an ENIG finished SAC305,

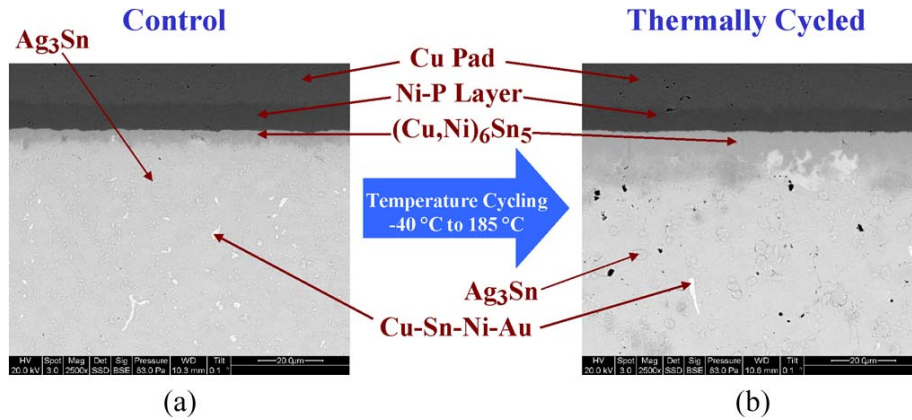


Figure 1.4: IMC layer growth [4].

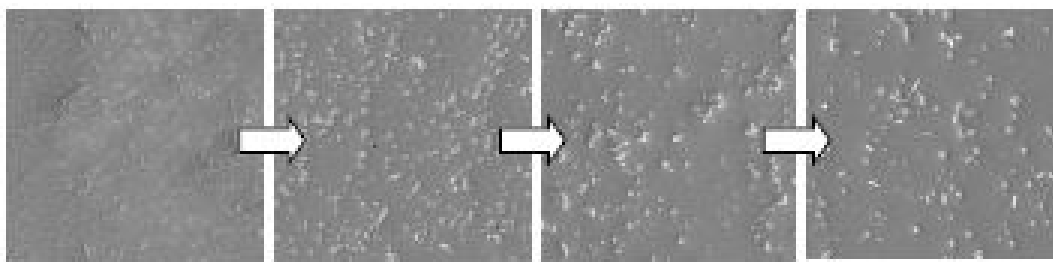


Figure 1.5: Microstructure evolution for SAC105 during aging at 125°C [5].

BGA sample aged at room temperature for two years and Figure 1.4b shows the IMC growth for the sample subjected to thermal cycling for a temperature range of -40°C to +185°C.

Aging also alters the structural properties of the solder material. After the reflow process, the microstructure of SAC alloy consists of Sn matrix (dendrites) and Ag_3Sn and Cu_6Sn_5 second phases (intermetallics) [5]. During the aging process, the Sn dendrites grow larger and merge, while the second phase intermetallics develop into larger and often needle shaped structures. This coarsening is fueled by higher temperatures and longer aging periods. The coarsened second phases are not as effective in blocking the dislocation movement or grain sliding, thus resulting in loss of strength. Figure 1.5 shows the evolution of microstructure for SAC105 during aging at 125°C. It was also found that the creep rate decreased with the increase in Ag content.

1.4 Reliability

Reliability of a product is the probability that the product does not fail during its expected operational life time. Due to the differences in manufacturing processes and operational conditions

reliability, or the failure probability, increases with time. Failure data from the tests (accelerated life testing) is used to generate failure distributions in accordance to time. Based on various demands of service duration and reliability, electronic products are classified into three categories:

Class I: Consumer products - These products have a service life of less than five years and demand for reliability is comparatively low.

Class II: Dedicated/Industrial products - These products have a service life that is longer than class I products and reliability demand is relatively higher.

Class III: Critical products - These products have a service life of more than 20 years and demand of reliability is the highest among the three with a very narrow or no margin for error.

Weibull distribution is one of the most useful probability distributions in reliability [44]. The Weibull failure distribution could be used to model both increasing and decreasing failure rates characterized by hazard rate function of the form:

$$\lambda(t) = at^b \quad (1.1)$$

which is a power function. The function $\lambda(t)$ increases for both $a > 0, b > 0$ and decreases for $a > 0, b < 0$. It could also be expressed in the following form for mathematical convenience:

$$\lambda(t) = \frac{\beta}{\theta} \left(\frac{t}{\theta}\right)^{\beta-1} \quad \theta > 0, \beta > 0, t \geq 0 \quad (1.2)$$

where β is shape parameter and θ is a scale parameter. Once the hazard rate function $\lambda(t)$ is known, reliability function is derived as follows:

$$R(t) = \exp\left[-\int_0^t \lambda(t') dt'\right] \quad (1.3)$$

Substituting $\lambda(t)$ in equation 1.3, we get:

$$R(t) = \exp\left[-\int_0^t \frac{\beta}{\theta} \left(\frac{t'}{\theta}\right)^{\beta-1} dt'\right] = e^{-(t/\theta)^\beta} \quad (1.4)$$

and the probability of failure $F(t)$ is defined as:

$$F(t) = 1 - R(t) = 1 - e^{-(t/\theta)^\beta} \quad (1.5)$$

Two parameter Weibull analysis is used to quantify the reliability of the tested product.

1.5 Problem Statement

In general, an electronic package consists of circuits on a silicon die enclosed in a package that is attached onto a PCB using interconnections and there are several materials such as epoxy, substrate, copper traces, components, silicon, etc., that go into a package. These materials have different coefficients of thermal expansion (CTE), which determine their rates of expansion on exposure to temperature variation. Due to the CTE mismatch between the component and the PCB, upon exposure to temperature variation, a stress is induced on interconnections, which are solder spheres in the case of BGAs. In real world applications, the electronic packages are exposed to several thermal cycles. This results in fatigue of the solder joints and adversely affects the reliability of the electronic product. Therefore, the reliability of solder joint is crucial for the electronic device to function as expected throughout the required period, which in turn is influenced by the solder paste, solder sphere, surface finish and other factors that constitute the joint.

Electronics packaging industry has switched to lead free solders for more than a decade. Finding a replacement for the traditional SnPb solder still remains a challenge in the industry, especially for harsh environments. One type of solder alloy might be a good fit for a particular condition (i.e., thermal cycling), but may not be suitable for another condition (i.e., vibration). SAC based solder alloys have been showing promising results among several materials. Kariya et al. [31] study the effects of Ag content on shear fatigue properties. SAC105 and SAC305 are the popular solder alloys and it was found that with the increase of Ag content, the strength of the alloy increases, which also makes it brittle. In another study by Yongping et al. [26], it was concluded that 1% Ag is better for drop tests than 3% Ag. But in the case of thermal cycling,

fatigue resistance was found to increase with the Ag content according to the studies by Otiaba et al. [45] that makes SAC305 better than SAC105 for thermal cycling.

Since a solder joint consists of not only solder paste, but also solder sphere and surface finish, the influence of these factors on the reliability should be taken into consideration. In a study by Akkara et al. [46], it was found that ENIG finish was better than others, which could be attributed to the Ni coating that acts as a barrier to diffusion of copper. In another study focusing on the effect of mixing solder spheres with SAC-Bi pastes [47], it was found that solder spheres have much more significant influence on the reliability than surface finish and that SAC305 spheres and match (solder sphere is same as solder paste) spheres were better than mixing SAC105 with SAC-Bi based pastes. Industry has been trying different combinations of solder pastes with different solder spheres and surface finishes and until very recently, the effect of aging has not been considered. Research has shown that the aging degrades the fatigue life of solder joints significantly due to precipitate coarsening and the growth of IMC layer. When the particles are fine and small, they effectively block the movements of dislocations and reduce grain sliding that strengthens the material [48]. But, as they get bigger and coarse, their ability to block the dislocation movements and grain boundary sliding is reduced, which in turn reduces the strength and creep resistance of the material. Even aging at room temperature has degrading effects as concluded by Sinan et al. [40]. In that study, it was found that dopants mitigated the effects of aging and that it also led to an increase in inelastic work per cycle and plastic strain range. Aging at higher temperatures fuels detrimental effects. Zhang et al. [48] studied the effects of temperature on the solder joint reliability and it was found that creep rates are higher for elevated aging temperatures and that the alloys with lower silver content are more sensitive to aging than the alloys with higher silver content. Very little research addresses the effects of recrystallization during thermal cycling. In the study by Mattila et al. [49], it was concluded that the new grain boundaries resulting from recrystallization provided favorable sites for crack propagation with less energy consumption compared to crack propagation in as-soldered microstructure.

Most of the current research considers only one or two factors with one or utmost two levels in each factor. So, the research would not encompass all the factors that come into play

in the solder joint reliability. Furthermore, in most researches, the solder pastes used might not be the ones from the market by different manufacturers. So, the real world applications may not be represented by their results. In high reliability applications where ten or more years of product life is expected (e.g., automotive, military, and aerospace), thermal fatigue is the major cause of failure of solder joints. In these applications, failures could be fatal and are never expected. Therefore, insight into thermal cycling reliability of the new materials considering the different aforementioned factors are crucial for high reliability applications. From the results of the research, the packaging industry would be able to better understand the effects of different factors and dopants on the reliability of solder joints, thereby allowing them to determine the best combination for harsh applications.

1.6 Research Objectives

Thermal cycling of BGA components is done after one year of aging. The factors that influence the solder joint reliability, such as solder paste, solder sphere, surface finish and aging are considered to ensure that the test conditions are close to the real world applications. Further, DOE - ANOVA analysis is done to determine the influence of all the factors and their interactions on the reliability of solder joints. The following objectives are to be obtained from the study:

- Develop and conduct tests to study the thermal cycling reliability.
- Analyze the data statistically to find out the different patterns/trends.
- Analyze the failed samples for various failure modes.
- Study the effect of surface finish (ENIG, ImAg, and OSP) on component reliability considering IMC growth.
- Study the effect of Bi in solder alloy composition on component reliability.
- Investigate the influence of different factors on the intermetallic compound (IMC) layer growth and its effect on the solder joint reliability.

1.7 Dissertation Organization

This dissertation consists of eight chapters. Chapter 1 briefs the entire study with relevant background information and concludes with the research objectives. Chapter 2 gives more in-depth knowledge about the concepts used in the study. Chapter 3 throws light on the research related to this study conducted all over the globe. The fourth chapter details the materials and methods used in the study that would allow to reach rational and scientific conclusions. Chapter 5 investigates the effect of three surface finishes, namely, ENIG, ImAg and OSP on the component reliability in thermal cycling and the effects of different alloy compositions are dealt with in Chapter 6. Chapter 7 analyzes the data for a different thermal cycling test and in Chapter 8, the major conclusions drawn from the study are mentioned with potential options for expanding this study.

Chapter 2

Electronic Packaging and Reliability

2.1 Electronic Packaging

The main purpose of the electronic package is to provide both mechanical and electrical bond for the component in the package. So, they are found in all electronics. And the reliability of this package ensures that the electronic product is reliable throughout its lifetime. With the advancement in technology, the electronic products are shrinking in size day by day, with reduced dimensions, low power consumption, and at the same time becoming faster and efficient. These product requirements impose significant challenges on the packaging industry. All the electronics start as silicon die with circuit patterns etched onto them.

Silicon crystal ingots are produced by the Czochralski (CZ) method. The ingots are sliced into thin wafers with a diamond saw and are polished for a smooth and flat surface for high yield optical photolithography [50]. The circuits mostly consist of different types of transistors, which are fabricated through the repeated application of a number of basic processing steps, namely, oxidation, photolithography, etching, diffusion, evaporation or sputtering, chemical vapor deposition, ion implantation, epitaxy and annealing [6]. The completed wafer is tested, diced and packaged in a variety of packages based on applications. The functions of the packages are signal distribution, power distribution, heat dissipation and protection (mechanical, chemical and electromagnetic).

There are different levels of packaging as shown in Figure 2.1. First level package is the chip carrier, which is the housing for the thin and fragile silicon chip. The silicon die is mechanically attached to the lead frame and electrically connected to its carrier through wirebonds or flip chip BGA. The chip carrier protects the silicon die from detrimental effects of the environment and from the damage due to abusive handling in the assembly. It also

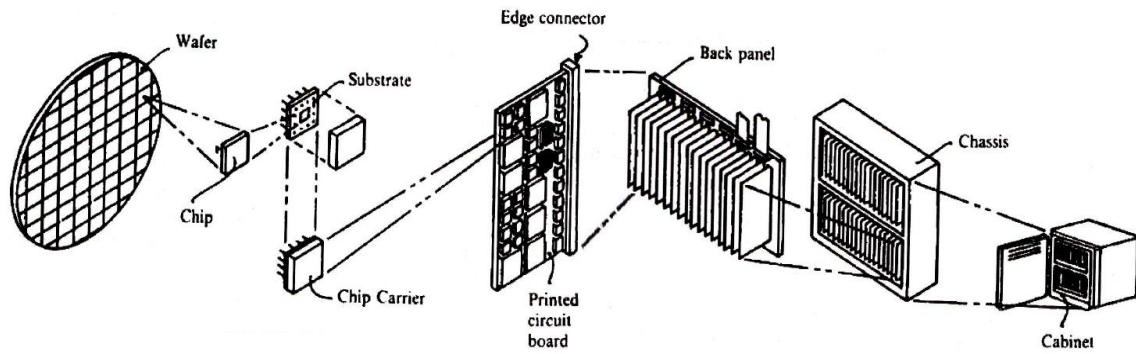


Figure 2.1: Different levels of packaging [6].

isolates the chip from shock or vibration during the service. The chip carrier also facilitates the interconnections from circuits on the chip to other chips on the circuit board.

The second level package connects components using printed circuit assembly, which is mounted on a PCB. PCB is generally a rigid laminate constructed of layers of fiber glass-epoxy composite. This layer contains both external and internal layers of copper for connecting components. The chip carrier could be attached to the PCB using through-hole mount technology (THMT) and surface mount technology (SMT) [51]. In the through hole mounting, the components with leads are inserted into the holes in PCBs and soldered onto pads on the other side [52], whereas in the surface mounting the components are mounted or placed directly onto the PCB surface. SMT is more popular in the industry as it has many advantages such as better mechanical performance, higher component density, higher real estate utilization, and lower cost. Third level packaging consists of all the hardware required to house the circuit boards and peripheral equipment for a complete electronic system [41]. These enclosures support the circuit boards, protect the components from the environment, provide a cooling medium and cabling facilities required for higher level connections.

2.2 Electronic Assembly: Components

There are different methods involved in the second level packaging. Based on the component to PCB mounting method, they could be classified into through-hole mount technology and surface mount technology.

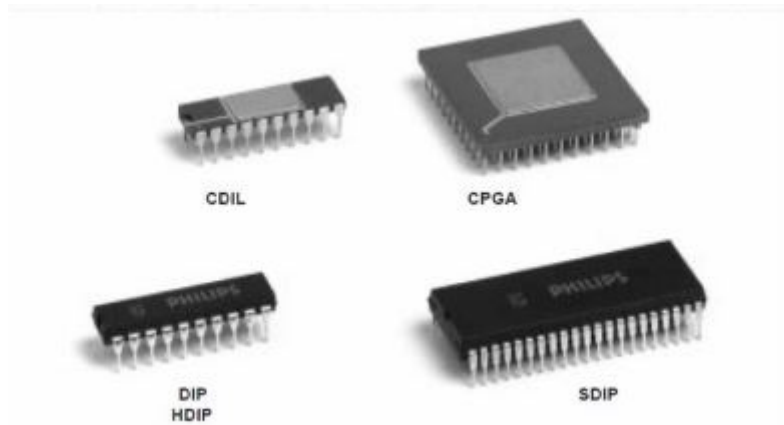


Figure 2.2: THMT components.

2.2.1 Through Hole Mount Technology (THMT) Components

As the name suggests, the basic idea in THMT is to insert the leaded components into the PCB through drilled holes or vias and wave solder the leads on to the pads on the other side of the PCB. This technology was developed in the 1950s and remained popular till the 1980s, when the SMT took over. Some examples for THMT packages are single in-line package (SIP), dual in-line package (DIP), ceramic DIP (CDIP), quadruple in-line package (QIP), skinny DIP (SDIP), etc. Figure 2.2 shows examples of THMT components. THMT components are highly reliable due to the ability of their lead frame structure to take up thermally induced stresses. On the contrary, this technology requires holes to be drilled through the PCB, which makes the process expensive. Another major disadvantage is that the THMT components require more PCB real estate and provide fewer input/output (I/O) connections. These made the technology less popular in the packaging industry and paved the way for SMT technology that is currently popular.

2.2.2 SMT (Surface Mount Technology) Components

SMT, as the name suggests, involves placing components directly on the PCB surface and using the reflow method to form the solder joint [6]. Unlike THMT, the components could be placed on both sides of the PCB, which doubles the available real estate of the board. And since there are no holes or leads, SMT has a much higher component density with lower cost and faster board assembly. SMT components are also smaller than THMT components as they

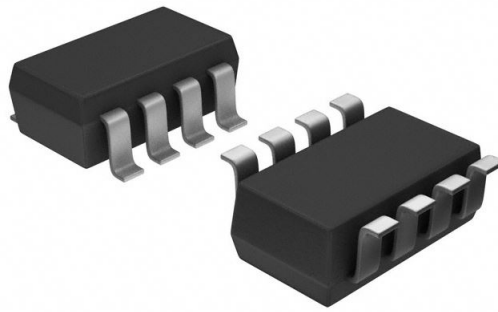


Figure 2.3: Gull wing package [7].

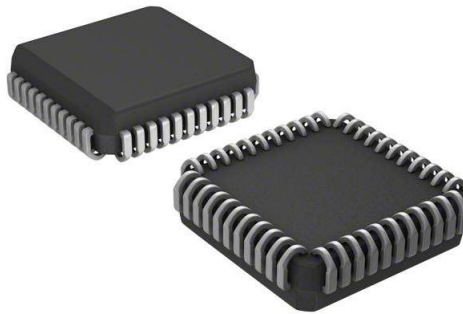


Figure 2.4: J-lead package [7].

have finer lead pitches and the I/O could be placed on all four sides, including the bottom of the component. But their smaller size leads to complicated thermal management and with less solder for each joint, the solder joint reliability is of a great concern. SMT supports both leaded and non-leaded components.

2.2.3 Leaded Components

The two main types of leaded components are gull wing and J-lead. As the names suggest, the gull wing component has its leads in the shape of a gull wing whereas a J-lead component has its leads folded under its body in the shape of 'J'. Figure 2.3 and Figure 2.4 show gull wing package and J-lead package, respectively [53]. There is large variety of surface mount components among which the gull wing and J-lead components are popular. Table 2.1 lists primary categories of gull wing and J-lead packages.

2.2.4 No-Lead (Leadless) Components

Component leads take up the thermal stress at the component-PCB interface. Leadless components have bare metal terminations on the bottom that are placed directly onto the solder paste





Gull Wing Packages		J-Lead Packages	
Small Outline IC (SOIC)		Small Outline J-Lead	
Quad Flat Pack (QFP)		Plastic Leaded Chip Carrier	
Small Outline Transistor (SOT)			

Table 2.1: Types of gull wing and J-lead packages [6, 7].

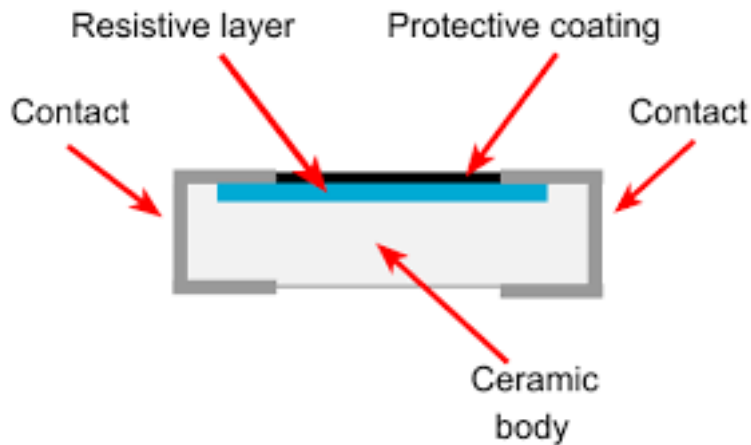


Figure 2.5: Construction of SMR [8].

printed copper pads on the PCB. Leadless components mainly consist of SMRs and QFNs. Figure 2.5 and Figure 2.6 show the construction of SMR and QFN components, respectively.

Most of the surface mount components consist of a silicon die that is connected to the copper lead frame using wirebonds. Gold is popularly used as wirebond followed by aluminum and copper in certain cases. Wire bonding is done using thermo-compression in the case of gold and ultrasonic bonding technique in the case of aluminum wires [6, 51]. The silicon die with wirebonds and lead frame are encapsulated with plastic. Flat no-lead components include an exposed thermal pad at the center of the component on the bottom to improve heat transfer [54].

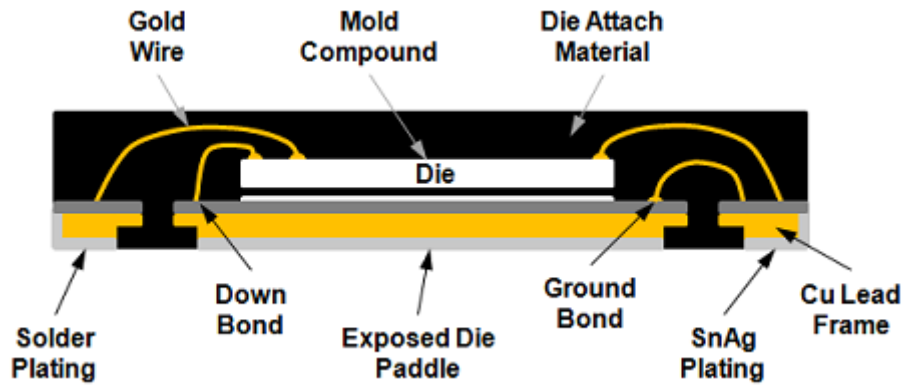


Figure 2.6: Construction of QFN [9].

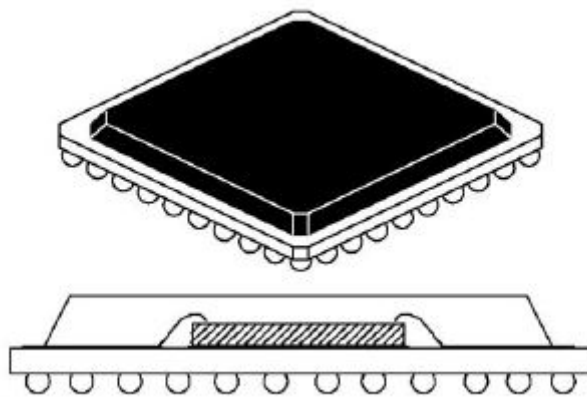


Figure 2.7: Area array package [10].

2.2.5 Area Arrays

As the number of I/O requirements increased, the packaging industry preferred progressively finer pitches. But these came with concerns such as increased fragility of finer pitch leads and bridging. In order to accommodate more I/O requirements with better reliability, the packages had the I/O on the bottom as area array or two dimensional lattice (Figure 2.7). For a square component with n leads on one side, the maximum I/O channels that it could accommodate is $4n$, whereas in the case of an area array component it could accommodate n^2 I/O channels. Area array could dramatically increase the I/O capabilities without decreasing the lead pitch. A popular area array component is the ball grid array (BGA) that has solder spheres on the contact pads at the bottom of the component. During the reflow process, the spheres reflow and wet together with the solder paste to form a solder joint. There are packages in which there is a higher standoff. These types of components are called column grid array (CGA). Similarly,

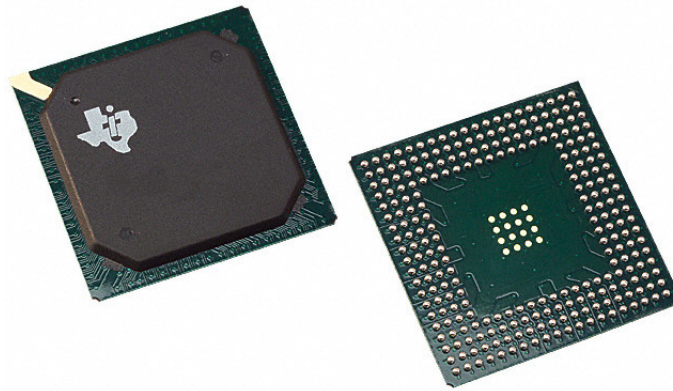


Figure 2.8: Ball grid array [11].

the components on which thick metal pins are attached in the place of solder balls are called pin grid array (PGA). There is a variety of BGA packages available, including Plastic BGA (PBGA), Super BGA (SBGA), Ceramic BGA (CBGA), ChipArray Thin Core BGA (CTBGA), Very Thin ChipArray BGA (CVBGA) and Flip Chip BGA (FCBGA).

2.2.6 BGA (Ball Grid Array)

BGAs have been the most popular packages among the area array components used with surface mount technology. As mentioned in the previous section, the BGA package has solder balls attached to the contact pads below the package. These packages are placed with solder spheres on the corresponding pads with solder paste on the PCB. The boards are then reflowed and electrical bonds are formed through the solder joints. Figure 2.8 shows a BGA component with solder spheres on the bottom side of the component.

The major disadvantage of BGA is that it is not mechanically compliant as the solder balls are not capable of taking thermal stress like the flexible leads. All materials expand or contract at different rates when exposed to a temperature change. For each material, this rate is determined by the coefficient of thermal expansion (CTE). Different materials that constitute

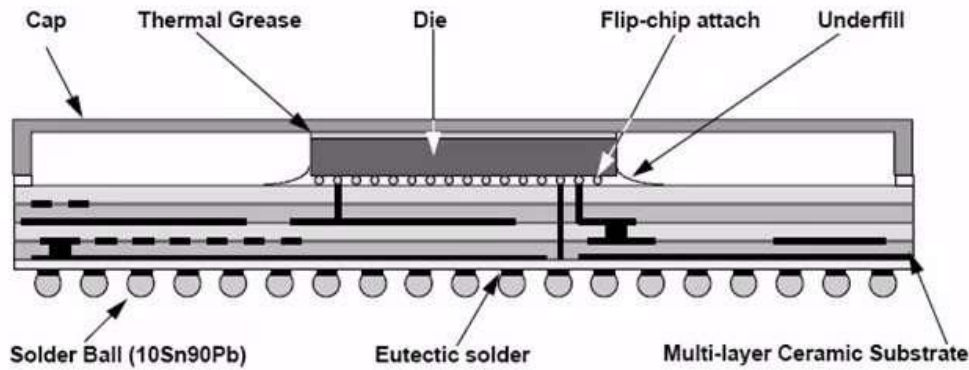


Figure 2.9: Cross-section of CBGA component [12].

the electronic assembly have a corresponding CTE. So, when the assembly is subjected to a thermally harsh environment, stress is developed at solder joints that form the interface between BGA component and PCB. Such exposures to thermal cycles cause fatigue in the joints which gradually leads to the failure. This situation is mitigated using underfills that help by matching the CTE of BGA with that of PCB. By the process of underfilling, an epoxy mixture is injected under the BGA component after it is soldered onto the PCB. There are several types of BGA components [55]:

1. CBGA- Ceramic BGA: A square or rectangular shaped ceramic package with solder balls arranged in a grid or array at the bottom of the package. The solder ball arrangement could be either perimeter, full grid array or staggered. Figure 2.9 shows the cross-section of a CBGA component with a flip chip attached. Multiple layers of substrate for interconnection could also be seen.

2. FCBGA - Flip-chip BGA: In FCBGAs, the die is positioned face down with direct connections to the substrate using solder spheres. FCBGA could have multiple layers of plastic or ceramic substrate as shown in Figure 2.9. Some advantages of the flip chip are reduced electrical inductance and component footprint as the die shrink.

3. PBGA - Plastic Ball Grid Array: PBGAs could have either two or four layer substrates, with organic materials. PBGAs come in different pitch sizes and component body size. The silicon die is attached to the solder spheres through wire bonds and vias as shown in Figure 2.10.

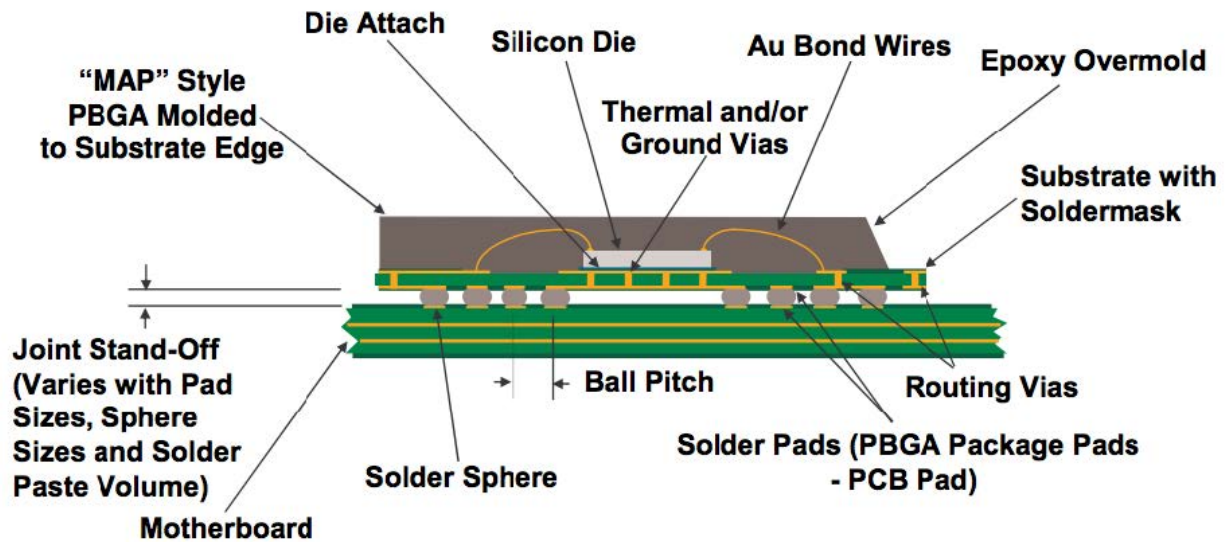


Figure 2.10: Cross-section of PBGA component [13].

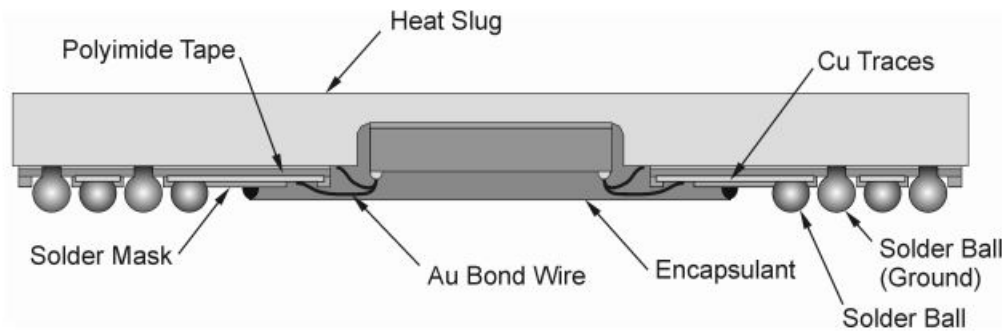


Figure 2.11: Cross-section of TBGA component [14].

4. TBGA - Tape Ball Grid Array: TBGA consists of a substrate composed by one or two soft polyimide tapes as shown in Figure 2.11. The silicon die is faced down with wire bonds providing connections to the package. Silicon die with the wire bonds are secured with the encapsulant.

5. CSP - Chip-Scale Package: In a BGA component, the size of the total package is about 1.2 times that of the die. The comparison of a standard BGA with a CSP component is shown in Figure 2.12. In the case of CSP, the die is mounted on the interposer on which the pads or solder balls are formed or the pads could be etched on the silicon die which results in a package very close to the size of the silicon die.

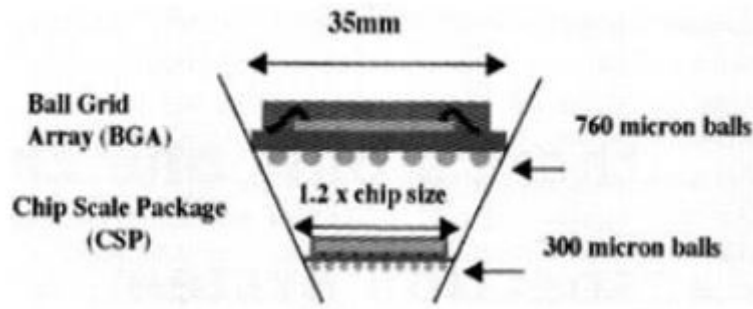


Figure 2.12: Comparison of standard BGA with CSP component [15].



Figure 2.13: PGA package [16].

2.2.7 PGA (Pin Grid Array)

PGA is an area array package similar to BGA, except that the solder spheres are replaced by an array of metallic pins. They are either inserted into the PCB using through hole technique or inserted using a socket. Like any other area array, PGA has more I/O when compared to standard dual in-line package (DIP). PGA was a standard package for most second through fifth generation processors. Figure 2.13 shows an example of PGA.

2.2.8 LGA (Land Grid Array)

LGA is another area array package similar to BGA or PGA except that the solder spheres/metallic pins are replaced by a grid of flat contacts. The contacts are made either by fitting the package into the LGA socket or by soldering them down onto the PCB surface. Figure 2.14 shows the comparison between PGA, LGA and BGA packages.

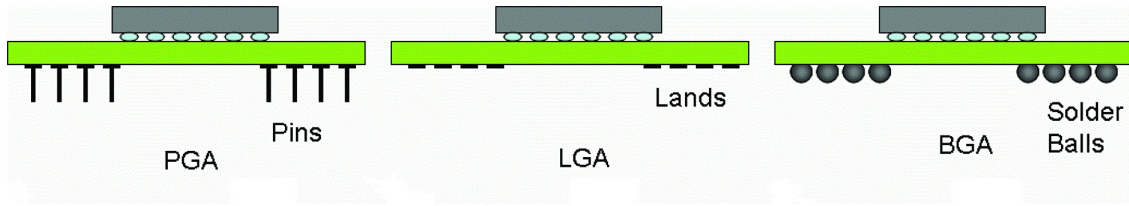


Figure 2.14: Comparison of PGA, LGA and BGA packages.

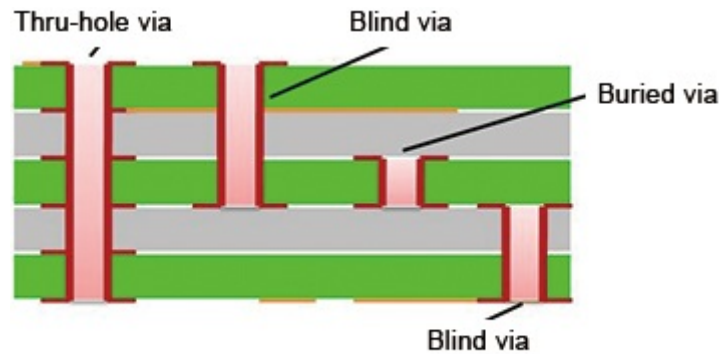


Figure 2.15: Different types of vias in substrate [10].

2.3 Electronic Assembly: Substrate

The electronic packages are mounted on the surface of a rigid substrate material called PCB with metal traces on its surface as well as incorporated internally into the substrate. The components are mechanically attached to the rigid board for physical support and electrically connected to the metal traces for connection between components. The PCB also helps with thermal conduction, dissipation, and electrical isolation [56]. A PCB could be single sided or double sided with multiple layers of laminated substrate. Electrical connections through different layers are made possible using vias. Vias could be buried to connect internal layers or could be blind vias that are exposed only on one side or even be a hole through the multiple layers [57]. Figure 2.15 shows different types of vias incorporated in the substrate.

2.3.1 Substrate Material

FR-4 is a widely used substrate. It is composed of woven fiberglass cloth with an epoxy resin binder that is flame resistant. “FR” stands for flame retardant, and “4” indicates woven glass reinforced epoxy resin [58]. FR-4 substrate is a good electrical insulator with considerable

Key Characteristics	Test Method	Units - English (SI)	Typical Values
Tensile Strength (0.125") LW	ASTM D638	ksi (MPa)	62 (430)
Compressive Strength, Flatwise (0.500")	ASTM D695	ksi (MPa)	66 (455)
Flexural Modulus (0.062") LW CW	--	ksi (GPa)	2,900 (20) 2,600 (18)
Shear Strength (punch type, 0.062")	ASTM D732	psi (MPa)	21,500 (148)
Coefficient of Thermal Expansion	--	" / °C x 10 ⁻⁶	15
Temperature Index	--	°C	130
Glow Wire Flame Index & Ignition Temperature	IEC 60695-2-12	°C	960
Hot Wire Ignition	UL 746A	Sec	120
High Current Arc Ignition (3mm)	UL 746A	Arcs	120
Arc Resistance (0.125")	ASTM D495	Sec	140
Comparative Tracking Index (.125")	ASTM D3638*	V	230
Dielectric Strength Condition A	ASTM D149	V/mil	635
Volume Resistivity (0.062")	ASTM D257	Ω – cm	3(10) ¹⁵
High Voltage Arc Resistance	UL 746A	Sec	300
High Voltage Arc Tracking Rate	UL 746A	mm/min	0

Table 2.2: Engineering properties of FR-4 substrate [15].

mechanical strength, in both dry and humid environments. Properties of FR-4 substrate material are given in Table 2.2.

The thickness of copper layer in FR-4 is typically denoted using “weights” such as “half-ounce” or “one-ounce”. This represents the weight of copper over a 1ft² area on the substrate. Therefore, “one-ounce” of copper layer on FR-4 substrate would be about 34 microns or 1.34 mils thick [59]. From Table 2.2, it could be found that the CTE of FR-4 laminate is about 15 ppm/°C. The overall CTE of the PCB could be affected by its constituents such as number of metal layers, laminate materials, trace density, operating environment and other considerations. The glass transition temperature (T_g) of FR-4 substrate ranges from 120°C to 180°C, during which the resin changes from a glassy to a plastic state. The recommended operating temperature for FR-4 is typically below 130°C [60, 61]. Besides FR-4, other materials such as the standard epoxy glass substrate and bismaleimide triazine (BT) are also used for PCB substrate.

2.3.2 Solder Mask

Solder mask is a thin lacquer-like layer of polymer applied on the PCB. The primary purposes of solder mask are to protect the copper traces on the surface from oxidation and to prevent

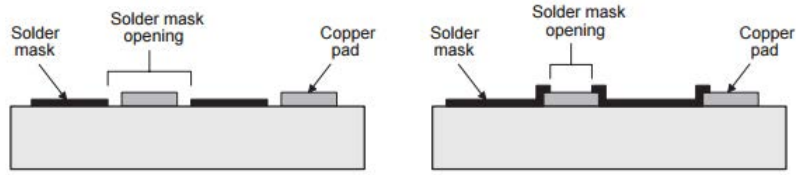


Figure 2.16: Cross sectional view of NSMD and SMD pads [15].

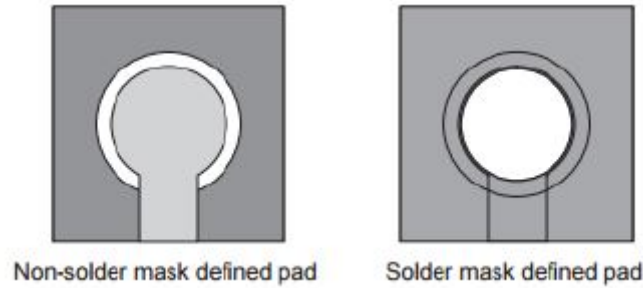


Figure 2.17: Top view of NSMD and SMD pads [15].

solder bridging among densely located copper pads. Acrylic and epoxy polymers are commonly used as solder masks. Copper pads on a PCB could be solder mask defined (SMD) or non-solder mask defined (NSMD). In the case of an SMD pad, the area on which the solder ball could be attached is defined by the solder mask, whereas in the case of NSMD the solder mask does not come on to the copper pads. Assuming that all other factors remain the same, solder joints on NSMD pads are stronger than SMD pads as the area of contact is larger for the NSMD pad. Figure 2.16 and Figure 2.17 show the difference between these PCB designs.

For a PCB with NSMD pads, there would be a gap between the solder mask and the circular copper pad. In this case, the solder flows over the top surface and around the copper pad. This additional soldering area results in a stronger mechanical bond. Clearly, a PCB with NSMD pads has higher resistance against thermo-mechanical fatigue failure as the design spreads the stress over a larger area when compared to SMD pads. As a result NSMD is more widely used as a standard for the PCB design by the industry.

2.3.3 Surface Finish

Solder masks are used to protect the copper traces. But the copper pads are still unprotected. The surface finish is used to protect the copper pads. The surface finish is also known as surface plating or coating. The surface finish not only protects the copper pads from oxidation, it also

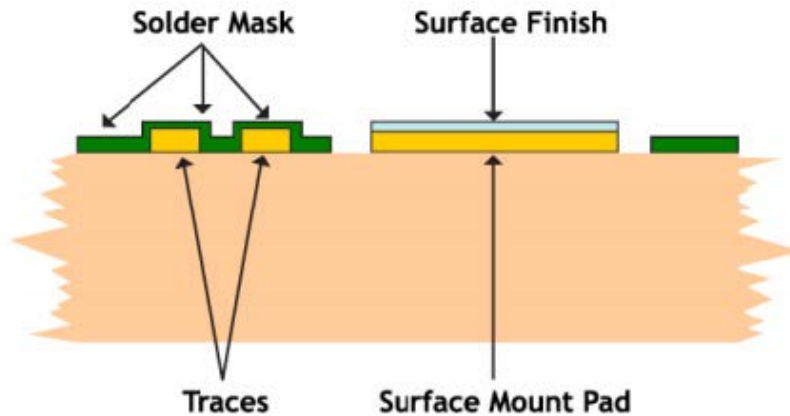


Figure 2.18: Surface finish applied on copper pads [17].

improves solderability by dissolving the outermost layer of surface finish during soldering. Sometimes surface finishes are considered as solder mask over bare copper (SMOBC). Figure 2.18 shows a schematic of cross-section view of PCB with surface finish on top of copper pad.

There are several different types of surface finishes [62]:

1. Hot Air Solder Leveling (HASL): This has been the predominant surface finish used with SnPb solder for a long time. For applying this surface finish, the PCB is immersed into molten Sn-Pb or lead free solder bath. In this process, the solder would cover the metal surfaces on the PCB without solder mask. After the board is pulled out, hot 'air knives' are used to remove the excess solder, which leaves a layer of coating on the copper pads. HASL has good solderability and is one of the least expensive options. But in the process of applying surface finish, the PCB is subjected to severe thermal shock and the coplanarity of the HASL coat on the board surface is very poor. Therefore, the popularity of HASL has dropped significantly in recent years.

2. Organic Solderability Preservative (OSP): This is a water based, organic finish that has a thin protective layer of carbon-based organic compound over the copper pad to protect it from oxidation and contamination. Advantages of OSP finish include low cost, superior coplanarity and solderability. Disadvantages of OSP finish include handling sensitivity, poor shelf life (less than 6 months), easy degradation with temperature and difficulty in testing the circuit as the coating is non-conductive.

3. Immersion Tin (ImSn): ImSn has a flat surface finish. ImSn forms a tin/copper (SnCu) intermetallic compound during the surface deposition process that grows with aging, resulting in significant deterioration of its shelf life. When exposed to elevated temperature during wave soldering, the finish is consumed to form a SnCu intermetallic compound, leading to very poor solderability. Another concern with ImSn is that it uses thiourea, which is a carcinogen.

4. Immersion Silver (ImAg): is a recent addition to the list of surface finish options and continues to grow in popularity. ImAg is a preferred surface finish for those concerned with excellent solderability, long shelf life, and easy probe testing. It performs favorable reliability in thermal and mechanical testing. It can generate a “creep corrosion” problem when using ImAg in an environment involving high sulfur and humidity.

5. Electroless Nickel Immersion Gold (ENIG): is a two-layer metallic coating over catalyzed copper, with nickel (Ni) layer acting as a diffusion barrier to the copper pad and surface to which the soldering occurs, covered by a gold (Au) layer which protects the nickel from oxidation during storage. ENIG provides excellent shelf life, good wettability, great coplanarity for fine pitch components, easy in-circuit testing, and certainly improved product reliability. The only concern when using ENIG surface finish is the higher cost per unit.

6. Electroless Nickel Electroless Palladium Immersion Gold (ENEPIG): is obtained by depositing additional electroless palladium layer to ENIG over the nickel layer and below gold layer. This palladium layer can prevent possible contamination of the nickel migrating into the gold, which can eliminate the “black pads” phenomenon of the ENIG surface finish and thus increase reliability. However, ENEPIG is more expensive than the already costly ENIG surface finish, especially a concern for those on a tight budget.

In summary, choosing right PCB surface finish is essential for predicting cost, quality, and reliability of any printed circuit assembly. Each surface finish has its strength as well as weakness to consider when matching it with particular user needs.

2.4 Electronic Assembly: Solder Alloy

Tin-Lead solders were used in electronic assemblies historically due to their favorable properties such as low surface tension, low melting point, strong intermetallic bonds with copper pads,

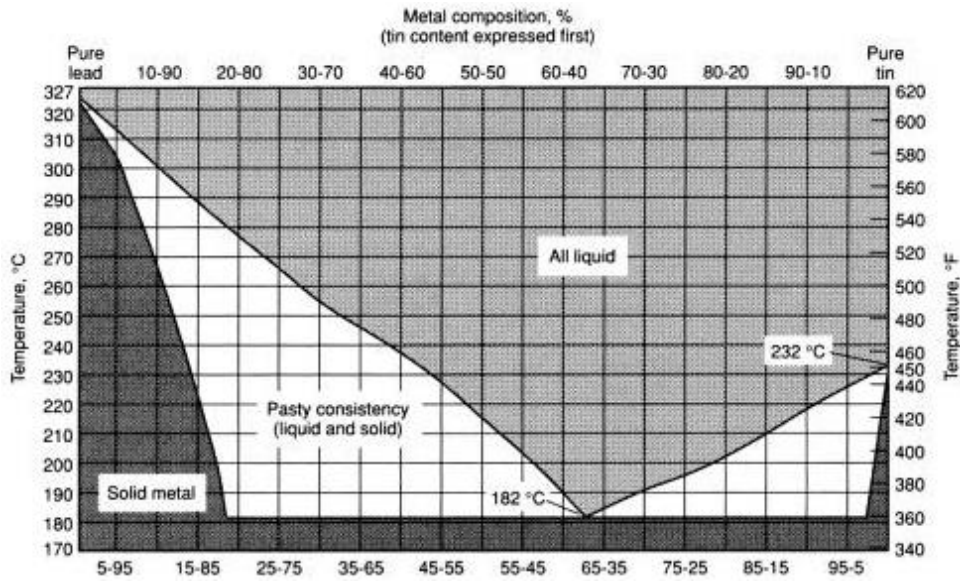


Figure 2.19: Tin-Lead binary phase diagram [18].

ductility and other mechanical properties. One other important feature was that 63Sn37Pb, which was popular in electronics was an eutectic alloy. Eutectic alloys, unlike other materials, have a single temperature at which the entire alloy melts (on increasing temperature) and solidifies (on decreasing temperature) without a ‘pasty’ range. Tin-Lead binary phase diagram is shown in Figure 2.19. Eutectic alloys offer the lowest melting point for a certain alloy system and the 63Sn37Pb has a melting point of 183°C.

Despite all advantages, lead is harmful for humans, especially for children. Lead toxicity, from prolonged exposure could cause learning disabilities, mental retardation, anemia and various other diseases. Once the harmful effects of lead were discovered, Japan and European Union led the drive to eradicate lead from electronics and to commercialize lead free alloys. In 2,000, the European Union put forward two directives towards lead free electronics. The Waste of Electrical and Electronic Equipment (WEEE) directive stipulated that lead should be removed from all the electrical and electronic components at the end of life. The Restriction of Hazardous Substances (RoHS) directive prohibits the use of lead in electrical and electronic components manufactured after July 1, 2006 [63]. As a result of these and similar directives, the industry went in intense search for a replacement. This led to a series of near eutectic alloys based on tin (Sn)-silver (Ag)-copper (Cu), commonly known as SAC solder alloys.

Properties of lead free solders include [6]:

- Low melting temperature similar to 63Sn37Pb
- Good wettability closed to 63Sn37Pb
- Low cost
- Compatibility with soldering process
- Adequate availability on Earth
- Eco-friendly
- Material properties similar to or better than 63Sn37Pb (CTE, ductility, thermal and electrical conductivity, etc.)

SAC alloys typically consist of 3-4% Silver and 0.5-1% Copper (Cu). Addition of small amounts of copper helps in lowering the melting point and in improving the wetting properties. Copper, being cheaper than silver also reduces the cost [64]. Some examples for lead free solders are:

- Tin-Copper Eutectic (Sn99.3 Cu0.7) - Eutectic mixture of tin and copper. Poor mechanical properties, prone to tin whiskers, poor quality when air reflowed. Melting temperature of 221°C.
- Tin-Silver Eutectic (Sn96.5 Ag3.5) - Eutectic mixture of tin and silver. Melting temperature of 221°C. Addition of copper helps in reducing melting temperature and cost by reducing silver content.
- SAC305 (Sn96.5Ag3.0Cu0.5) - Most popular solder alloy in the U.S. electronic industry. Good mechanical characteristics. Pasty range around 217°C to 225°C.
- SAC105 (Sn98.5Ag1.0Cu0.5) - Popular in certain sectors of electronics industry, mainly in cell-phone manufacturing. Has superior drop/shock resistance. Low cost due to reduced silver content.
- SAC387 (Sn95.5Ag3.8Cu0.7) - Not popular in U.S. Recommendation of European IDEALS Consortium.
- SAC396 (Sn95.5Ag3.9Cu0.6) - Used occasionally in U.S. Recommendation by U.S. NEMI group.

2.4.1 Micro-alloying/Doping

In-order to improve the properties of SAC based lead-free solder alloys, several elements were added by the process of micro-alloying or doping. As practised in semiconductor industry, doping means adding dopants to the traditional solder alloys to form a new alloy. But unlike the semiconductor industry where the proportion of dopant is limited to less than 1%, in solders, the proportion could be much larger. Some elements that are used as dopants are Bi, Sb, In, Mg, Ti, Zn, Ce, Co, Ni, La [65]. Micro-alloying with elements is found to enhance the shock/drop resistance, wetting and other mechanical properties. For instance, addition of bismuth (Bi) has several benefits including improved shear strength and reduced IMC layer thickness in lead-free solder alloys.

There are also applications where copper or silver in SAC based alloys are replaced by other elements. Some examples of such cases are listed below.

- Sn42Bi58 - Tin-Bismuth Eutectic solder with low melting point of 138°C, which could reduce the thermal damage. Mechanical strength is also enhanced by bismuth content. But bismuth is not easily available.
- 48Sn52In - Tin-Indium Eutectic solder with melting point of 118°C. The presence of indium decreases the mechanical strength of the alloy but indium is not readily available.
- 20Sn80Au - Tin-Gold Eutectic solder with a high melting point of 280°C. Even with high melting point, this alloy is considered as solder as it is lower than 350°C, which is the transition temperature into the braze materials. The alloy hardness is high and that makes it more rigid than other solders, but also presents some unique manufacturing difficulties. And the presence of gold makes it expensive.
- 95Sn5Sb - Tin-Antimony non-eutectic solder with a pasty range of 232-240°C. Due to its high melting point, it could be used in high temperature applications. Sb enhances the strength and hardness and this alloy has a good thermal fatigue performance. But, the alloy comes with poor wetting properties and the toxicity of antimony is also a concern.
- 91Sn9Zn - Tin-Zinc Eutectic solder with melting point of 199°C. Strength and melting temperature increases with the increase in zinc content. But, as zinc is prone to corrosion, this

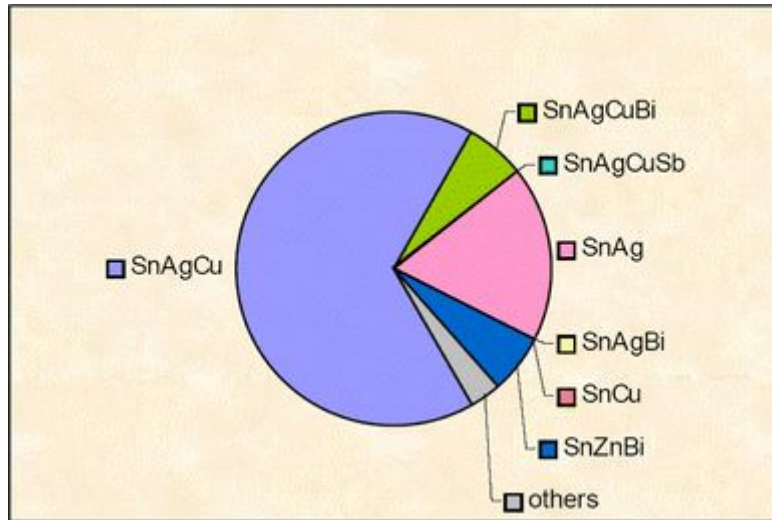


Figure 2.20: Market share of lead-free alloys [19].

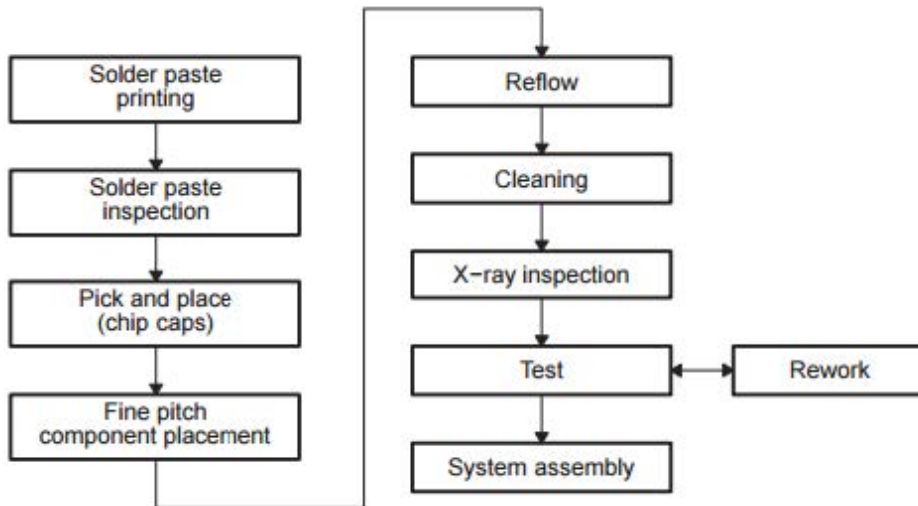


Figure 2.21: Typical SMT assembly flow diagram [15].

alloy has corrosion issues and poor wettability.

Figure 2.20 show the market share for different lead-free alloys.

2.5 Electronic Assembly: SMT Assembly Process

The electronic components are mounted on the copper pads of the PCB substrate by SMT assembly process. Figure 2.21 shows the process flow for a typical SMT assembly.



Figure 2.22: Solder paste printing process [17].

The major steps in a SMT assembly are listed below:

- Step 1: Solder paste printing - The solder paste printing applies solder paste onto the appropriate pads of the PCB to hold the SMT components in place before reflow soldering. This is the most popular method in the industry. The solder paste consists of powder of metallic particles suspended in thick medium named flux. Flux plays the role of an adhesive to hold the components till the reflow process, where the paste melts and forms a physical bond. Figure 2.22 shows the solder paste printing process. The paste is applied onto the copper pads using a stainless steel stencil, with holes for the corresponding pads on the PCB. Use of stencil ensures the accurate deposition of right amount of the paste on the copper pads so that the solder joint between PCB and component terminal is acceptable in terms of mechanical strength and electrical performance. A squeegee blade is used to force the paste through the holes in the stencil onto the PCB. These blades are generally made from metal, but they could also be made from polyurethane. Figure 2.23 shows the printing process using a squeegee. There are different factors that determine the efficiency of a print process such as squeegee pressure, squeegee speed, print stroke, stencil separation speed, stencil cleaning, condition of stencil and squeegee, storage, handling and inspection. The solder paste should be inspected after printing to ensure that there are no defects. The inspection systems in the solder printers use 2D technology while

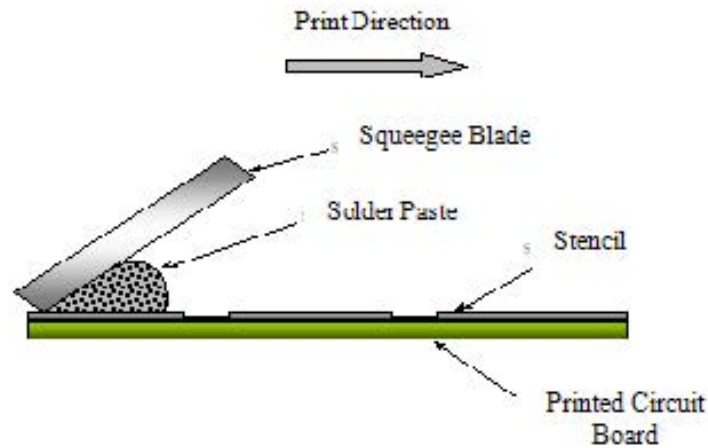


Figure 2.23: Squeegee printing solder paste onto a stencil [19].

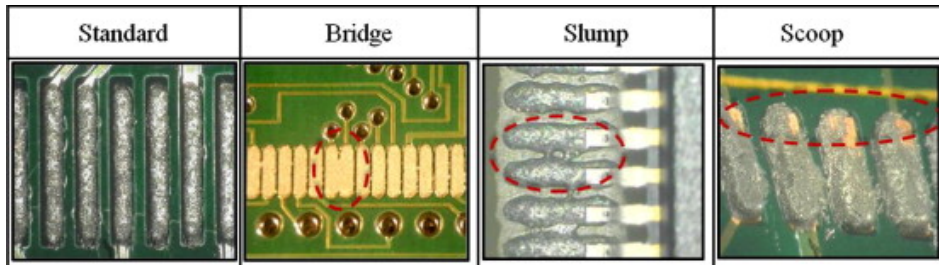


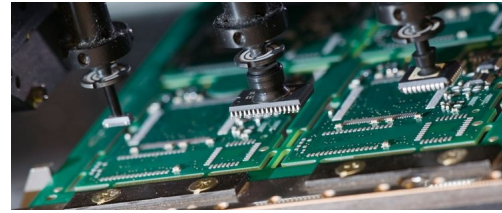
Figure 2.24: Outcomes of solder paste printing [19].

dedicated inspection machines use 3D technology to ensure more thorough inspection including the solder volume. Figure 2.24 shows few examples of outcomes of solder paste printing.

- Step 2: Component pick and placement - This process is automated such that the machine picks appropriate components from the feeders, to be placed on the corresponding copper pads on the PCB. Generally there are five basic types of feeders that include tape feeders, bulk feeders, tray feeders and wafer feeders. Figure 2.25a shows some examples of component feeders. There is a wide range of pick and place machines based on different parameters including placement speed, accuracy, types of feeders, mechanical action, serviceable board sizes and inspection capabilities [66]. Figure 2.25b shows components being picked and placed on the board. After the components are placed, the board is inspected using automated optical inspection machine, before reflow soldering. The machine checks for the component presence, value/type and polarity [66]. If an errors remains undetected, that could lead to a large volumes of rework.



(a) Different component feeders.



(b) Pick and place machine.

Figure 2.25: Component pick and placement [19].

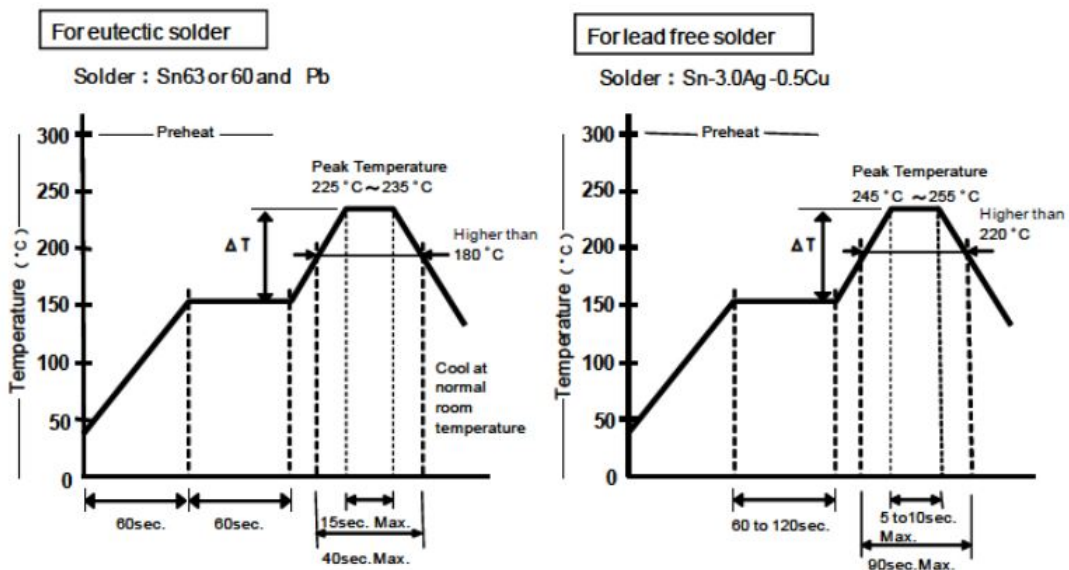


Figure 2.26: Typical reflow profile for lead based and lead-free alloys.

- Step 3: Reflow process - Once the component placement is inspected, the entire SMT assembly is exposed to controlled heat in a reflow oven in order to melt the solder paste and form a permanent solder joint between the component and the copper pad. The reflow oven consists of multiple zones that could be individually temperature controlled. The PCB moves on a conveyor belt through multiple zones in the reflow oven, thereby subjected to controlled time-temperature profile [67]. Figure 2.26 shows reflow profile for different types of solder alloys. A typical reflow profile consists of four stages [68].

1. Preheat - In this phase the assembly is heated to a target soak or dwell temperature at a slow rate of less than 2°C/second. Higher ramp rate might cause the components to crack or the solder paste to splatter.

2. Soak - In this phase, it is ensured that all the components are at the required temperature before the reflow process. At this stage, the solder flux is activated and the solder paste volatiles



Figure 2.27: Reflow oven [20].

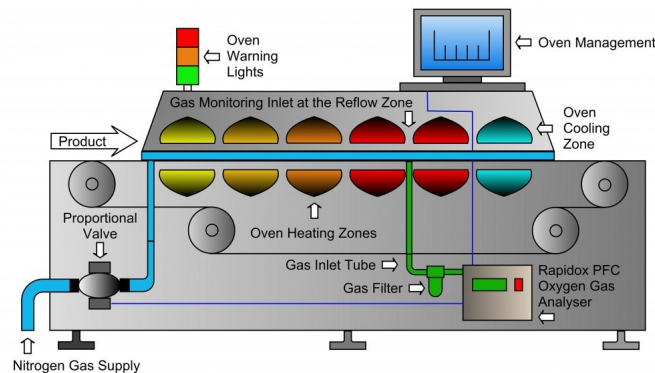


Figure 2.28: Multiple zones in a reflow oven [21].

are removed and it lasts for 20 to 120 seconds depending on different parameters. At the end of this phase, thermal equilibrium of the entire assembly is desired.

3. Reflow - This phase is also called as “time above liquidus” (TAL), where the temperature of the oven is raised above the melting point of the solder paste. It is held at this temperature for about 30 to 60 seconds to enable the proper wetting of the solder paste. The peak reflow should be controlled to prevent component failures and other defects.

4. Cooling - At this phase, the assembly is cooled allowing the solder joints to solidify. The recommended cooling rate is less than 4°C/second. Figure 2.27 and Figure 2.28 show the reflow oven and the multiple zones present in the oven, respectively.

- Step 4: Inspection and testing - The last part of the SMT process is to check that there are no mistakes by using an automated optical inspection machine. The advent of 3D technology has improved the reliability as it allowed more accurate measurements to be taken and a more stable inspection process. These inspection machines could also be networked together for instant feedback to the preceding machine to enable automatic adjustments. Figure 2.29 shows schematic for a typical SMT assembly production line.

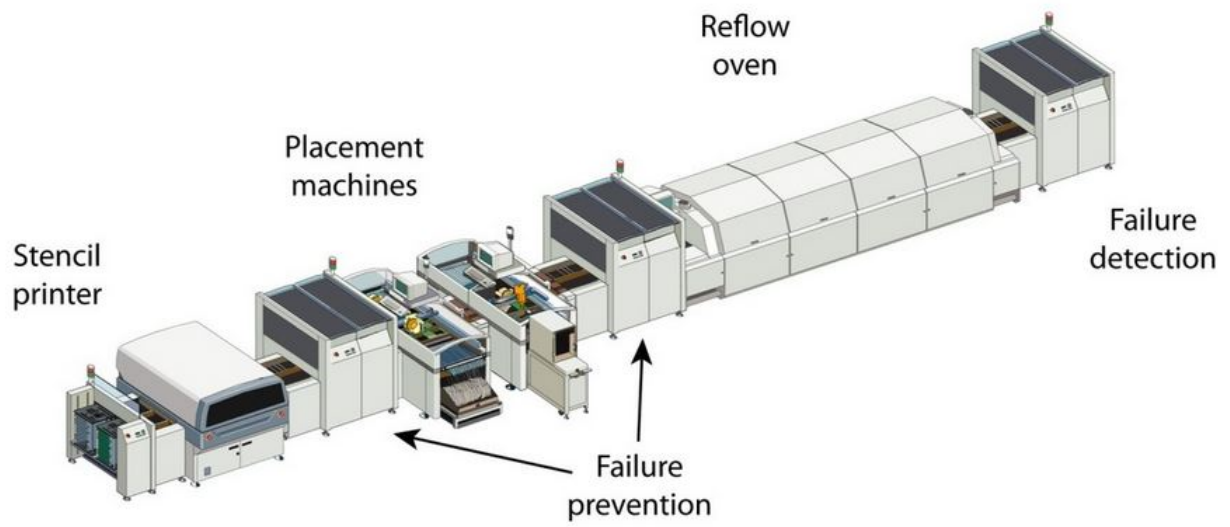


Figure 2.29: Typical SMT assembly production line [22].

Chapter 3

Literature Review

3.1 Reliability of Pb-Free Solder Joints

Solder joint reliability could be defined as the ability of electronic product's solder joints to function for a specified period of time under given conditions without exceeding acceptable failure levels. Once one solder joint fails, the product is rendered useless. So, reliability testing of solder joints is a crucial part in the electronics packaging industry. Thermal cycling is one of the most popular reliability tests. Other reliability tests include thermal shock, mechanical shock, vibration testing, and power cycling. When symptoms of aging are found, the tests are conducted.

3.2 Thermal Reliability

In real world applications, the solder joints are subjected to thermal cycling, especially in under the hood automotive applications. In normal automotive application, the joints are subjected to five to six thermal cycles. So, the thermal reliability is tested through accelerated life testing, where the joints are subjected to extreme thermal cycles compared to the normal conditions. In the study by George et al. [4], the thermal profile used was from -40°C to $+185^{\circ}\text{C}$ with Quad Flat Packages (QFP) and two types of BGAs (144 I/O and 256 I/O). The study concluded that smaller BGAs were more reliable than the large BGAs. Among the surface finishes, ENIG performed better than others. The main cause of failure was due to thermo-mechanical fatigue resulting from CTE mismatch. In BGA packages, the failure location was at the package-solder interface as it is the narrowest section and hence has the maximum stress. Figure 3.1 shows the

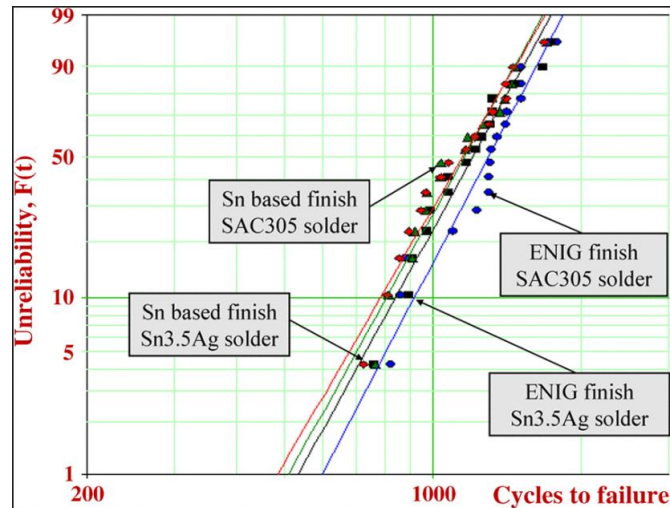
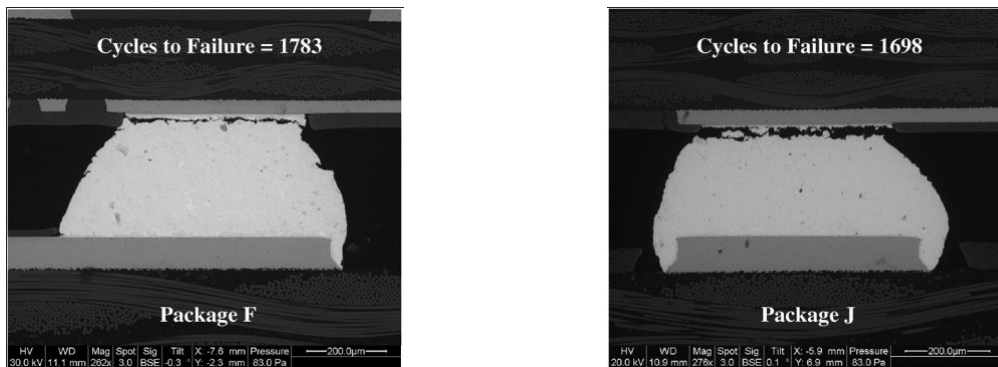


Figure 3.1: Weibull analysis for surface finishes for 2156 I/O BGAs [4].



(a) 256 I/O BGA with ENIG and SAC305.

(b) 144 I/O BGA with ENIG and Sn3.5Ag.

Figure 3.2: Package side crack [4].

the Weibull analysis for different surface finishes for 256 I/O BGAs. The crack locations for packages are shown in Figure 3.2a and Figure 3.2b.

Coyle et al. [23] studied the effect of multiple reflows and the dwell times on the characteristic fatigue life of PBGAs. The fatigue life degrades with longer dwell times and multiple reflows as shown in the Weibull plot of Figure 3.3. In the microstructure analysis of 10 minute dwell samples, more coarsening was found in the case of two reflows. But, for 60 minute dwell samples, the coarsening was comparable between both reflows. This group also studied the influence of the initial microstructure on the fatigue life of the component. It was found that the initial SAC morphology was less of a factor as the thermal cycling exposure increased.

In a study conducted by Teo et al. [24], the BGA components were thermal cycled from -40°C to $+125^{\circ}\text{C}$. It was found that the SAC based solder alloy had better fatigue life than SnPb

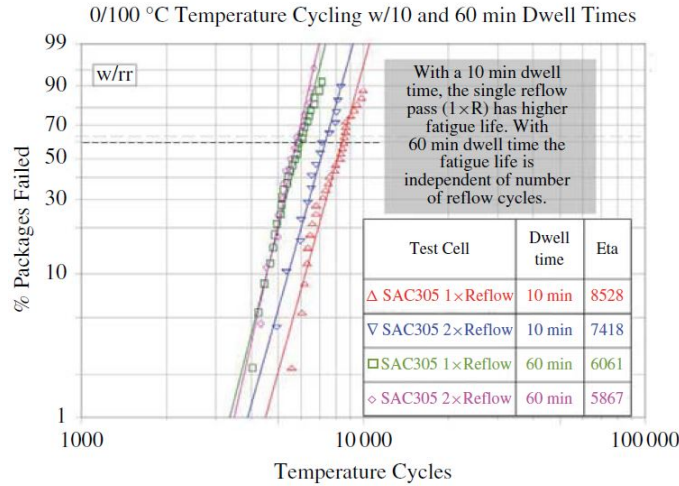


Figure 3.3: Weibull analysis for SAC305 PBGA for multiple reflows and temperatures [23].

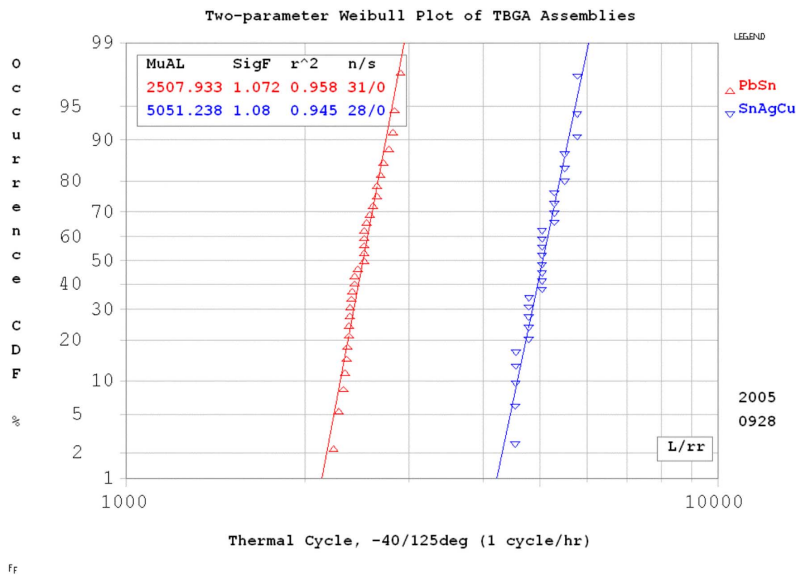


Figure 3.4: Weibull analysis for SnPb and SAC solder TBGA assemblies [24].

alloy as shown in Figure 3.4. This was due to the inelastic deformation during low temperature regime and high creep resistance at high temperature regime of the SAC alloy.

Zhang et al. [25] extensively studied the effect of thermal aging on the thermal cycling reliability. The samples were aged at 25°C, 55°C, 85°C and 125°C for periods of 0 months, 6 months and 12 months, respectively. It was found that the characteristic fatigue life degraded at higher aging temperatures and for smaller solder ball size. Among SnPb, SAC105 and SAC305 solder joints, SAC105 had the least reliability after aging. Figure 3.5 shows the Weibull analysis for 19mm SAC305 BGAs with ImAg surface finish and Figure 3.6 shows the summary of characteristic life for different aging periods.

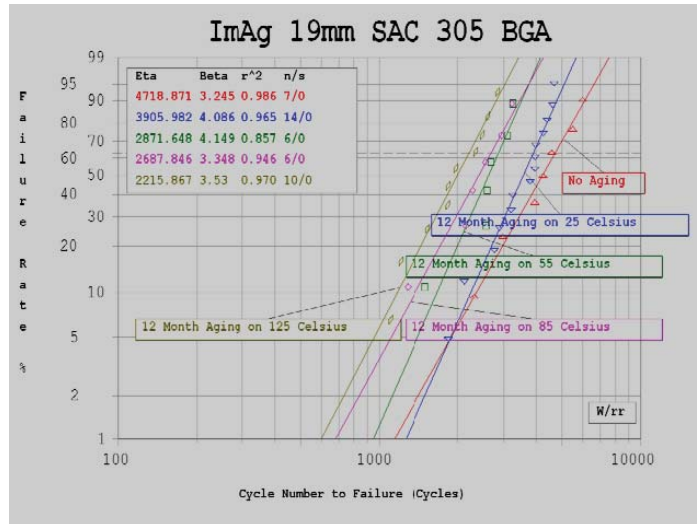


Figure 3.5: Weibull analysis for SAC305 BGA for different temperatures [25].

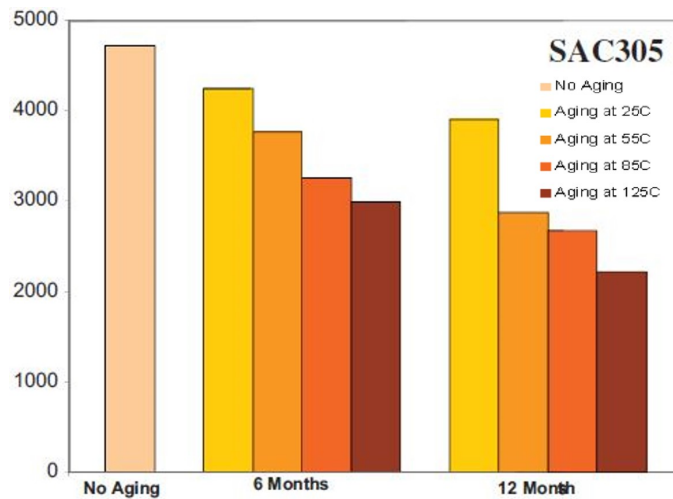


Figure 3.6: Summary of characteristic life for SAC305 BGA for different aging duration [25].

Figure 3.7 shows the evolution of SAC305 microstructure at different points of aging. As it could be seen in the figure, the Ag₃Sn particles get coarsened with aging.

3.3 Other Reliability Tests

Along with thermal cycling, there are other accelerated tests such as drop, vibration, low fatigue cycling, power cycling, etc., which are carried out to study the reliability of lead free solder joints.

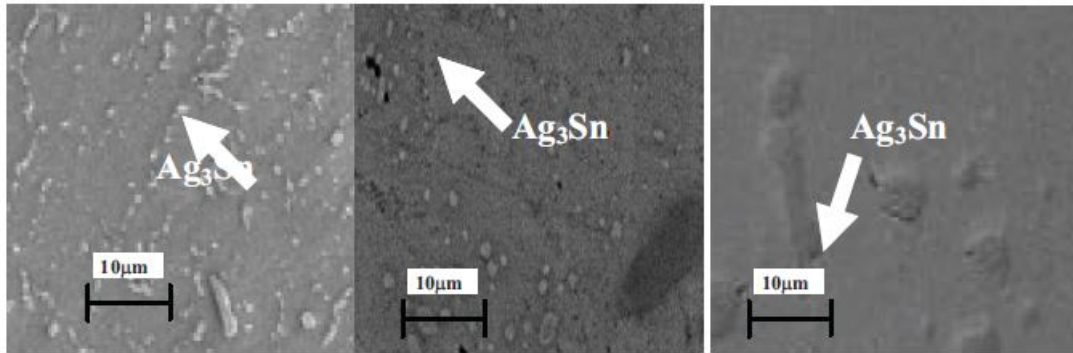


Figure 3.7: SAC305 microstructure evolution during 0, 6 and 12 months of aging [25].

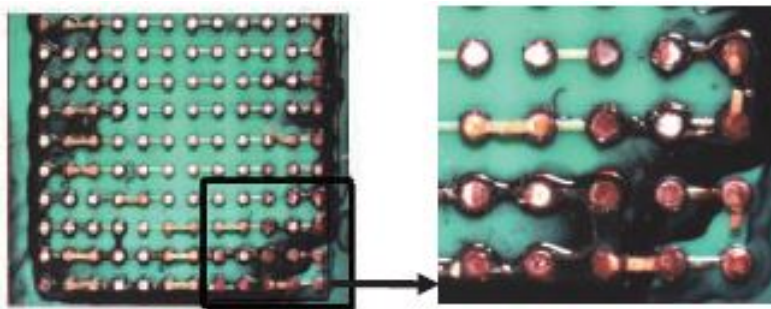


Figure 3.8: Chip fracture surface after dye test [26].

3.3.1 Drop Test

For most of the consumer electronics such as cell phones, laptops, mp3/mp4 players, the expected life is lower than that for military/aerospace/automotive applications. So, the temperature cycling does not play much significant role in their reliability. Most of the times, the failures in these products are caused by vibration and drops during transportation and handling.

Yongping et al. [26], studied the effect of silver content in lead free solders on the drop reliability. SAC based alloys, namely SAC105, SAC305 and SAC0307, were included in the study. Half sine wave acceleration with a peak 3,200g and 1ms duration was used in the test. It was found that the peripheral spheres failed first as shown in Figure 3.8 and that in most of the solder joints the cracks were on the PCB side. It was concluded that drop resistance decreases with increase in Ag content as shown in Figure 3.9. The IMC layer thickness was also found to have increased with the increase in Ag content. The effect of aging and underfills on drop reliability was studied by Liu et al. [69]. They concluded that the underfills increased the reliability in drop tests and that aging decreased the drop reliability.

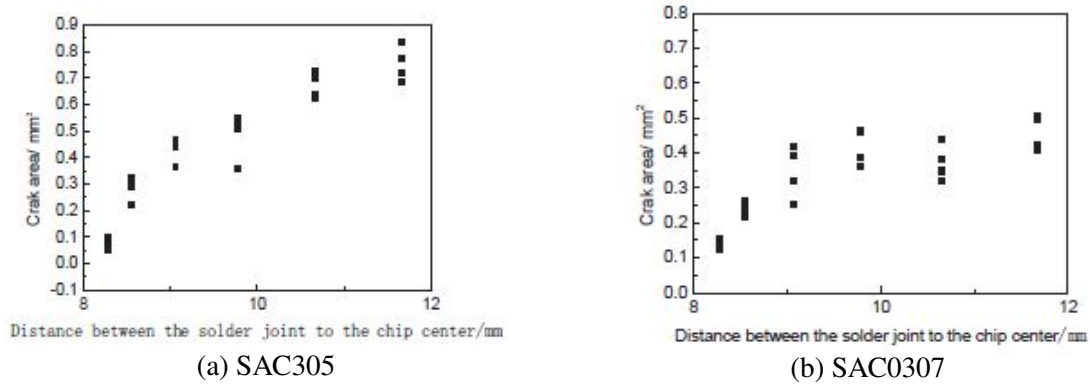


Figure 3.9: Effect of solder joint location and Ag content on the crack area [26].

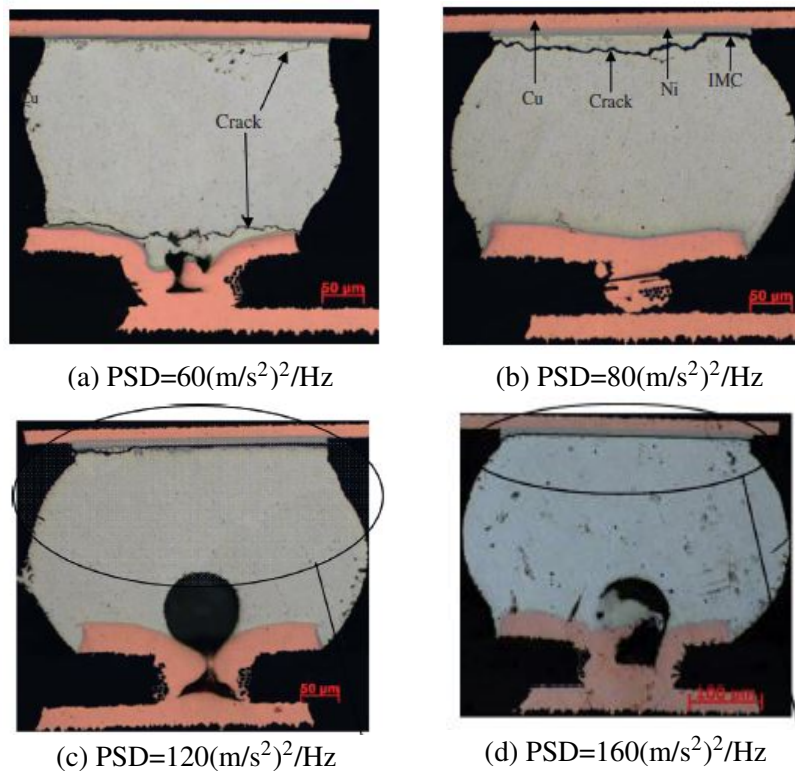


Figure 3.10: Crack location for different acceleration PSD amplitudes [27].

3.3.2 Vibration Test

Liu et al. [27] studied the random vibration reliability of BGA solder joint at different acceleration PSD amplitudes. It was found that the failure modes and propagation rate of cracks changed with the PSDs. The propagation rate of crack increased with increase in acceleration PSD amplitudes. It was also found that with the increase in PSD amplitudes, the location of crack on the solder joint changed from the PCB side to the solder ball neck and finally to the IMC layer interface on the component side. Their images are presented in Figure 3.10.

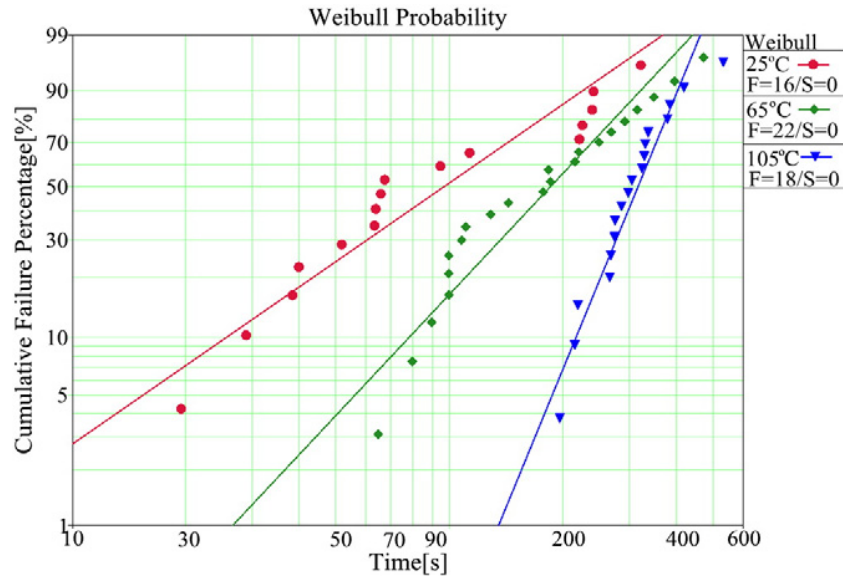


Figure 3.11: Weibull analysis for vibration reliability at different temperatures [28].

In another study by Zhang et al. [28], it was found that the vibration reliability increased with increase in temperature as shown in Figure 3.11. Similar results were published by Libot et al. [29], showing that the components were more likely to fail at -55°C than at 20°C or 105°C due to the embrittlement at low temperatures.

3.3.3 Low Cycle Fatigue Test

Most of the times, the realistic service conditions are not taken into consideration when fatigue cycling test is done at fixed amplitudes. Hamasha et al. [29] conducted low fatigue shear tests with single and varying stress amplitudes considering the effects of strain rate. It was observed that with the increase in strain rate during stress control cycling leads to less work dissipation per cycle and reduced plastic strain, which in turn creates less damage and leads to higher fatigue life as demonstrated in Figure 3.12.

Another similar study was conducted by Su et al. [40], in which they studied the effect of long term room temperature aging on the solder fatigue life. It was found that there was a significant drop in fatigue life after four years of room temperature aging. The solder alloys with elements such as Bi, Ni, Sb and several others micro-alloys, showed relatively less degradation when compared to SAC105 and SAC305. Percentages of degradation for different alloys are listed in Table 3.1.

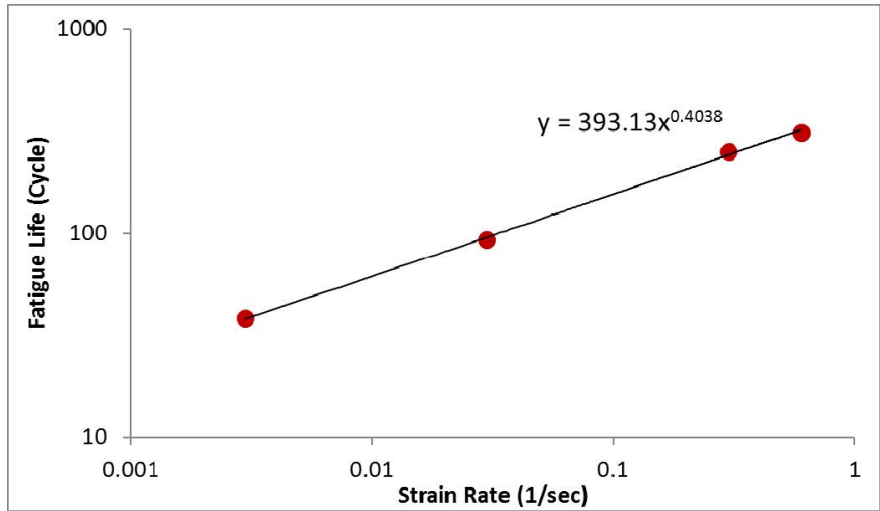


Figure 3.12: Characteristic life of individual SAC305 solder joints cycled at 24 MPa vs. strain rate on log-log scale [29].

	Avg. degradation of characteristic life	Avg. degradation of B10 life
SAC305	60%	53%
SAC105	66%	42%
SAC-Ni	45%	28%
SAC-X-Plus	35%	21%
Innotot	4%	7%

Table 3.1: Degradation of fatigue life after four years of room temperature aging [40].

3.4 Microstructure Evolution

Depending upon the conditions that the solder joints are subjected to, their microstructure evolves over time. Generally, the evolution is such that the stress induced in the solder joints from external thermo-mechanical conditions is relaxed. It was also found that the IMC growth rate was higher for thermal shock than that for thermal-cycled and thermal-aged loading conditions. George et al. [4] mention that the stress imposed on the solder joint during non isothermal aging conditions could be relaxed by the formation of IMC layer, which explains the IMC growth rate difference under thermal shock and thermal cycling tests. The IMC layer is formed during the reflow process. IMC layer strengthens the solder joint, but as it keeps on growing with time, it becomes more brittle and that makes it the location of crack initiation and finally a failure. IMC layer growth rate is accelerated at higher temperatures. Figure 3.13 shows the

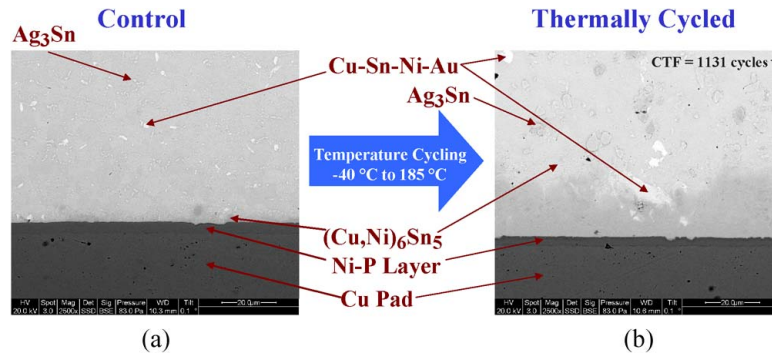


Figure 3.13: IMC growth for control sample and tested sample [4].

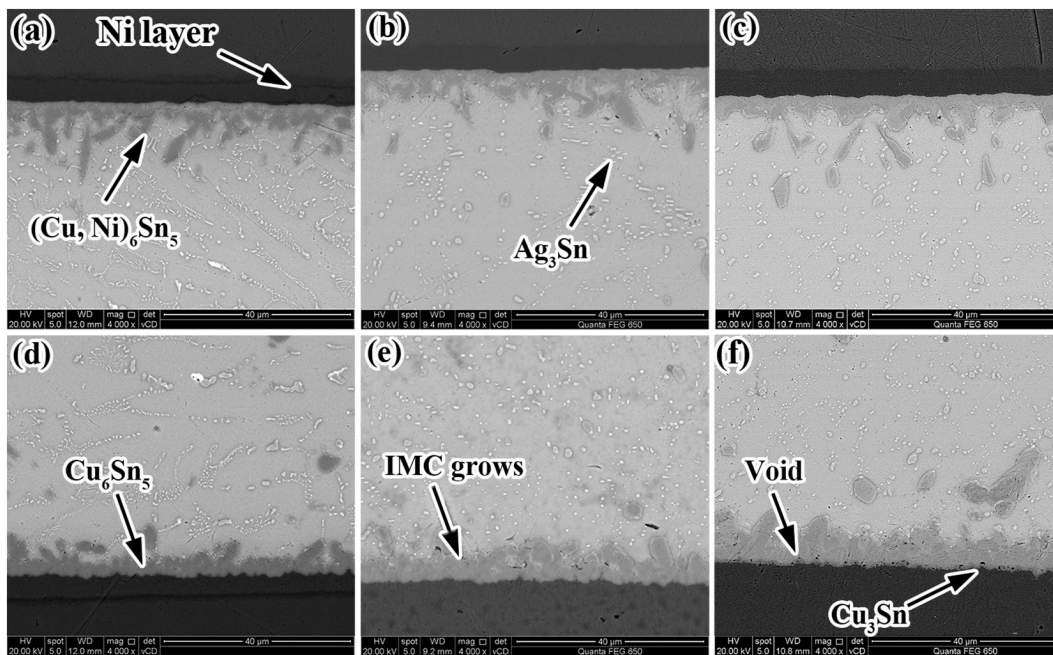


Figure 3.14: Microstructure evolution (a,d) as reflowed, (b,e) after thermal cycling and (c,f) after aging [30].

growth of IMC layer in a sample aged at room temperature for two years (control) and in a thermal cycled sample (tested). From Figure 3.13, in SAC305 soldered BGAs, $(\text{Cu}, \text{Ni})_6\text{Sn}_5$ formed the IMC layer at the solder-board interface. In the bulk solder, Ag_3Sn and Cu-Sn-Ni-Au phase was observed.

In another study by Gu et al. [30], the microstructure evolution during the thermal cycling was studied. The solder joint at the component side and at the board side is shown in the Figure 3.14. Both the package side and the board side consist of $\beta\text{-Sn}$ matrix with dispersed Ag_3Sn particles. The needle shaped structures $(\text{Cu}, \text{Ni})_6\text{Sn}_5$ were found on the package side IMC layer due to the presence of Ni layer. On the board side, the IMC was a more uniform

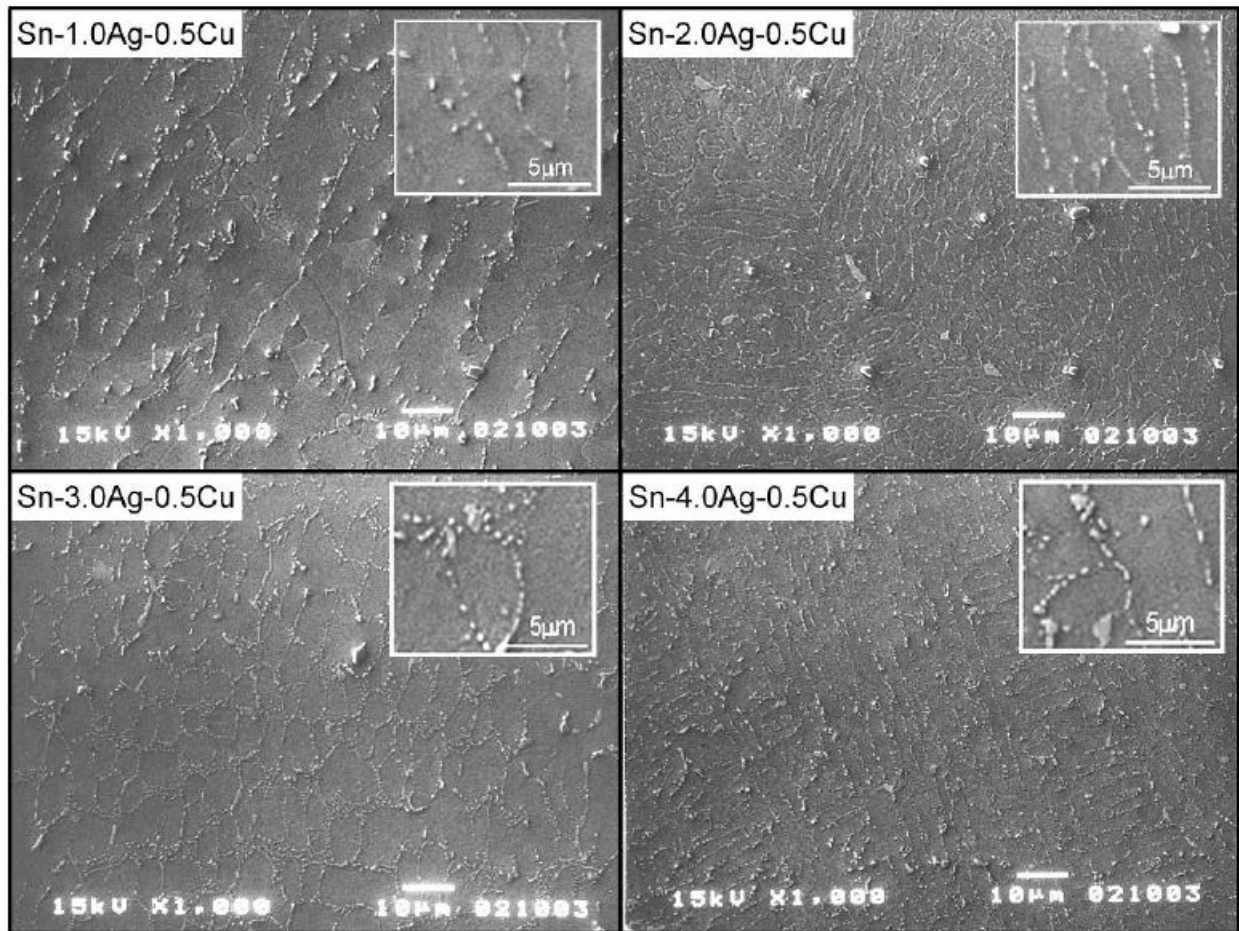


Figure 3.15: Initial microstructure of SAC solder [31].

layer of Cu_6Sn_5 . After thermal cycling, the IMC layer on both sides grows thicker and Ag_3Sn particles grow larger in size and their number decreases. Voids are formed on the board side IMC layer due to the non-equilibrium diffusion of Cu into the bulk solder leading to the formation of Cu_3Sn . On the package side, the presence of Ni prevents the diffusion of Cu. So, the thickness of IMC layer is comparatively smaller on the package side with respect to the board side.

The effects of silver content on the shear fatigue of SAC solder joints were studied by Kariya et al. [31] using SAC105, SAC205, SAC305 and SAC405. The reflowed microstructure is shown in Figure 3.15. All alloys had fine dispersed Ag_3Sn intermetallic compounds with Cu_6Sn_5 within the β -Sn matrix. SAC105 has relatively large Sn grains with more coarsened interparticle spaces of intermetallics. SAC205 has cell like Sn grains decorated with fine IMCs. For SAC305, the IMCs appear around the Sn grains with a network structure and the Sn grains

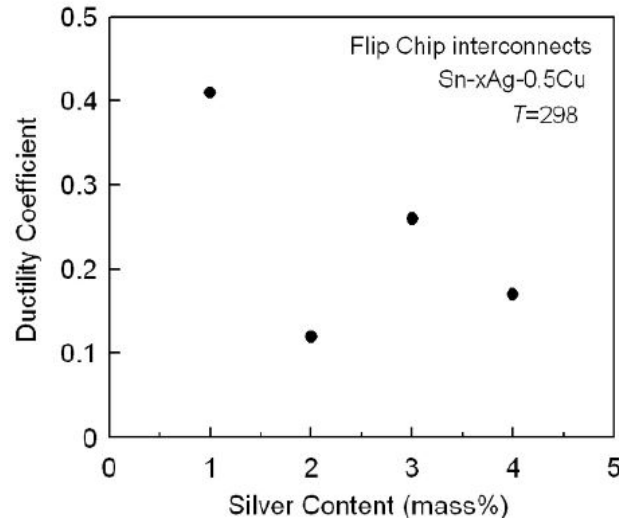


Figure 3.16: Effect of Ag content on ductility [31].

appear to be larger than those of SAC205 solder. In the case of SAC405, the microstructure is very fine and the IMCs appear dense within the matrix, when compared with the other alloys. In general, the interparticle space and the grain size seem to decrease with increasing Ag content, which might increase the strength of the solder alloy. The higher Ag content in the alloy induces comparatively high elastic deformation in the substrate, so that the plastic deformation of the solder sphere is less compared to alloys with low Ag content. Hence, the increase in Ag content is effective in suppressing the deformation of the solder bumps. It was also found that, with the increase in strength, there is a decrease in ductility. Figure 3.16 shows the effect of Ag content on the ductility of the solder alloy.

Figure 3.17 shows the crack propagation in the solder joint. Microstructure coarsening, that degrades fatigue resistance and ductility coefficient could be seen in SAC205. The study concluded that the SAC305 is recommended in flip chip bump for different conditions as the strength and fatigue ductility is well balanced.

Fu et al. [32] studied the effect of aging on the evolution of microstructure using SAC305 solder joint as micro cylinder shaped uniaxial sample. The samples were aged for 20 days at 125°C. The dendrite structure was observed, similar to previous study. This kind of structure

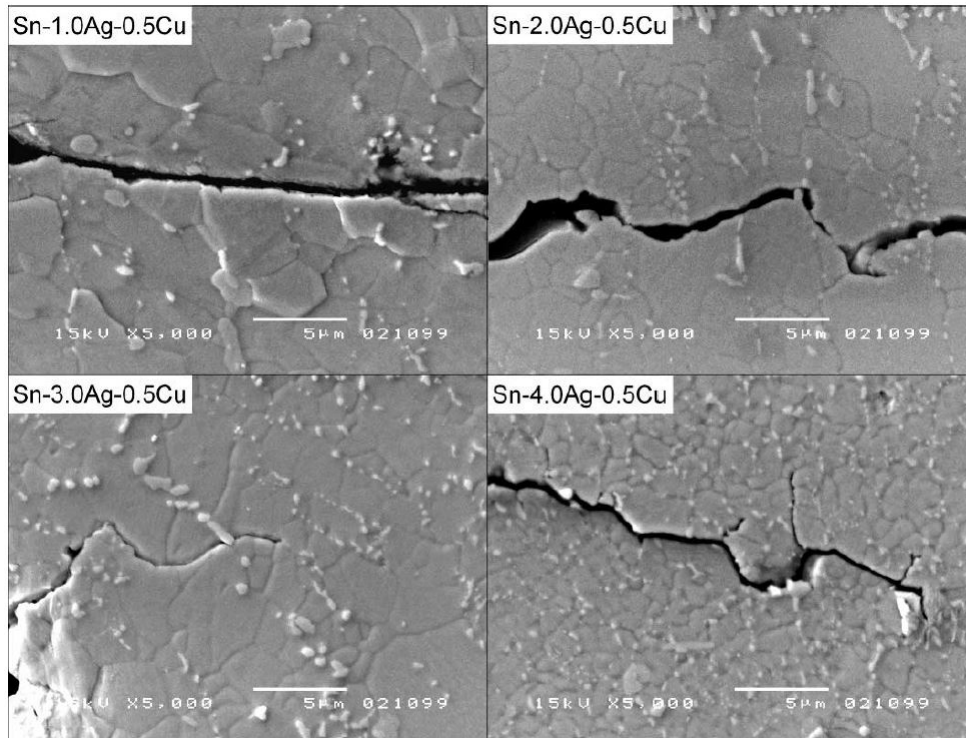


Figure 3.17: Crack propagation in different alloys subjected to shear fatigue test [31].

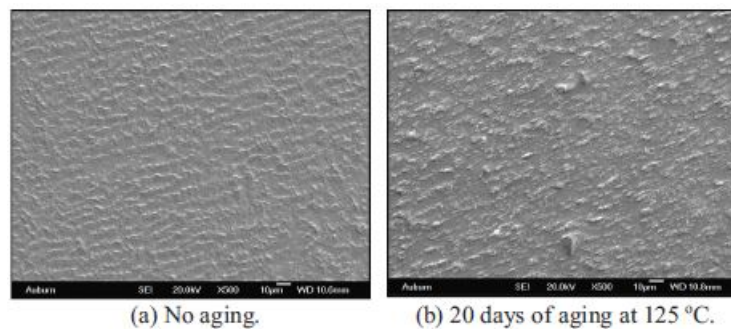


Figure 3.18: Effect of aging on the microstructure of SAC305 [32].

is effective in blocking the dislocation movements. With aging, the dendrite structures disappear and the IMC coalesce and coarsen, which leads to increased dislocation movements. The microstructure before and after aging is shown in Figure 3.18.

3.5 Effect of Dopants

In order to improve the mechanical properties and fatigue resistance, and thereby to mitigate the effect of aging several elements such as Bi, Ni, Co and Sb have been added in very small percentages to SAC based solder alloys. Some elements increase the wettability, whereas some

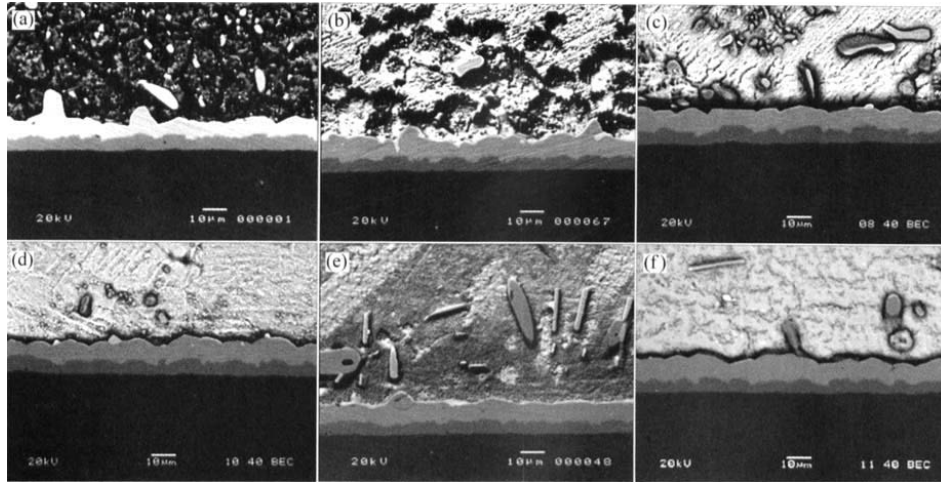


Figure 3.19: SEM images of Sn-3.5Ag-0.7Cu-xBi solder joints aged at 190°C for 400 hours (a)x=0; (b)x=1.0; (c)x=2.0, (d)x=3.0; (e)x=4.0; (f)x=5.0 [33].

form precipitates that block dislocation movements and some decrease the IMC layer growth, thereby increasing the fatigue life.

3.5.1 Bismuth (Bi)

Guo-yuan et al. [33] studied the effect of adding Bi to the SAC based lead free solder alloy. The samples were reflowed at a peak temperature of 250°C for 60 seconds and then aged at 120°C, 150°C, and 190°C for periods of 0, 200, 400, 600, 800 and 1,000 hours. Figure 3.19 shows the effect of adding Bi to SAC solder, after aging for 400 hours at 190°C. It was observed that the thickness of the IMC layer decreased with the increase in Bi composition till 2.0%. But after this point, the IMC thickness increases. It was also found that the growth rate was the lowest at 1.0% Bi and the explanation was that the mutual solubility of Sn and Bi increases with the increase in temperature that leads to finer particles precipitated on the grain boundary preventing the diffusion of Sn and Cu atoms across the IMC layer. Another conclusion was that the activation energy of Sn-3.5Ag-0.7Cu-xBi was the highest at x=1 as shown in Figure 3.20, which indicates reduced rate of atomic diffusion. In another study by El-Daly et al. [34], the effect of Bi on other characteristics of SAC alloy, such as melting point, creep resistance and microstructure was studied. Sn-1.5Ag-0.7Cu-xBi where x=1,3 alloys were used in the study. SAC-3Bi had melting temperature that was around 6.8°C lower than that of the SAC alloy used in the study. As shown in Figure 3.21, with the addition of Bi, the microstructure changed from

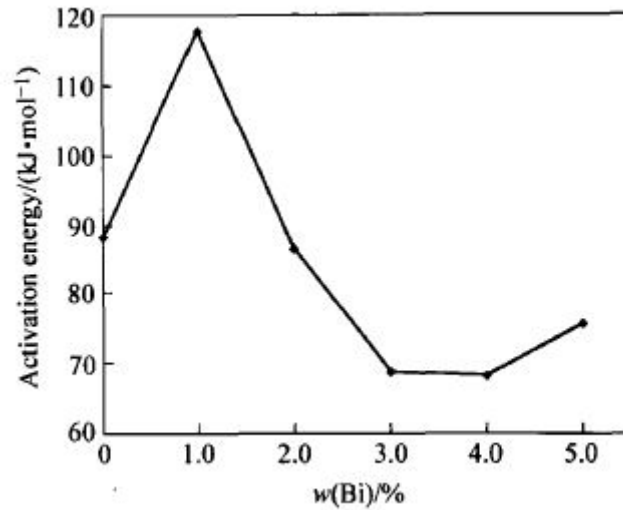


Figure 3.20: Effect of Bi on activation energy [33].

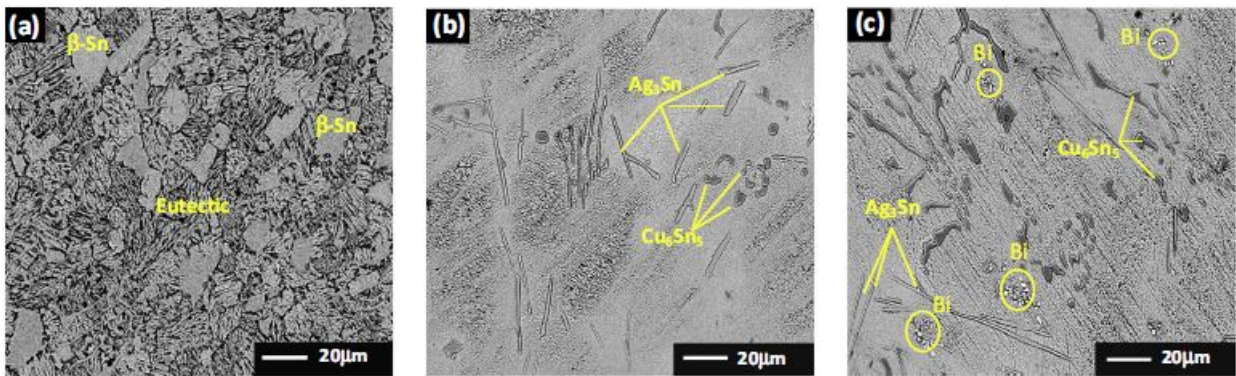


Figure 3.21: SEM microstructures of (a)SAC-0.0Bi (b)SAC-1.0Bi (c)SAC-3.0Bi [34].

large number of primary β -Sn grains surrounded by eutectic regions to a large number of small needle shaped Ag_3Sn and dark gray Cu_6Sn_5 particles. It was also found that the addition of Bi increased the creep resistance of SAC alloy without Bi as shown in Figure 3.22, which could be attributed to the solid solution strengthening effect of Bi atoms and Bi precipitates.

3.5.2 Antimony (Sb)

In the study conducted by Li et al. [35], the effect of adding Sb to SAC alloy was studied with Sn-3.5Ag-0.7Cu lead free solder joints. The SEM micrographs of Figure 3.23 show that the grain size of IMC layer is smaller when Sb is added, which improves the mechanical properties. From Figure 3.23(a) a trace of a disappearing grain boundary could be seen, and from Figures 3.23(b) and (c), it could be seen that different small grains coalesce to form larger

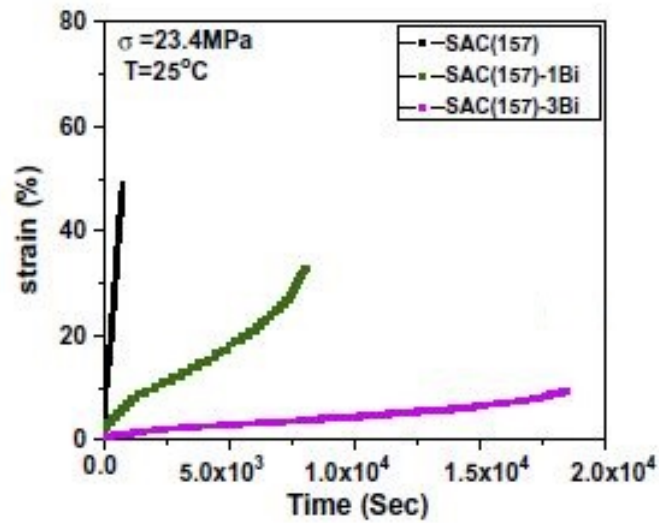


Figure 3.22: Effect of %Bi on creep rate [34].

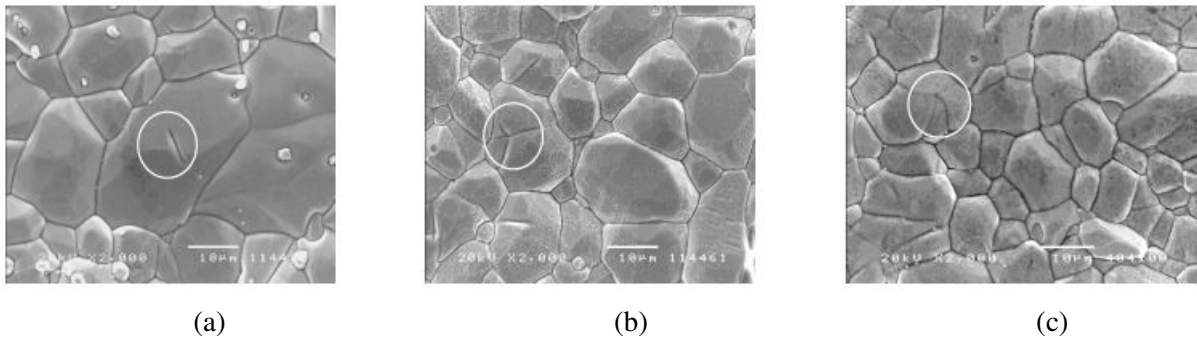


Figure 3.23: SEM images of top view of IMC layer of Sn-3.5Ag-0.7Cu-xSb solder joints aged at 190°C for 600 hours (a)x=0; (b)x=0.2; (c)x=0.8 [35].

grains. Similar to the case of Bi addition, even in the case of Sb addition, Cu_6Sn_5 IMC layers had a scallop-type appearance at the beginning of aging, which later transforms to comparatively even layer with aging. From Figure 3.24, it could also be seen that Cu_3Sn layer is developed with aging.

The authors give a similar explanation as in the case of Bi addition that the IMC layer has the lowest thickness when 0.8% of Sb is added at this composition, the SAC-xSb has the highest activation energy as shown in Figures 3.25a and 3.25b.

3.5.3 Nickel (Ni)

Addition of Ni to SAC alloys appeared to have suppressed most of the Cu_3Sn [70]. With 5-15 at% Ni, an increased growth rate of $(\text{Cu,Ni})_6\text{Sn}_5$ was observed, in addition to the absence

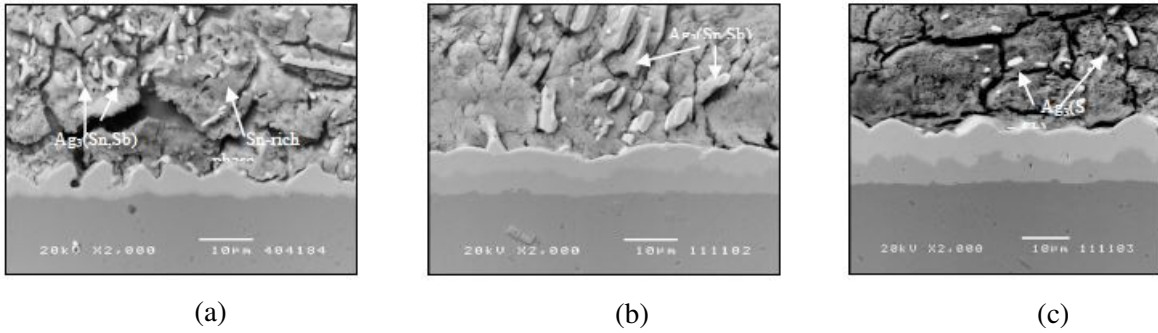
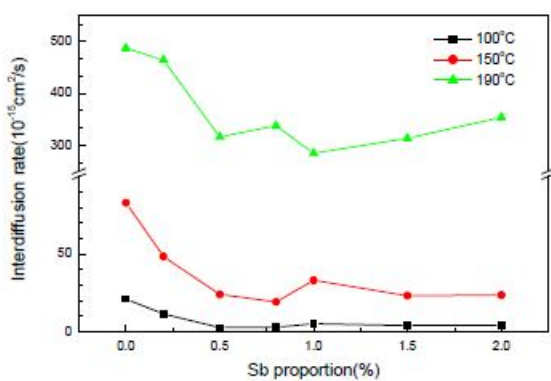
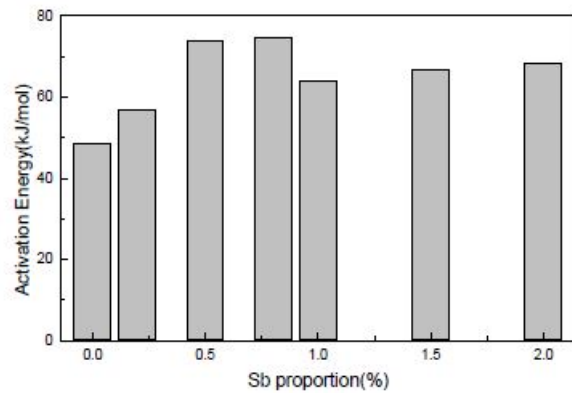


Figure 3.24: Backscattered SEM micrographs of cross-sectional view of Sn-3.5Ag-0.7Cu-1.0Sb solder joints aged at 190°C for (a) 1 hour, (b) 200 hours, and (c) 600 hours [35].



(a) Effect of %Sb on the IMC growth rate.



(b) Effect of %Sb on activation energy.

Figure 3.25: Different characteristics affected [35].

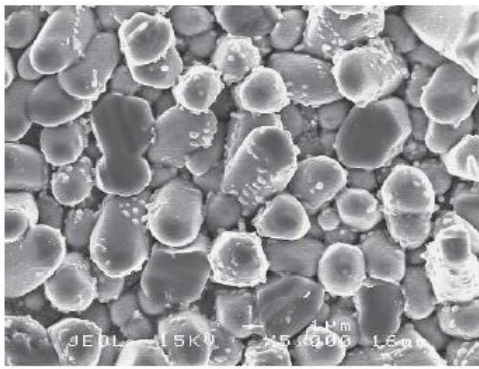
of Cu_3Sn . It was also found that when Cu was alloyed with 5-15 at%, the grain size of the $(\text{Cu},\text{Ni})_6\text{Sn}_5$ was more than one magnitude smaller than that of pure copper. With regards to Cu_3Sn , similar observation was made by Gao et al. [36]. In their research, it was found that Cu_3Sn phase existed when the aging temperature was more than 130°C as shown in Table 3.2.

The site 1 mentioned in the Table 3.2 is located in upper intermetallic region adjacent to the solder matrix, site 3 was close to the interface of intermetallic-Cu to probe the Cu_3Sn phase and site 2 is located in the middle of sites 1 and 2.

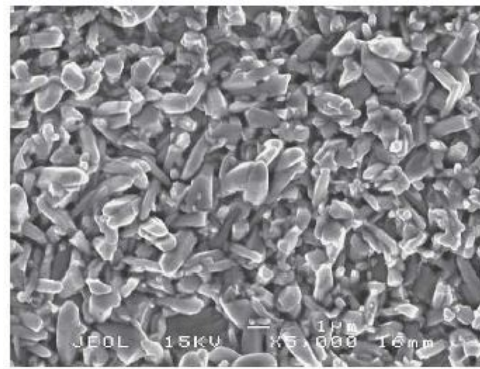
Another interesting fact from the top view SEM micrographs of intermetallics as shown in Figure 3.26 was that the IMC formed between Sn-Ag-Co-Ni solder and Cu was extremely refined, indicating that the grain coarsening was significantly suppressed.

Sn-3.5 Ag-0.2Co-0.1Ni	Sites	Composition (At.%)				Phases
		Sn	Cu	Ni	Co	
No aging	1	46.2	43.3	5.1	5.4	$(\text{Cu}_{(1-x-y)}, \text{Co}_x, \text{Ni}_y)_6\text{Sn}_5$
	2	46.3	51.8	1.2	0.7	$(\text{Cu}_{(1-m-n)}, \text{Co}_m, \text{Ni}_n)_6\text{Sn}_5$
	3	46.0	53.3	0.5	0.2	$(\text{Cu}_{(1-x-y)}, \text{Co}_x, \text{Ni}_y)_6\text{Sn}_5$
110°C	1	45.7	44.8	4.4	5.1	$(\text{Cu}_{(1-x-y)}, \text{Co}_x, \text{Ni}_y)_6\text{Sn}_5$
	2	44.8	53.1	1.4	0.7	$(\text{Cu}_{(1-m-n)}, \text{Co}_m, \text{Ni}_n)_6\text{Sn}_5$
	3	45.6	53.8	0.4	0.2	$(\text{Cu}_{(1-x-y)}, \text{Co}_x, \text{Ni}_y)_6\text{Sn}_5$
130°C	1	46.7	46.9	2.5	3.9	$(\text{Cu}_{(1-x-y)}, \text{Co}_x, \text{Ni}_y)_6\text{Sn}_5$
	2	47.2	51.6	0.5	0.8	$(\text{Cu}_{(1-m-n)}, \text{Co}_m, \text{Ni}_n)_6\text{Sn}_5$
	3	25.5	74.5	—	—	Cu_3Sn
150°C	1	45.7	48.9	1.7	3.7	$(\text{Cu}_{(1-x-y)}, \text{Co}_x, \text{Ni}_y)_6\text{Sn}_5$
	2	46.1	52.6	0.4	0.9	$(\text{Cu}_{(1-m-n)}, \text{Co}_m, \text{Ni}_n)_6\text{Sn}_5$
	3	25.7	74.3	—	—	Cu_3Sn

Table 3.2: Chemical compositions of IMC determined by EPMA [36].



(a) Sn-3.5Ag/Cu



(b) Sn-3.5Ag-0.2Co-0.1Ni/Cu

Figure 3.26: Comparison of intermetallic morphology (top view), reflow at 250°C for 1 min [36].

3.5.4 Cobalt (Co)

Research has found that adding Co improves the ductility [71], improve thermal fatigue and creep resistance [38] and reduces brittle failures [72]. As in the case of Ni, Co also tends to suppress the growth of Cu_3Sn [37]. As seen in Figure 3.27, with the addition of Co, the IMC layer appears to have a flat morphology compared to the one with SAC alloy. It could also be seen that the thickness of Cu_3Sn layer is smaller for solder with Co. More concentration of Co as $(\text{Cu},\text{Co})_6\text{Sn}_5$ was observed in the upper region of the IMC layer than inside of the layer. The interdiffusion coefficient D_{eff} of each IMC layer could be determined by using the equation:

$$x_t - x_0 = (D_{\text{eff}})^{1/2} \quad (3.1)$$

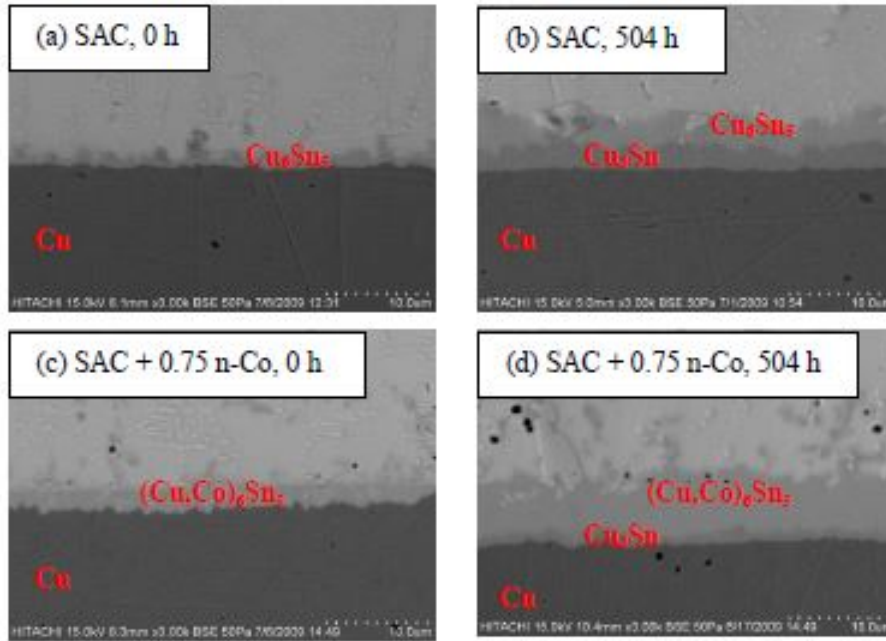


Figure 3.27: SEM images of solder-substrate interface after aging for 0 and 504 hours at 1150°C [37].

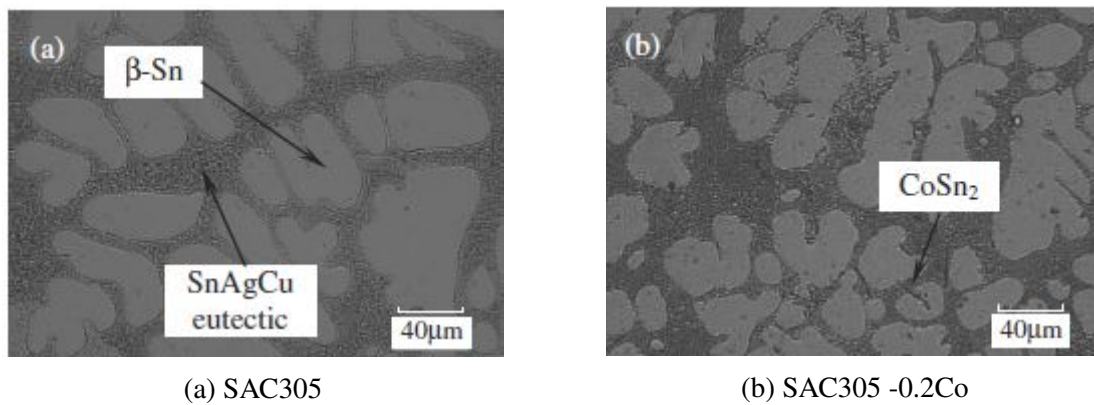


Figure 3.28: Comparison of microstructure as-cast condition [38].

where x_t is the thickness of IMCs at time t and x_0 is the IMC thickness after reflow. After the addition of Co nanoparticles, the interdiffusion coefficient for Cu_3Sn is much smaller in SAC+0.75 n-Co composite when compared to normal SAC alloys, which would explain the thin Cu_3Sn layer.

Cheng et al. [38] report finding a new intermetallic compound CoSn_2 with the addition of Co as shown in Figure 3.28. Microstructural coarsening was also found with aging, in the case of SAC alloy and SAC alloy with Co addition.

3.6 Fatigue Models

The increase of the fatigue damage with applied loads in a cumulative manner will lead to the failure of materials [73]. With the amount of damage accumulated, the lifetime under certain loads becomes limited. Therefore, it is important to study the mechanism of damage accumulation in the material that results in the failure. Comprehensive reviews about the damage accumulation theories have been conducted earlier by Fatemi et al. [74]. Linear damage cumulative theory predicts that the damage caused by a stress cycle that is independent of its load sequences and assumes the ratio of damage accumulation is also independent of the stress level. Linear damage models are used due to their simplicity and close approximation to reality [75].

Among many of those models, the Miner's rule has been extensively utilized to estimate the fatigue life exposed to cyclic loading conditions with varying stress amplitudes [73]:

$$\sum_{i=1}^k \frac{n_i}{N_i} = 1 \quad (3.2)$$

where n_i is the number of cycles accumulated at a given stress amplitude, N_i is the number of cycles to failure at the same stress amplitude, and k indicates the number of stress levels. Moreover, several modifications of Miner's rule have also been provided by Grover and Gratts [76, 77]. They provide a two-phase damage model that counts damage evolution as a combination of crack initiation and crack propagation.

For crack initiation:

$$\sum \frac{n_i}{\alpha N_i} = 1 \quad (3.3)$$

For crack propagation:

$$\sum \frac{n_i}{(1 - \alpha)N_i} = 1 \quad (3.4)$$

It has been proved recently by Hamasha et al. and others [78, 79] that Miner's rule is not valid for predicting the fatigue life of lead-free solder joints. They give the reasons as: 1. Lead-free solder material is stress dependent, which means that the accumulated damage after specified fraction of fatigue life is different for different stress amplitudes. However, Miner's rule assumes the material is stress independent; 2. Lead-free solder material is damage

interactive, which means that the way damage is accumulated could be changed by previously applied stress. However, Miner's rule assumes that the material is free of damage interaction. Corten and Dolan provided a non-linear accumulative damage model to account for the effects of load interaction during fatigue cycling [80]. It assumes that the damage accumulation is nonlinear and can be expressed in terms of the number of cycles in a power law equation, and the damage can propagate at both high and low stress amplitudes that are applied to the material. The damage accumulation according to the Corten-Dolan model is expressed as:

$$\sum_i \left(\frac{n_i}{N_1} \right) \left(\frac{\sigma_i}{\sigma_1} \right)^d = 1 \quad (3.5)$$

where N_1 is the fatigue life at the highest stress amplitude σ_1 , n_i is the number of cycles at stress amplitude σ_i and d is the material constant for the model.

According to Corten-Dolan model, material constant d should be constant for all materials. However, results indicate that the exponent d is smaller at higher maximal stress than at lower stress [81]. Many researchers have focused on determining the value of d in order to make Corten-Dolan model more accurate and effective [26, 81]. Zhu et al. [81] proposed a "dynamic" Corten-Dolan equation, where exponent d is defined as a function that decreases with the increasing loading stress amplitude:

$$d(\sigma_i) = \mu \frac{\sigma_i^\lambda \delta_f^{1-\lambda}}{\sigma_i} \quad (3.6)$$

where λ is load-interaction factor, μ is material constant, σ_i is i th level stress amplitude, and δ_f is initial static strength. Therefore, fatigue life of Corten-Dolan model could be rewritten as:

$$N_g = \frac{N_1}{\sum_{i=1}^k \alpha_i \left(\frac{\sigma_i}{\sigma_1} \right)^{d(\sigma_i)}} \quad (3.7)$$

where N_g is number of cycles to failure and N_1 is number of cycles to failure at σ_1 .

By combining the concept of Miner's rule (linear damage theory) with Corten-Dolan theory (stress interactive theory), Hamasha et al. [79] proposed a modification of Miner's rule for

combination of two alternating amplitudes:

$$1 = \sum_{i=0}^s f(i) \frac{n_{mi}}{N_m} + \frac{n_{hi}}{N_h} \quad (3.8)$$

where n_{mi} is the number of cycles at low amplitude, N_m is the life at low amplitude, n_{hi} is the number of cycles at high amplitude and N_h is the life at high amplitude. The amplitude factor $f(i)$ is the hysteresis energy in the low amplitude cycles after exposure to i sets of n_{hi} high amplitude cycles divided by the hysteresis energy in the low amplitude cycles before it gets exposed to high amplitude cycles.

Cheng et al. [82] came up with a model based on continuum damage mechanics and ductility exhaustion using a pressure vessel steel (16MnR) alloy for verification. In the first part, the specimens were subjected to single level constant stress amplitude. In the second part, the specimens were subjected to two levels of stress: a stress amplitude for a number of cycles and then lower stress amplitude for a given number of cycles. Damage variable related to ductility exhaustion has been successfully used to predict cyclic damage evolution and this variable is expressed by,

$$D = 1 - \frac{\tilde{\epsilon}_f}{\epsilon_f} \quad (3.9)$$

where ϵ_f is the fracture strain of the uncycled material and $\tilde{\epsilon}_f$ is the residual strain after n loading cycles. Here, $\epsilon_f = \ln\left(\frac{1}{1-\Psi}\right)$, where Ψ is original reduction of section area and $\tilde{\Psi}_f$ is the residual reduction of area after n cycles. In their work, the fatigue damage evolution equation is expressed as:

$$D = D_c \left\{ 1 - \left[1 - \left(\frac{n_i}{N_i} \right)^{\frac{1}{1-\Psi}} \right]^{\frac{1}{1+\beta}} \right\} \quad (3.10)$$

where D_c is the critical damage value that corresponds to the development of 1mm long crack in the material. Fatigue failure will occur when damage (D) reaches or exceeds D_c .

N_i is the fatigue life defined by the number of cycles to form critical crack:

$$N_i = \left[(1 + \beta) (1 - \Psi) \left(\frac{\Delta\sigma}{A(R)} \right)^\beta \right]^{-1} \quad (3.11)$$

There are two methods to forecast the structure fatigue life: one is fatigue life prediction based on fatigue cumulative damage theories and the other is damage tolerance method based on fracture mechanics. In the work by Wang et al. [83], brittle fatigue damage model is modified and combined with damage constitutive model to predict the fatigue life of titanium alloy components. The degeneration of material mechanical properties results from nucleation, growth, and integration of microcracks and voids within metal material. Thus, for one-dimensional structure, a damage variable can be defined as:

$$D = \frac{S_D}{S} \quad (3.12)$$

where S is the total area of cross section and S_D is the total area of micro cracks and cavities. By applying strain equivalence theory after damage initiation, the constitutive relation of material can be defined under state of one dimensional stress as:

$$\epsilon = \frac{\tilde{\sigma}}{E_0} = \frac{\sigma}{E_0(1-D)} \quad (3.13)$$

where $\tilde{\sigma}$, E_0 and ϵ are the true stress of damaged material, the initial elasticity modulus of material and the elastic strain, respectively. $D = 0$ means the material is undamaged and $D = 1$ means material is damaged. The damage evolution model is expressed as,

$$\frac{dD}{dN} = \frac{\bar{B}}{q(1-D)^{2q}} \left(\sigma_{eqM}^{2q} - \sigma_{eqm}^{2q} \right) \quad (3.14)$$

where \bar{B} and q are material constants, σ_{eqM} is maximum equivalent stress of loading and σ_{eqm} is the minimum equivalent stress. In their paper, Wang et al. have applied the model by using FEM to smooth and notched specimens and predicted the fatigue life at the given stress level.

Chapter 4

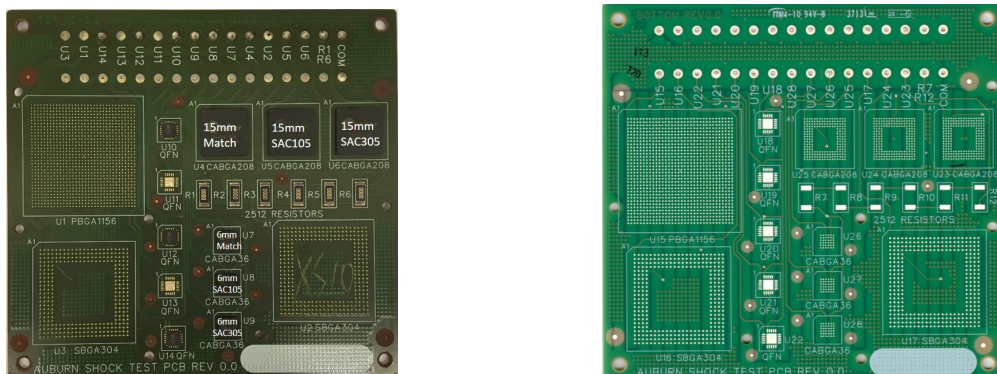
Materials and Methods

4.1 Test Vehicle Design and Assembly

4.1.1 Test Vehicle

The PCB of the test vehicle is made of four layers of FR4-06 glass-epoxy substrate with glass transition temperature of 170°C and dimensions of 4.0 x 5.0 x 0.062 inches. NSMD pads were used for the test vehicle. Figure 4.1a shows the front of the test board and Figure 4.1b shows the backside. As shown in the figures, both the front and back sides have component footprints for one PBGA1156, two SBGA304, three CABGA208, three CABGA36, five QFN and a bank of six 2512SMRs in series. Three different surface finishes, namely ENIG, ImAg and OSP were used. The surface finish thicknesses were measured using Rutherford backscattering spectroscopy (RBS). Figure 4.2 shows the measurements.

The RBS results showed relatively sharp spectra for the surface finishes even though it was less sharp for Au and Ni RBS peaks. The lower sharpness of RBS peaks could be an



(a) Frontside

(b) Backside

Figure 4.1: Testboard.

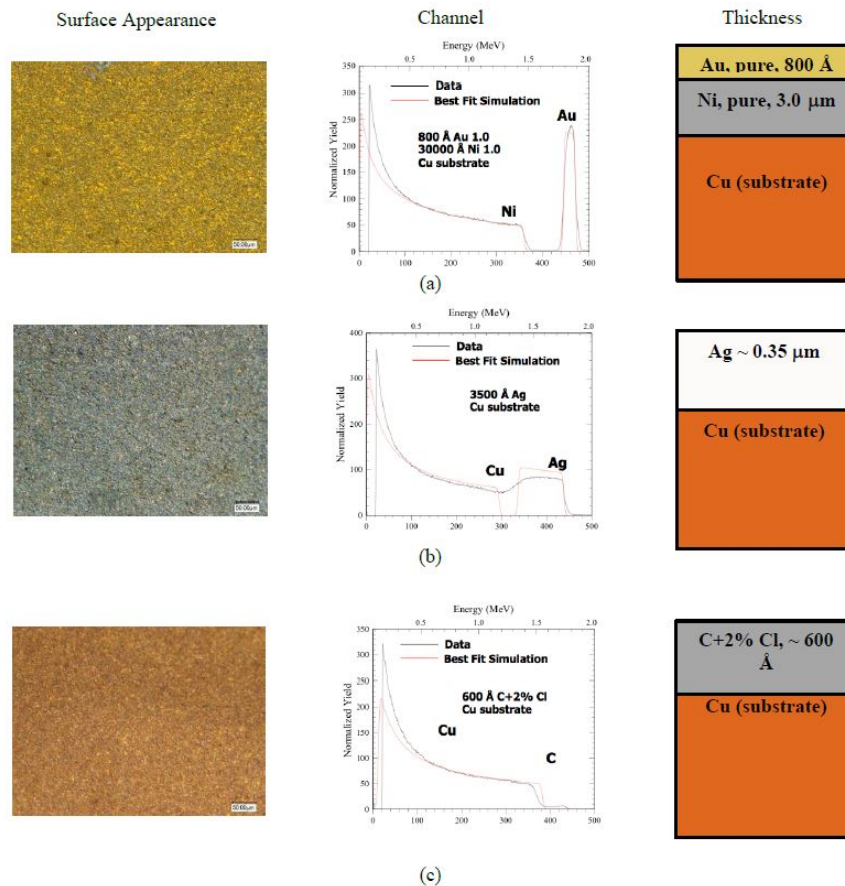


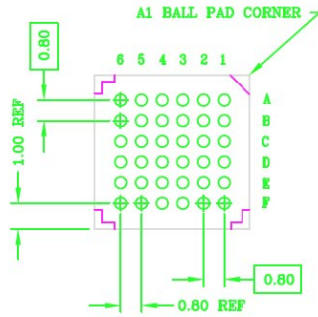
Figure 4.2: RBS for surface finishes: (a) ENIG, (b) ImAg, and (c) OSP

indication of interfacial roughness and/or slight inter diffusion between layers. For the ENIG finish, the Cu pad is coated with $3\mu\text{m}$ of pure Ni and 800\AA of pure Au. In the case of ImAg, the copper was coated with $0.35\mu\text{m}$ of Ag. OSP finish had the least thickness with 600\AA of organic material.

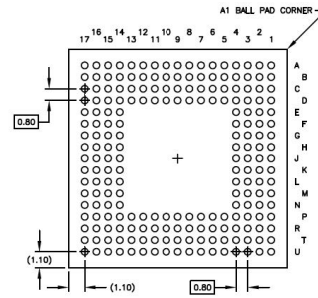
4.1.2 Test Components

The front side of the board was populated with components including BGAs, QFNs and SMRs. The PBGAs were mounted on the PCB using solder joints. Popular solder pastes, namely, SAC105 and SAC305 along with match (solder sphere is matched with solder paste) spheres were used to form the joint.

Two types of BGAs, CABGA208 and CABGA36 with package dimensions of $15\text{mm} \times 15\text{mm}$ and $6\text{mm} \times 6\text{mm}$, respectively, and pitch size of 0.8mm were included in the study. The MLF QFN packages had dimensions of $5\text{mm} \times 5\text{mm}$. 2512SMRs were also included in



(a) 6mm full array.



(b) 15mm perimeter array.

Figure 4.3: Schematic of BGA packages.

Package Type	Package Size (mm)	Pitch Size (mm)	Die Size (mm)	Ball Diameter (mm)	I/O Count	Ball Arrangement	Solder Sphere
BGA	15x15	0.8	12x12	0.46	208	Perimeter	SAC105/SAC305/Match
BGN	6x6	0.8	NA	0.46	36	Full Array	SAC105/SAC305/Match
QFN	5x5	0.65	4.5x4.15	NA	20	NA	Paste Only
2512SMR	2.5x1.2	NA	NA	NA	NA	NA	Paste Only

Table 4.1: Package specifications.

the study due to their large body size, high power dissipation and poor solder joint reliability. The QFNs and SMRs had terminations of 100% Sn. All components are daisy chained to ensure that all solder joints are included in the circuit and to allow continuous sampling of component resistance to detect interconnection failure. The specifications of different packages are tabulated in Table 4.1. The schematics of the bottoms of both BGA packages are shown in Figure 4.3a and Figure 4.3b.

4.1.3 Solder Alloys

In study, fourteen lead-free solder alloys were included. The BGA components were pre-balled with SAC105, SAC305 and match spheres before the components were mounted on the copper pads with stencil printed solder paste on the PCB. The solder paste constituted about 16% of the solder joint. Some BGAs did not have match spheres due to the unavailability of materials. The composition of the pastes used are tabulated in Table 4.2. The solder pastes include SAC pastes with dopants such as Bi, Sb, Ni, Mn, Nd and In.

Paste Name	Composition	Solder Sphere 15mm BGA	Solder Sphere 6mm BGA
Ind_1	98.47Sn-0.5Ag-1.0Cu-0.03Mn	SAC105/SAC305/Match	SAC105/SAC305/Match
A_Inn	90.95Sn-3.80Ag-0.70Cu-0.15Ni-1.40Sb-3.00Bi	SAC105/SAC305/Match	SAC105/SAC305/Match
Ind_2	SAC+Sb	SAC105/SAC305/	SAC105
Sj_94	Sn-3.4Ag-0.7Cu-3.2Bi-3.0Sb-Ni-Co	SAC105/SAC305/Match	SAC105/SAC305/Match
Ap_Mx	Sn-3.8Ag-0.8Cu-Bi-X	SAC105/SAC305/Match	SAC105/SAC305/Match
Ac_Cyx	92.77Sn-3.41Ag-0.52Cu-3.3Bi	SAC105/SAC305/Match	SAC105/SAC305/Match
Ac_Ely	96.62Sn-0.92Cu-2.4Bi	SAC105/SAC305/Match	SAC105/SAC305/Match
Hs_Inn	Sn-3.5Ag-0.7Cu-0.125Ni-1.5Sb-3Bi	SAC105/SAC305	SAC105
Hs_HT	Sn-2.5Ag-0.5Cu-2In-0.03Nd	SAC105/SAC305/Match	SAC105/SAC305/Match
Sj_58	Sn-3.0Ag-3Bi-0.8Cu-Ni	SAC105/SAC305/Match	SAC105/SAC305/Match
Hk_K	90.98Sn-3.8Ag-0.7Cu-0.02Ni-1.5Sb-3Bi	SAC105/SAC305	SAC105
Hk.L	90.98Sn-3.8Ag-0.7Cu-0.02Ni-1.5Sb-3Bi	SAC105/SAC305	SAC105

Table 4.2: Solder paste composition.

4.1.4 SMT Assembly

The test boards were assembled at Electronics Packaging Lab, University of Alabama, Huntsville. In order to remove the moisture that could damage the assembly, a 12-hour ‘bake out’ process was performed in the oven at 150°C. An E-FAB Electroform stencil with thickness of 6 mils was used for stencil printing. MPM UP2000 HiE machine was used for solder paste printing. Once the paste is printed on the PCB substrate, the assembly is visually inspected and verified by a 3D inspection process to check the area and volume of the paste deposit. The Universal GSM-1 pick and place machine with tray feeder is used to pick and place all components. The machine works based on a pre-stored algorithm to accurately pick and place components on the PCB. The assembly is inspected again to ensure that there is no skewed package placement. Figure 4.4 shows the SMT assembly line at UAH, Alabama. After the components are placed, the assembly is reflowed in a 13-zone Rehm V7 convection reflow oven with a conveyor speed of 26 inch/min, operating in a nitrogen environment. The reflow thermal profile is selected such that the solder joints have the best wetting with least board damage. Figure 4.5 and Figure 4.6 show the reflow oven and thermal profile used. Generally, there are four stages for the reflow profile. The pre-heat stage lasts for about 80 seconds, where the temperature is raised from 35°C to 155°C after which the assembly stays in soak stage (155°C to 175°C) for around 75 seconds. The peak temperature is around 245°C and the total time above 217°C (melting point for SAC alloys) is about 70 seconds. The maximum ramp rate is about 3°C per second.



Figure 4.4: Assembly line at UAH.



Figure 4.5: Reflow oven.

After the reflow, the assembly is allowed to cool. The assembly is later inspected by transmission X-ray tomography to ensure the quality of solder joints. Common defects such as insufficient solder, solder bridging, voids, black pad and head-in-pillow could be detected with this technology. In case of defects, the board is reworked.

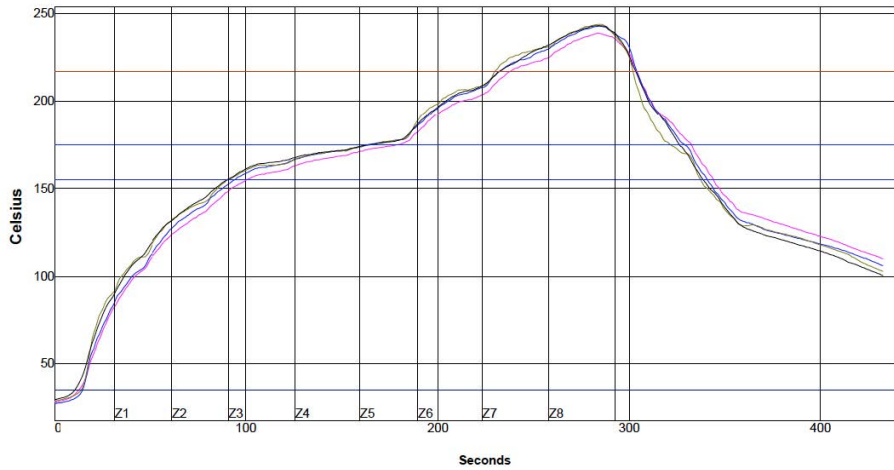


Figure 4.6: Reflow profile.

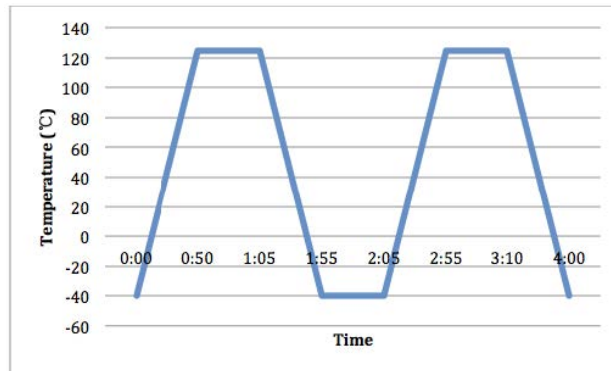


Figure 4.7: Thermal cycling profile.

4.2 Thermal Test

4.2.1 Isothermal Aging and Thermal Cycling

After the assembly the boards were isothermally aged at 125°C for a period of 12 months in a 16ft³ Thermotron chamber. After aging, all boards were subjected to thermal cycling with temperature range of -40°C to +125°C with 15 minutes dwell at +125°C and 10 minutes dwell at -40°C. The profile had a ramp time of 50 minutes, which would be at a rate of about 3.3°C per minute. The thermal profile was based on modified standard JEDEC JESD 22-A104-B. Figure 4.7 shows the thermal cycling profile for the test. Component matrix for larger aged BGAs are tabulated in Table 4.3 and aged SMRs are tabulated in Table 4.4, respectively. In the case of resistors, each one in the matrix indicates a bank of six resistors connected in series.

Finish	OSP			ImAg			ENIG		
	SAC105	SAC305	Match	SAC105	SAC305	Match	SAC105	SAC305	Match
Ind_1	5	5	5	5	5	5	5	5	5
A_Inn	5	5	5	5	5	5	5	5	5
Ind_2	5	5	0	5	5	0	5	5	0
Sj_94	5	5	5	5	5	5	5	5	5
Ap_Mx	5	5	5	5	5	5	5	5	5
Ac_Cyx	5	5	5	5	5	5	5	5	5
Ac_Ely	5	5	5	5	5	5	5	5	5
Hs_Inn	5	5	0	5	5	0	5	5	0
Hs_HT	5	5	5	5	5	5	5	5	5
Sj_58	5	5	5	5	5	5	5	5	5
Hk_K	5	5	0	5	5	5	5	5	0
Hk_L	5	5	0	5	5	0	5	5	0

Table 4.3: Component matrix for CABGA208 in aged condition.

Finish	OSP	ImAg	ENIG
Ind_1	5	5	5
A_Inn	5	5	5
Ind_2	5	5	5
Sj_94	5	5	5
Ap_Mx	5	5	5
Ac_Cyx	5	5	5
Ac_Ely	5	5	5
Hs_Inn	5	5	5
Hs_HT	5	5	5
Sj_58	5	5	5
Hk_K	5	5	5
Hk_L	5	5	5

Table 4.4: Component matrix for SMR2512 in aged condition.

Matrix for small BGAs (CABGA36) for aged condition are shown in Table 4.5 and QFNs are tabulated in Table 4.6, respectively.

4.2.2 Data Acquisition System

Test vehicles were arranged in palettes as shown in Figure 4.8. All components were wired to the data acquisition system developed by Dr. Thomas Sanders, Auburn University to measure the component resistance continuously. The system consists of Keithley 2001 digital multi-meter and Keithley scanning system interfaced through NI LabView software, as shown in Figure 4.9.

Finish	OSP			ImAg			ENIG		
Component	CABGA36			CABGA36			CABGA36		
Sphere	SAC105	SAC305	Match	SAC105	SAC305	Match	SAC105	SAC305	Match
Ind_1	5	5	5	5	5	5	5	5	5
A_Inn	5	5	5	5	5	5	5	5	5
Ind_2	5	0	0	5	0	0	5	0	0
Sj_94	5	5	5	5	5	5	5	5	5
Ap_Mx	5	5	5	5	5	5	5	5	5
Ac_Cyx	5	5	5	5	5	5	5	5	5
Ac_Ely	5	5	5	5	5	5	5	5	5
Hs_Inn	5	0	0	5	0	0	5	0	0
Hs_HT	5	5	5	5	5	5	5	5	5
Sj_58	5	5	5	5	5	5	5	5	5
Hk_K	5	0	0	5	0	0	5	0	0
Hk_L	5	0	0	5	0	0	5	0	0

Table 4.5: Component matrix for CABGA36 in aged condition.

Finish	OSP	ImAg	ENIG
Ind_1	15	15	15
A_Inn	15	15	15
Ind_2	15	15	15
Sj_94	15	15	15
Ap_Mx	15	15	15
Ac_Cyx	15	15	15
Ac_Ely	15	15	15
Hs_Inn	15	15	15
Hs_HT	15	15	15
Sj_58	15	15	15
Hk_K	15	15	15
Hk_L	15	15	15

Table 4.6: Component matrix for QFN in aged condition.

Based on the IPC-9701 standard, the solder joint failure was defined as the increase in resistance of more than 1,000 ohms. In this study, the solder joint failure is defined as the occurrence of an increase in daisy chain resistance of 100 ohms from the baseline resistance for five consecutive measurements.

4.2.3 Failure Analysis

After the test, the failed samples are used for micro structure analysis. The failed sample is cut from the PCB using a saw from Allied High Tech Products, Inc., with diamond sectioning blade. The sample is then cleaned and the face of the sample to be analyzed is selected using an

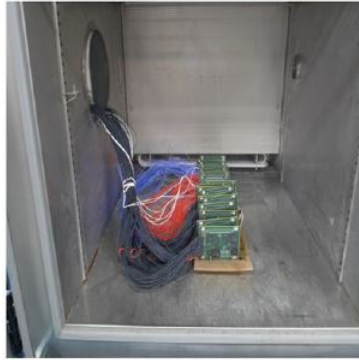


Figure 4.8: Test boards in thermal cycling chamber.

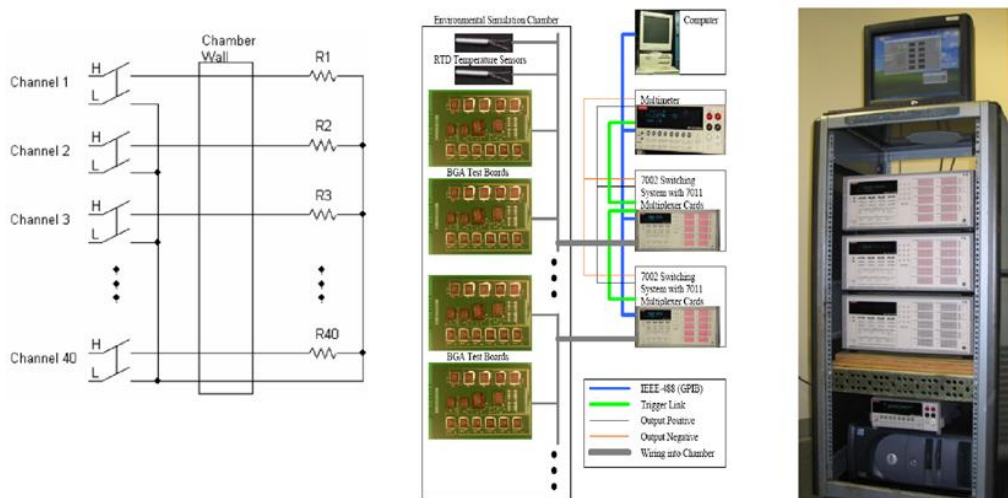


Figure 4.9: Schematic design of data acquisition system.

optical microscope. Then the component is mounted in a epoxy system (resin and hardener). For preparing the epoxy, the ratio of hardener to resin was 1:6. A unique label was prepared for each sample and a sample holder clip from Buehler was used to mount the sample upright. The epoxy was left in the mold for 20-24 hours for curing. Once the sample is cured, it is separated from the mold for preparing for the analysis. For grinding and polishing, semi-automated polishing machine from Pace Technologies (FEMTO-1000 with NANO-1000T polishing head) was used with silicon carbide grit papers. The automated polishing machine is shown in Figure 4.10. Papers of 120, 400, 600, 800, 1000 and 1200 grit were used sequentially. The sample was rotated 90° after each grit paper so that the cuts made by one paper are removed by the succeeding finer grit paper.



Figure 4.10: Semi-automated polishing machine.

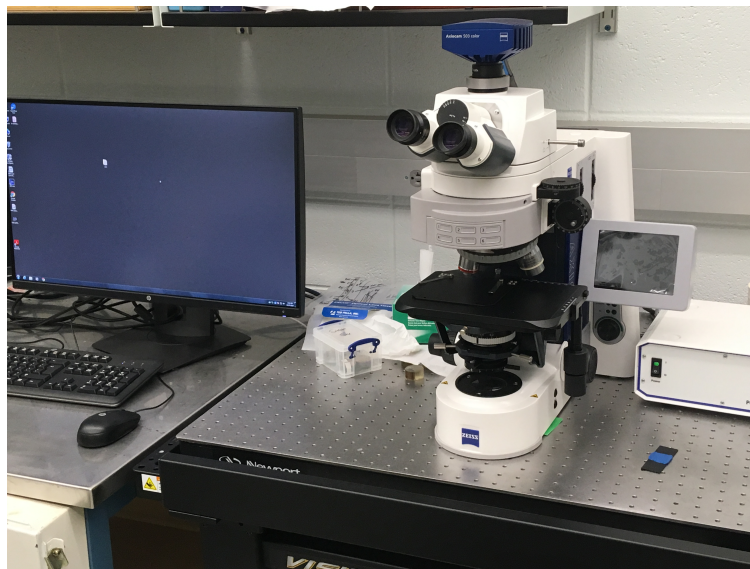


Figure 4.11: ZEISS Axio Imager.M2m optical microscope.

After grinding, the sample is polished using $3\mu\text{m}$, $1\mu\text{m}$ and $0.05\mu\text{m}$ viscous alumina polish from Pace Technologies and final stage of polishing is done using $0.02\mu\text{m}$ colloidal silica polishing suspension from Buehler. Each polishing stage lasts for 15 minutes to 30 minutes depending on the removal of scratches from previous stages. Once the sample is prepared, ZEISS Axio Imager.M2m optical microscope with a Axiocam 503 color microscope camera and ZEN-Core software was used to analyze the sample. Polarized images were also obtained to check for recrystallization. Once the desired image is captured, the software is used for further image analysis. The microscope used is shown in Figure 4.11.



Figure 4.12: Carbon coating system.



Figure 4.13: Hitachi S-2460N SEM.

For further analysis, Hitachi S-2460N Scanning Electron Microscope is used. In order to understand the material composition, EDX analysis is done. Prior to the SEM analysis, the samples are carbon coated in order to inhibit charging in non-conductive samples. DV-401 Carbon Coating System is used for coating carbon. Carbon tape is also used in order to ensure proper grounding of the sample. Carbon yarn, which is used as a source of carbon is kept about 48mm from the surface of the sample to ensure optimum coat thickness. Figure 4.12 and Figure 4.13 show the carbon coater and the SEM, respectively.

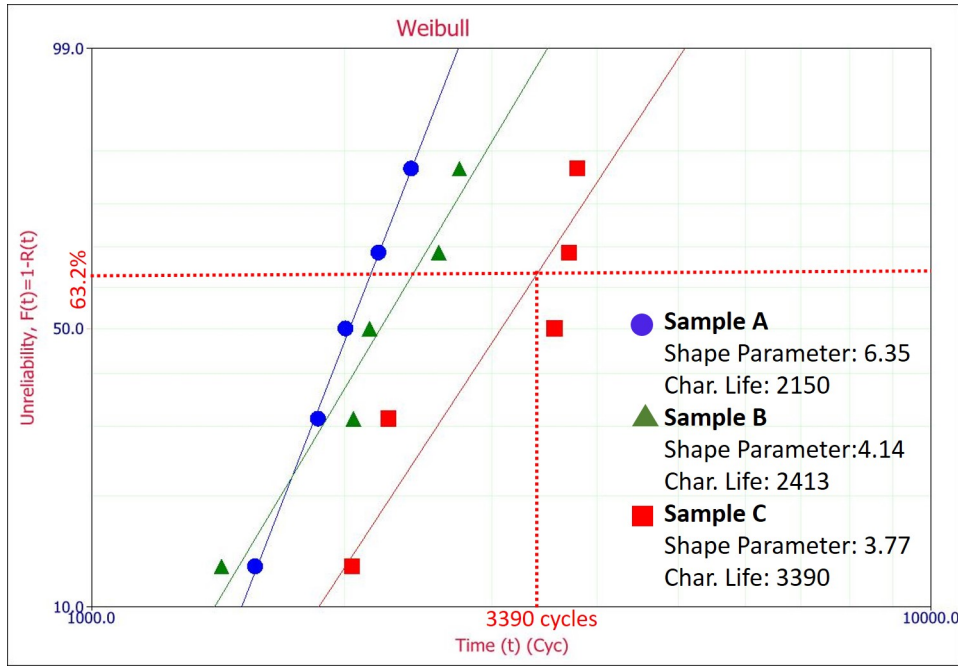


Figure 4.14: Weibull analysis for samples A, B and C.

4.3 Data Analysis

4.3.1 Two parameter Weibull plot

The data regarding the number of cycles each component survived is obtained from the data acquisition system. Weibull analysis is done in order to quantify the performance of each combination of component - solder paste - solder sphere - surface finish. In the Weibull plot, the probability of failure is the ordinate and time (cycles) is the abscissa. The probability of failure $F(t)$ of a product at time 't' is defined in equation 1.5, that depends on scale parameter (θ) and shape parameter (β). Two parameter (β, η) Weibull analysis is used in this study. The shape parameter β determines the slope of the plot and η is the characteristic life, which could be defined as time (cycles) at which 63.2% of samples failed. B10 life, the time at which 10% of the population is expected to fail, is also calculated for comparison of early failures in each combination. Figure 4.14 shows the Weibull analysis of three samples A, B and C. Right censoring is also used in cases where the samples did not fail at the end of the test.

In Figure 4.14, the characteristic lives of three samples are compared. In the case of each sample, there are five repetitions. Sample C has the highest life followed by Samples B and A. The more the plot is on the right, better is its life. Bar charts are also used from time to

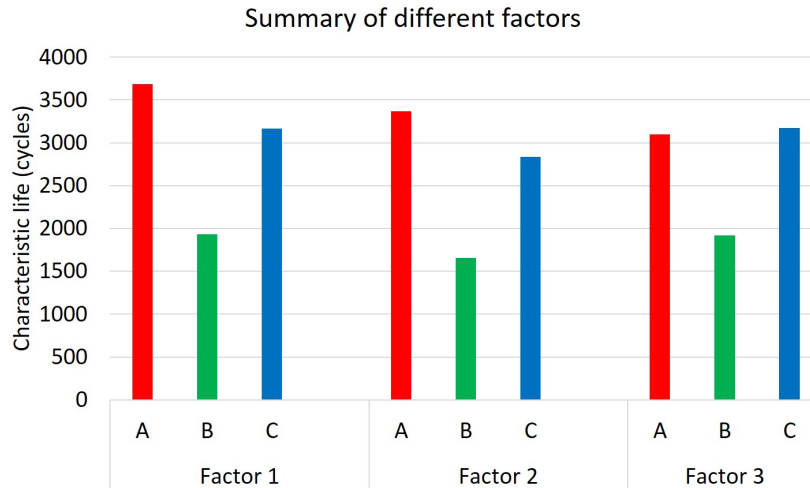


Figure 4.15: Comparison of factors 1, 2 and 3.

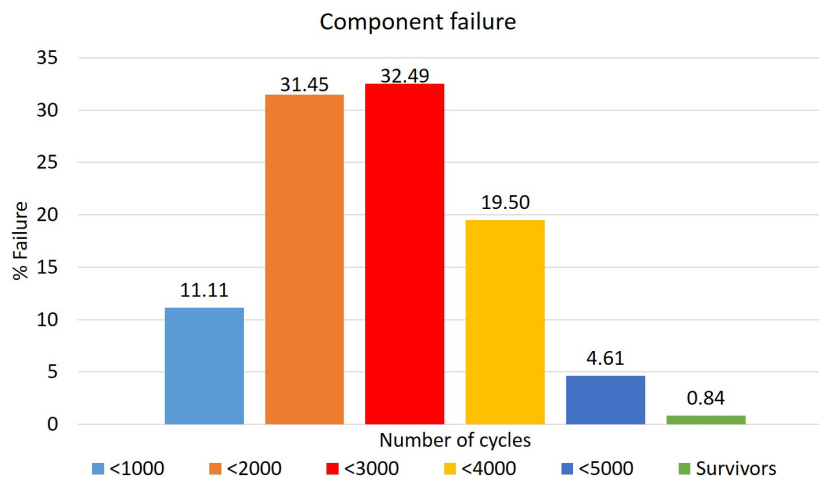


Figure 4.16: Percentage failure analysis.

time for comparison between different levels and different factors as shown in Figure 4.15. Percentage failure analysis is done to determine the time around which most of the failures occurred. Example of % failure plot is shown in Figure 4.16. As per the figure, it could be seen that most of the failures occur around 2000-3000 cycles. This conclusion could be valuable for military and automotive industry, but not for the consumer electronics industry.

4.3.2 ANOVA analysis

From the characteristic life obtained from the Weibull analysis, ANOVA analysis is done in order to determine the most and least influential factors. In the study, there are different factors such as component type, solder sphere, solder paste, surface finish, aging and several others.

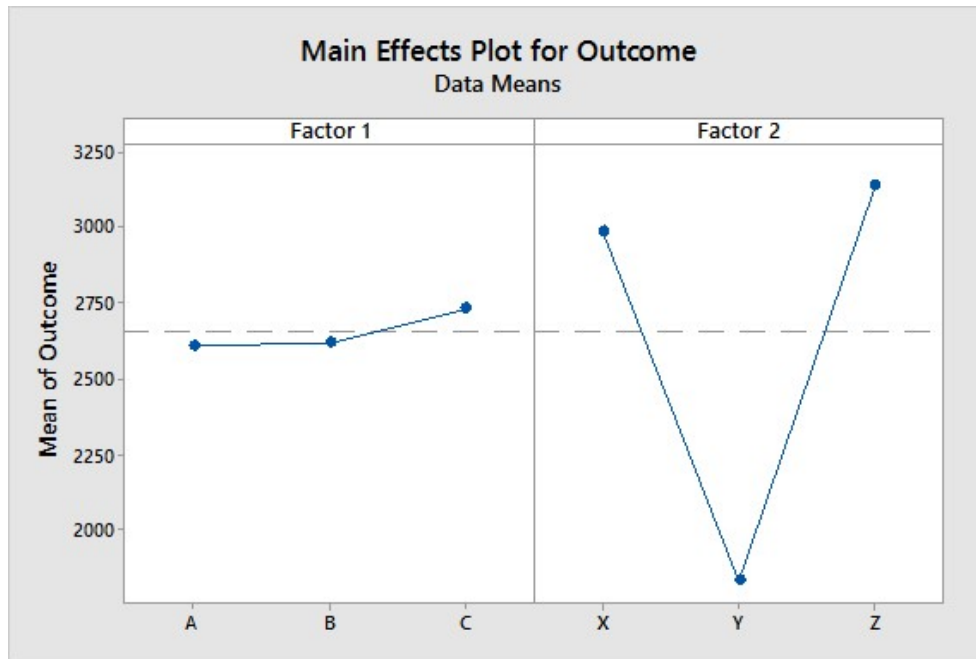


Figure 4.17: Main effect plot for two factors, each with three levels.

In the main effect plot, the influence of each factor on the outcome is considered separately and other factors are ignored. But in reality, the interaction between different factors could also be responsible for the outcome, which would be determined from the interaction plots. As shown in the main effect plot of Figure 4.17, it could be concluded that ‘factor 1’ does not have much influence on the outcome, even though C does better than A and B. But ‘factor 2’ has a significant effect on the outcome. Z and X have positive influences on the outcome, while Y has a negative influence. From the interaction plot of Figure 4.18, the combination that has positive or negative influence on the outcome could be determined. For example, a combination of A with Z influences the outcome positively while A with X has a negative effect on the outcome.

4.3.3 IMC Layer Analysis

The thickness of the IMC layer is measured for each combination to study the role of its thickness on the component reliability. ANOVA analysis is done to determine the factors responsible for the IMC layer growth. In order to measure the thickness of the IMC layer, the picture is captured using the ZEISS microscope as shown in Figure 4.19.

The area and the length of the layer is obtained using the image processing tools in ZEN core software by ZEISS. The thickness is calculated by dividing the area by the length, so that

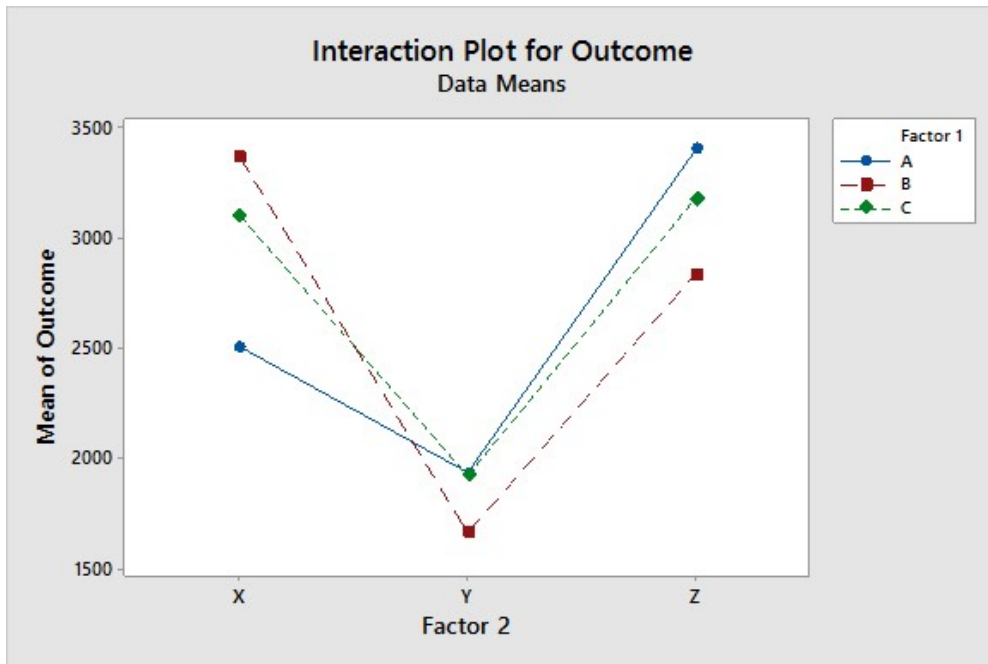


Figure 4.18: Interaction effect plot for two factors, each with three levels.

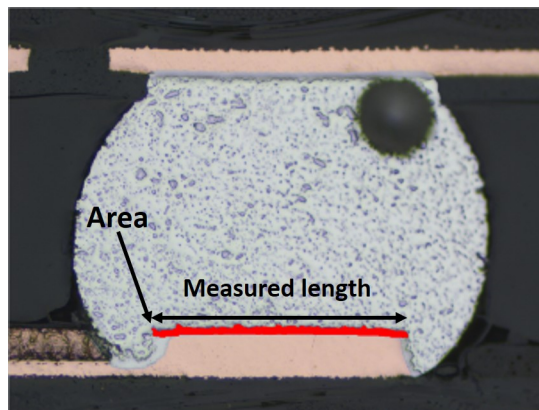


Figure 4.19: IMC layer thickness measurement.

the mean thickness is obtained. Measurements are taken for at least three different solder joints in a sample and their average is calculated for the IMC layer thickness.

Chapter 5

Effect of Surface Finish on Component Reliability

5.1 Introduction

As mentioned earlier, surface finishes are used to protect the copper pads prior to assembly. During assembly, the finish becomes a part of the solder joint and thereby has influence on the reliability of the component. Three of the popular surface finishes, namely ENIG, ImAg and OSP are included in this study. The surface finish plays an important role in determining the thickness of the IMC layer at the interface of solder and copper pads that affects the solder joint reliability. In this chapter the performances of three surface finishes are compared in regard to the characteristic life of the component. Two Bi based solder alloys are included in the study and compared with SAC305 alloy. The alloy composition with the labels used are shown in Table 5.1.

All the boards were isothermally aged at a temperature of 125°C for a period of twelve months. Temperature of 125°C was chosen so that the packages undergo effective aging. The boards were then subjected to thermal cycling with the temperature range from -40°C to +125°C for 5,000 cycles. The resistance of each component was measured using the monitoring system mentioned in Chapter 4. The test matrix used in the study is presented in Table 5.2.

Solder paste	Label	Composition
A_Inn	Innolot	Sn-3.80Ag-0.70Cu-0.15Ni-1.40Sb-3.00Bi
A_Mx	SAC-Bi	Sn-3.8Ag-0.8Cu-2.8Bi
SAC305	SAC305	Sn-3.0Ag-0.5Cu

Table 5.1: Solder alloys in the study.

Component	Solder paste/sphere	Surface Finish
CABGA208	Innolot	ENIG
		ImAg
		OSP
	SAC-Bi	ENIG
		ImAg
		OSP
	SAC 305	ENIG
		ImAg
		OSP

Table 5.2: Test matrix.

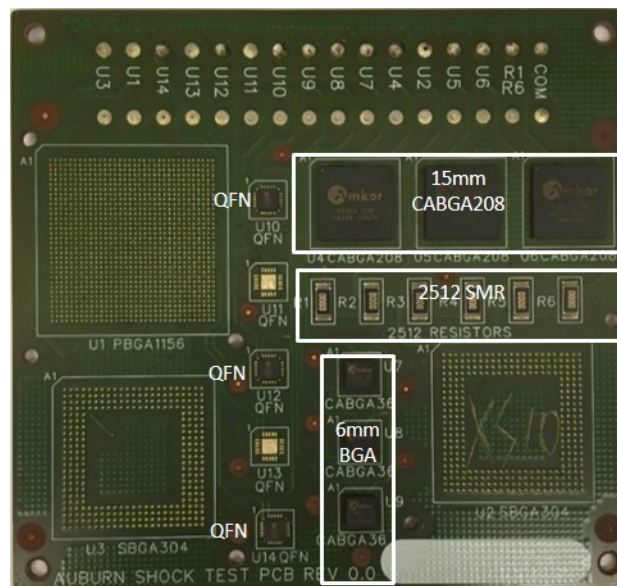


Figure 5.1: Test vehicle used.

5.2 Setup and Procedure

The test vehicle use for this study is the same as the one mentioned in the previous chapter, in Section 4.1.1 and is shown in Figure 5.1.

5.3 Results and Discussion

Once the test was over, the data were collected and analyzed. It was observed that only the large components had enough failures while there were very few failures among the small BGAs and SMRs. So the data presented in this study pertains to the CABGA208s. Two parameter Weibull analysis is used to quantify the performances of different solder alloy-surface finish

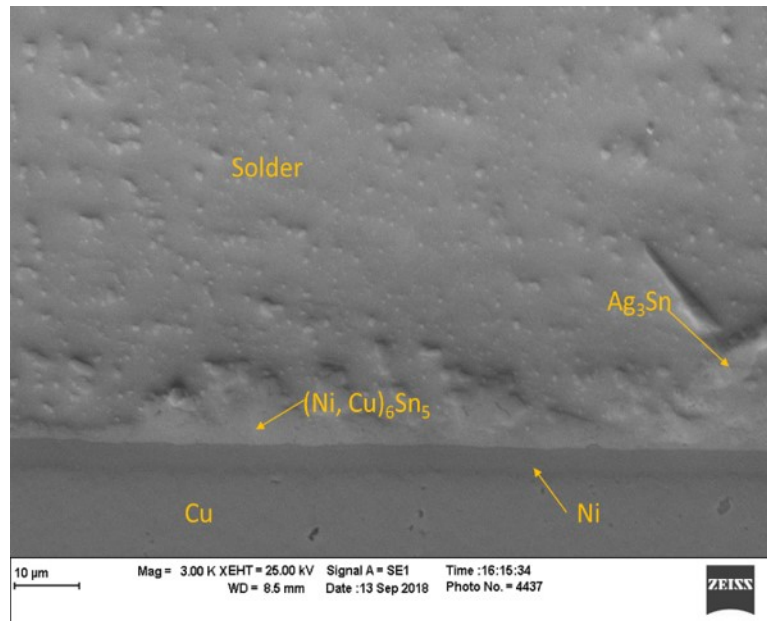


Figure 5.2: SEM image of SAC-Bi alloy with ENIG surface finish [39].

combinations. ANOVA analysis is also used to determine the most influential factors in the component reliability.

During the reflow process, an IMC layer is formed at the interface of bulk solder and the board. This layer is essential for the electrical and mechanical connection. Gradually, with time the IMC layer grows in thickness and negatively impacts the component reliability due to its brittle nature. Figure 5.2 shows the SEM image of SAC-Bi alloy with ENIG finish after assembly. ENIG finish has a Ni layer that blocks the diffusion of Cu from the pads. A thin layer of gold is used to protect Ni during its shelf life. During the reflow, gold is totally dissolved in the molten solder. Since the solid solubility of Au in Sn is negligible at room temperature, all the gold precipitates out as $(\text{Au},\text{Ni})\text{Sn}_4$ [84]. The IMC layer as shown in the figure consists of $(\text{Ni},\text{Cu})_6\text{Sn}_5$. In the case of ENIG finish, Cu in the IMC comes from the bulk solder and not from the Cu pads. The IMC layer is comparatively thin in the case of ENIG finish with respect to ImAg and OSP finish. Figure 5.3 shows the SEM image of ImAg surface finish with SAC-Bi alloy. IMC layer in the case of this finish is composed of Cu_6Sn_5 . Large precipitates of Ag_3Sn could be seen near the IMC layer due to increased Silver content from the ImAg finish.

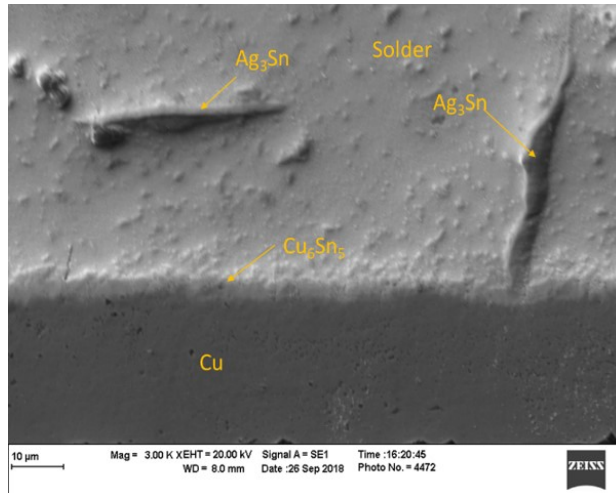


Figure 5.3: SEM image of SAC-Bi alloy with ImAg surface finish [39].

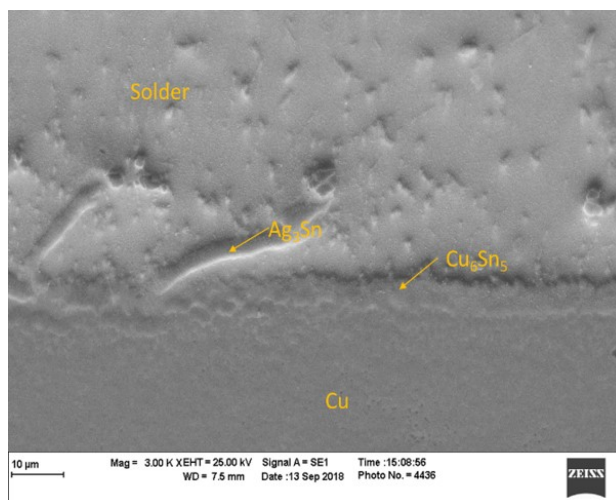


Figure 5.4: SEM image of SAC-Bi alloy with OSP surface finish [39].

SEM image of OSP finish with SAC-Bi is shown in Figure 5.4. The IMC layer was formed of Cu_6Sn_5 , similar to ImAg finish and a network of Ag_3Sn dispersion could be seen in the tin matrix.

Figure 5.5 shows Weibull analysis for different surface finishes in the case of Innolot solder alloy. As could be seen in the figure, ENIG surface finish performs the best with characteristic life of about 4,440 cycles followed by ImAg with 3,271 cycles. OSP has the least characteristic life of 2,348 cycles. It could also be seen that there are couple of early failures in the case of ImAg that pulls down its characteristic life. Figure 5.6 summarizes the characteristic life and B10 life for Innolot paste. In the case of characteristic life, drops of 26% and 47% could be observed for ImAg and OSP finishes, respectively, when compared with ENIG finish. B10 life

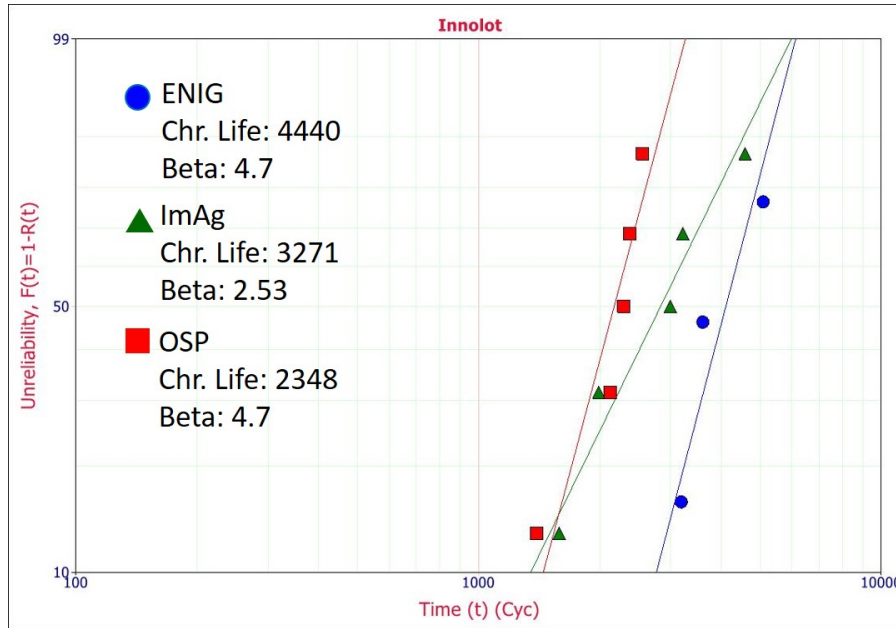


Figure 5.5: Weibull analysis of surface finishes for Innolot alloy.

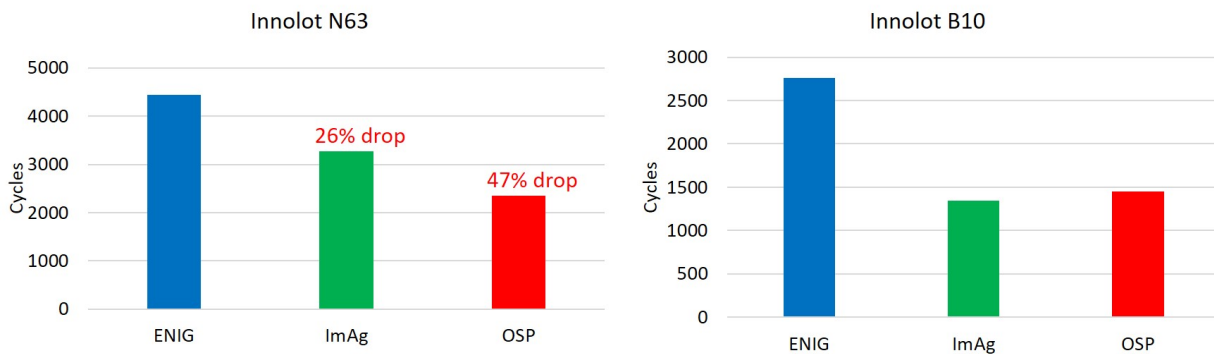


Figure 5.6: Summary of characteristic life and B10 life for Innolot alloy.

analysis is used to study the early failures. In this case, ImAg has the least B10 life unlike the trend in characteristic life, which is due to early failures.

Weibull analysis for SAC-Bi alloy is shown in Figure 5.7. The plots have a similar trend as in the case of Innolot, except that there are no early failures. ENIG has the highest characteristic life of 4529 cycles followed by ImAg and OSP with 3,028 and 2,846 cycles, respectively. The same data are summarized in Figure 5.8 and characteristic life shows a drop of about 35% when ENIG is not used. Since there are no early failures, B10 life follows the same trend as the characteristic life.

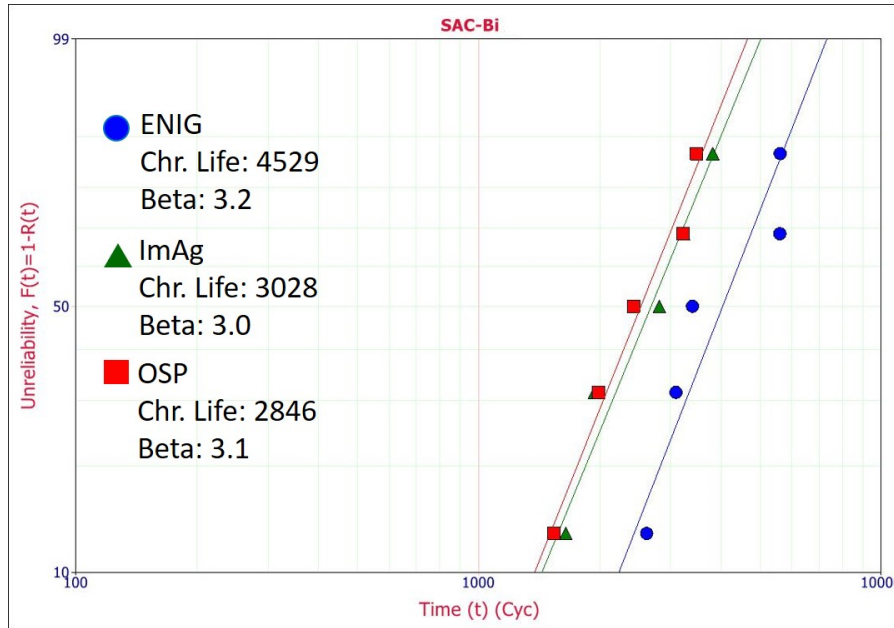


Figure 5.7: Weibull analysis of surface finishes for SAC-Bi alloy.

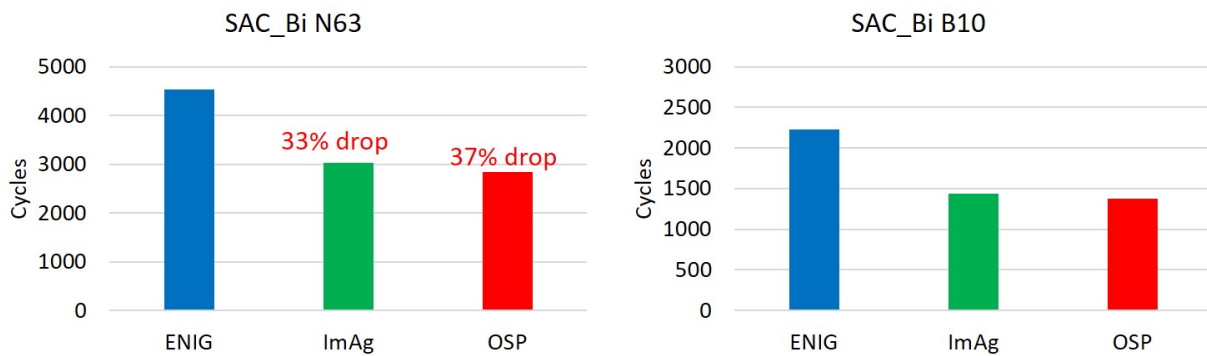


Figure 5.8: Summary of characteristic life and B10 life for SAC-Bi alloy.

Weibull analysis of SAC305 alloy is presented in Figure 5.9. Even in this case, trends similar to the other alloys are followed as ENIG leads the pack with 2,663 cycles and OSP has the least characteristic life of 1,183 cycles. Figure 5.10 shows the summary of the fatigue life. Characteristic life drops by about 30% when ImAg is used and more than 50% when OSP is used. B10 life follows the same trend as in the case of characteristic life since there are no early failures.

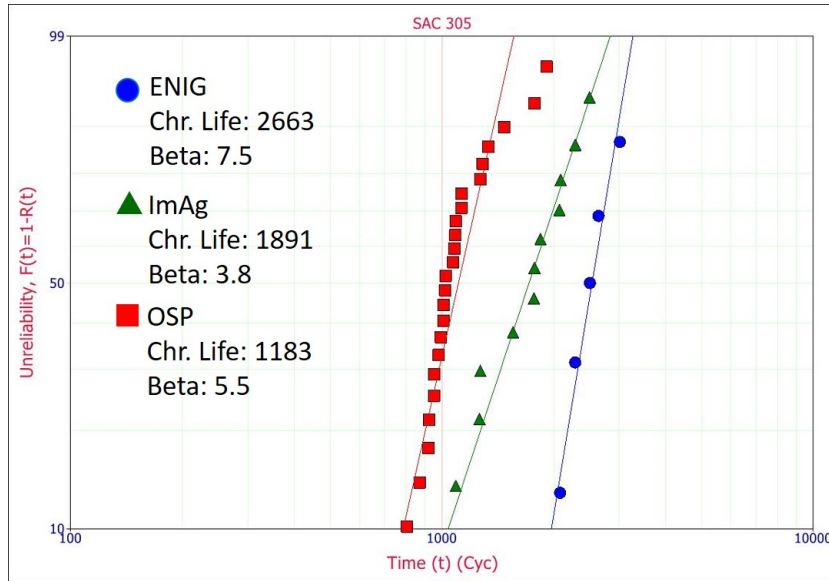


Figure 5.9: Weibull analysis of surface finishes for SAC305 alloy.

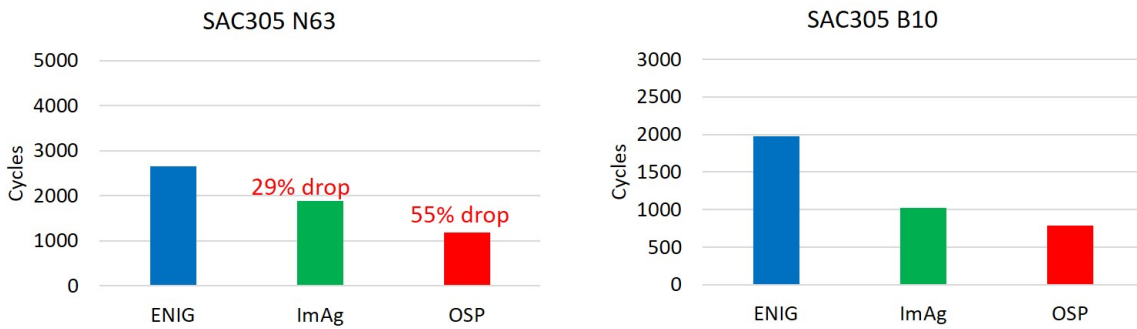


Figure 5.10: Summary of characteristic life and B10 life for SAC305 alloy.

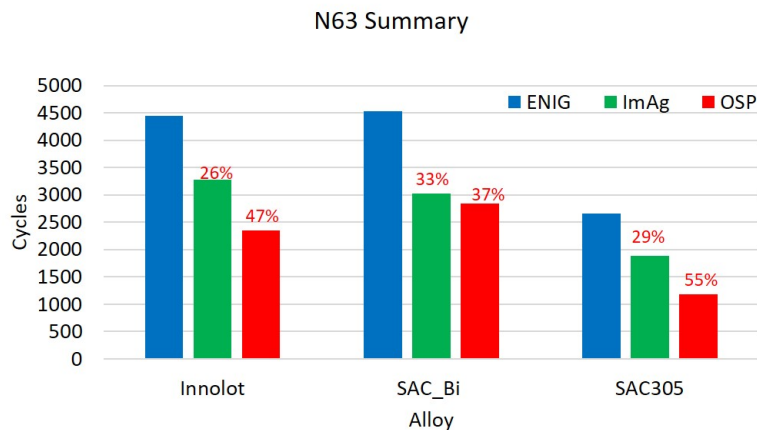


Figure 5.11: Summary of characteristic life for all alloys.

Figure 5.11 summarizes the characteristic life for all alloys. From the bar charts, it could be concluded that surface finish has an effect on the component reliability as ENIG performs

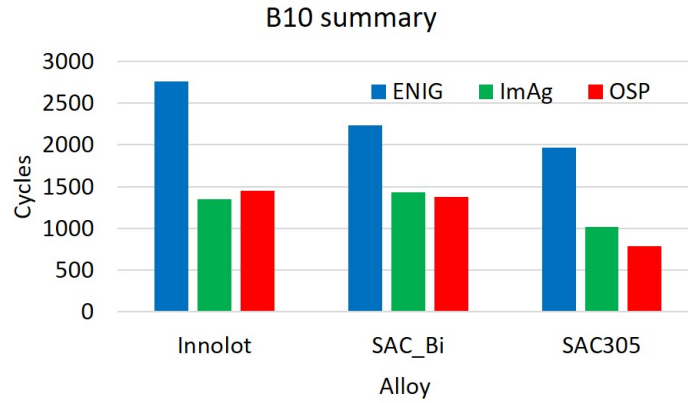


Figure 5.12: Summary of B10 life for all alloys.

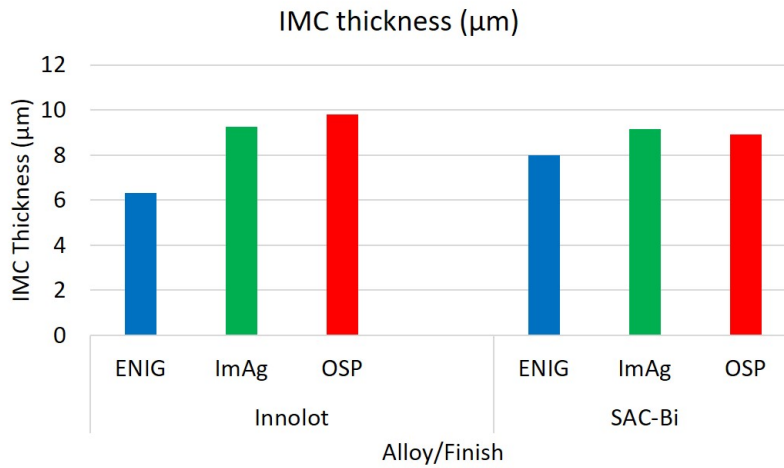
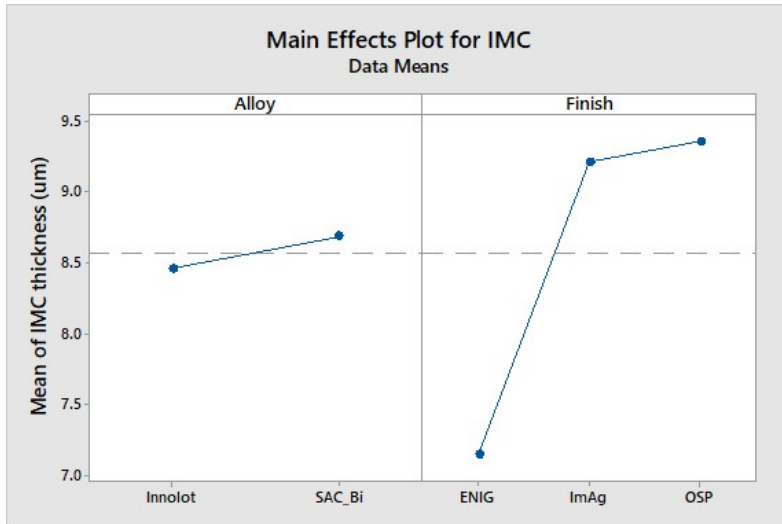


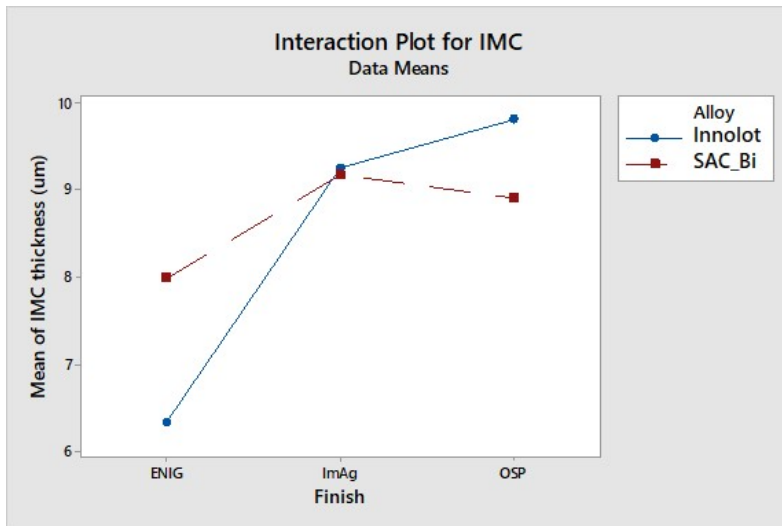
Figure 5.13: IMC layer thickness measurements.

the best, followed by ImAg and OSP. Even in the case of B10 life, ENIG performs better than others, as shown in Figure 5.12. It can also be noted that, among solder alloys SAC305 has the lowest reliability and that as more elements are micro-alloyed, the reliability increases. Figure 5.13 presents the IMC layer thickness measurements of Innolot and SAC-Bi solder joints for each surface finish. ENIG finish has the least IMC layer thickness. IMC thickness increases for ImAg and OSP finishes. The Ni layer in the case of ENIG finish, appears to have a significant impact on the growth of IMC layer at the interface.

Different factors influencing the growth of IMC layer are investigated in Figure 5.14a and Figure 5.14b. It could be seen that solder alloy or paste does not have a significant impact as the IMC layer thicknesses in both cases are in the same range. But, when it comes to the finish,



(a) Main effects plot.



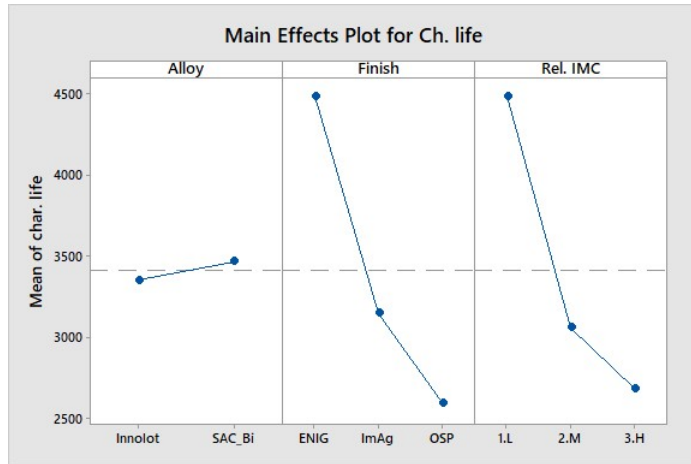
(b) Interaction plot.

Figure 5.14: ANOVA analysis for IMC growth.

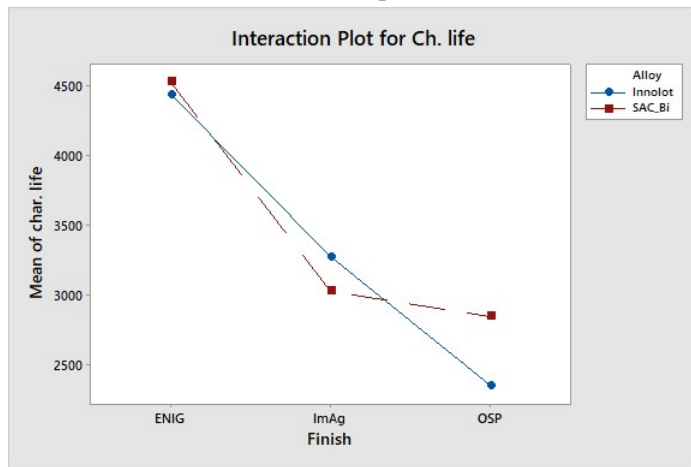
it could be seen that ENIG has the least IMC layer thickness and that ImAg and OSP have IMC layers of average thickness of more than $9\mu\text{m}$. This could be attributed to the Ni layer in the case of ENIG finish. From the interaction plot, it appears that SAC-Bi performs better with OSP than Innolot in having the least IMC thickness and this trend is reversed in the case of ENIG.

Figure 5.15a, Figure 5.15b and Figure 5.15c show ANOVA analysis of effects of different factors such as solder alloys, finish and relative IMC thickness on the characteristic life.

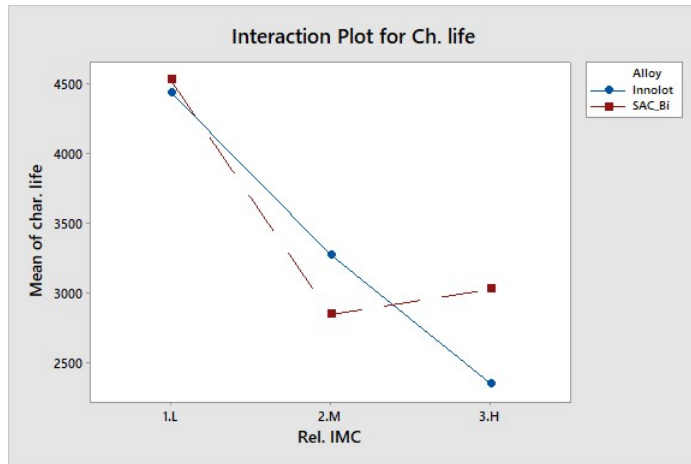
From the main effect plot, it could be seen that micro-alloying Bi and other elements have an effect on the reliability and that ENIG has a significant positive impact on the component



(a) Main effects plot.



(b) Interaction plot between alloy and finish.



(c) Interaction plot between alloy and rel. IMC layer thickness.

Figure 5.15: ANOVA analysis for characteristic life.

reliability followed by ImAg. It could also be seen from Figure 5.15a that the least thick IMC could be correlated with highest characteristic life. In this analysis, the categorization of the

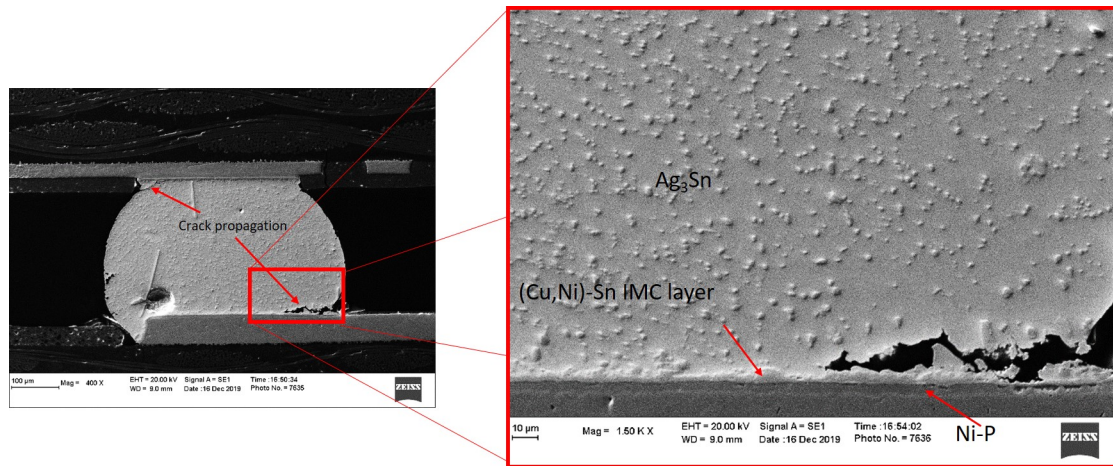


Figure 5.16: SEM image of SAC-Bi solder joint with ENIG finish.

relative IMC thickness was done locally in each alloy. For each alloy, the least thick IMC layer was categorized as low (L) and the thickest layer was categorized as high (H). From the interaction plot between alloy and finish, it could be seen that Innolot and SAC-Bi perform very closely in the case of ENIG finish and Innolot performs slightly better in the case of ImAg. When it comes to OSP, SAC-Bi has better life than Innolot. When the effect of relative IMC thickness and solder alloy is investigated as in Figure 5.15c, the alloys perform closely in the case of least thick IMC layer. For medium thick layer, Innolot is slightly better than SAC-Bi. But in the case of the thickest IMC layer, SAC-Bi performs better than Innolot. IMC layer is brittle in nature. When the effect of Innolot that has Sb is combined with IMC layer, the solder joint might become more brittle as Sb makes the alloy more brittle [85].

Figure 5.16 shows the cross section of SAC-Bi solder joint with ENIG surface finish. As can be observed, ENIG finish has a Ni layer that prevents Cu from the pads from diffusing into the bulk solder to form Cu_6Sn_5 precipitate. Finer, uniformly distributed Ag_3Sn precipitates were found in the bulk of the solder joint.

Figure 5.17 shows the cross section of SAC-Bi solder joint with ImAg finish. At reflow, the Ag from the finish dissolves in the bulk and forms Ag_3Sn precipitate due to which an increased density of Ag_3Sn precipitate is found near the Cu pads. In the case of OSP surface finish with SAC-Bi solder alloy, as shown in Figure 5.18, Cu from the pads diffuses into the bulk to form IMC layer at the pad-solder interface as well as Cu_6Sn_5 precipitates in the bulk solder.

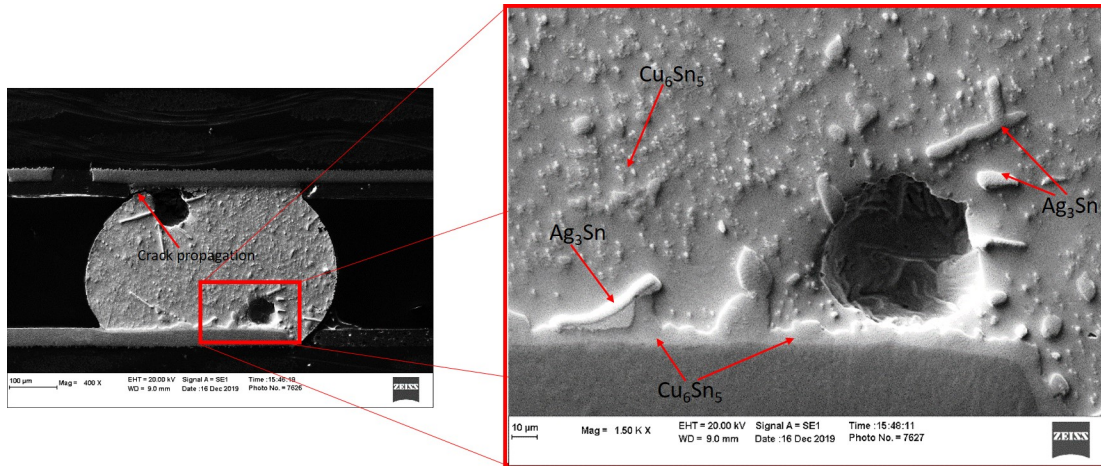


Figure 5.17: SEM image of SAC-Bi solder joint with ImAg finish.

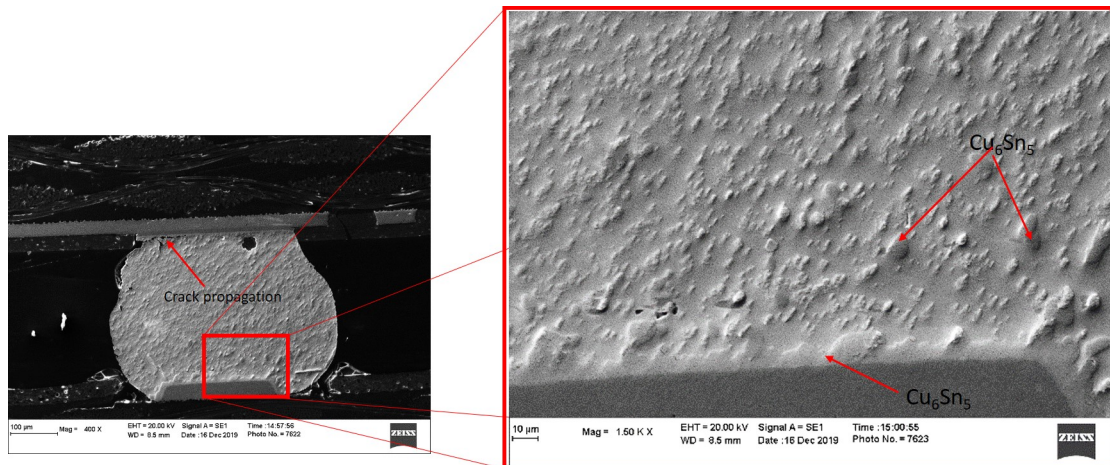
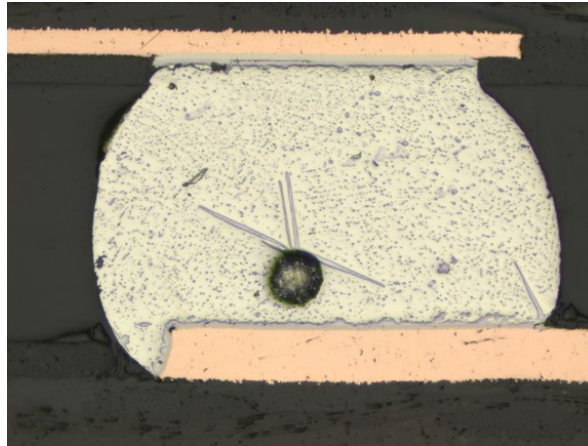


Figure 5.18: SEM image of SAC-Bi solder joint with OSP finish.

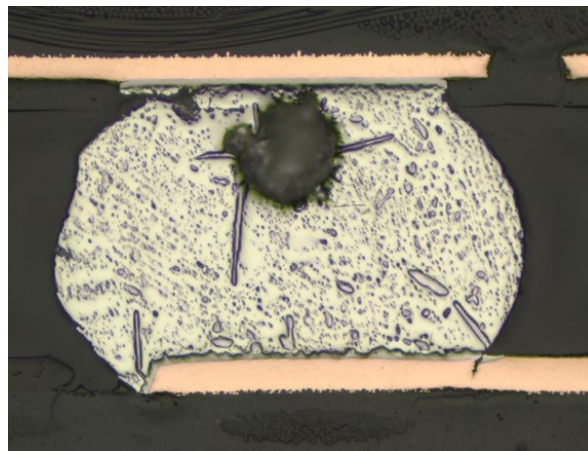
Figure 5.19a, Figure 5.19b and Figure 5.19c show darkfield images of solder joints with ENIG, ImAg and OSP finishes, respectively. It could be observed that the precipitate in the bulk is more uniformly distributed and finer in the case of ENIG. Ag_3Sn precipitates were much coarse in the case of ImAg and OSP finishes. This observation aligns with that in the work by Collins et al. [84]. Large number of needle shaped Ag_3Sn could be observed in the case of ImAg finish as well.

5.4 Conclusion

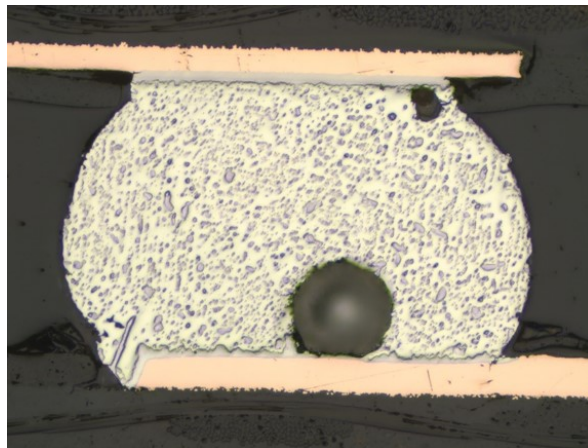
The effects of different surface finishes were studied with CABGA208 component and different solder pastes. The major conclusion was that there was a significant improvement in reliability when ENIG finish was used with different pastes included in the study. ENIG was followed



(a) ENIG finish



(b) ImAg finish



(c) OSP finish

Figure 5.19: Comparison of solder joints with different finishes and SAC-Bi alloy.

by ImAg, which was followed by OSP. When it comes to the different solder pastes, microalloyed alloys, namely Innolot and SAC-Bi performed better than SAC305 alloy. Even in the case of microstructure, ENIG had a significant impact. Microstructure with finer and uniformly distributed precipitates, as in the case of ENIG finish correlated with better reliability.

Chapter 6

Effect of Micro-Alloying New Elements on Thermal Cycling Reliability of Components

6.1 Introduction

As concluded in the previous chapter, solder microstructures with fine and uniformly distributed precipitates are crucial in having high-reliability joints. The features that influence the solder joint, such as solder paste, solder sphere, and surface finish, should promote such a microstructure. The solder joints exposed to thermal cycling undergo re-crystallization that aids the local growth of several new grains in areas of stress concentration. These new grains help in crack propagation and the crack propagates along the grain boundaries, ultimately resulting in failure. The situation becomes much worse in the case of aging. In this chapter, the effect of alloy composition is investigated under three surface finishes.

6.2 Setup and Procedure

The test vehicle used for this study is the same as the one mentioned in Section 4.1.1 and is shown in Figure 6.1. The test board consists of three large BGAs(CABGA208), three small BGAs(CABGA36) with daisy chain connection and a bank of six resistors (SMR2512) connected in series. The solder alloys included in the study are such that they provide some insight into the effects of micro-alloying new elements with the SAC alloy in order to improve the reliability. SAC305 is included for comparison of the performance. The alloy compositions and their labels are shown in Table 6.1.

All boards were isothermally aged at a temperature of 125°C for a period of twelve months. Temperature of 125°C was chosen so that the packages undergo effective aging. The boards

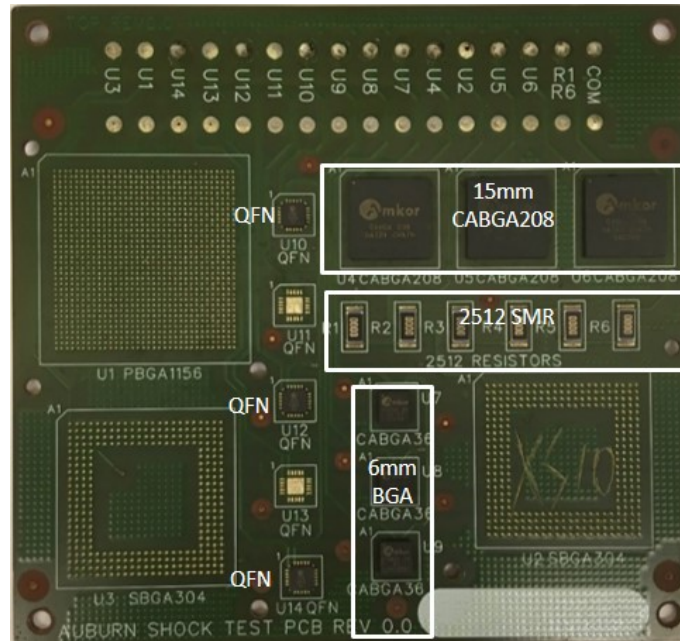


Figure 6.1: Test vehicle used.

Paste	Label	Composition
A_Inn	Innolot	90.95Sn-3.80Ag-0.70Cu-0.15Ni-1.40Sb-3.00Bi
Ac_Cyx	SAC-Bi	92.77Sn-3.41Ag-0.52Cu-3.3Bi
Hs_HT	SAC-In	Sn-2.5Ag-0.5Cu-2In-0.03Nd
Ind_1	SAC-Mn	98.47Sn-0.5Ag-1.0Cu-0.03Mn
SAC305	SAC305	Sn-3.0Ag-0.5Cu

Table 6.1: Solder alloys used in the study.

were then subjected to thermal cycling with the temperature range from -40°C to $+125^{\circ}\text{C}$ for 5,000 cycles. The resistance of each component was measured using the monitoring system mentioned in Chapter 4. The test matrix used in the study is presented in Table 6.2.

6.3 Results and Discussion

Figure 6.2 shows the image of a typical solder joint. There are several factors that contribute to the reliability of the solder joint. Some of the factors are solder sphere, solder paste, and surface finish. In this particular study, the effect of solder alloy (includes solder sphere and paste) is investigated under three surface finishes.

Component	Surface finish	Solder alloy
CABGA208	ENIG	Innolot
		SAC-Bi
		SAC-In
		SAC-Mn
		SAC305
	ImAg	Innolot
		SAC-Bi
		SAC-In
		SAC-Mn
		SAC305
	OSP	Innolot
		SAC-Bi
		SAC-In
		SAC-Mn
		SAC305

Table 6.2: Test matrix.

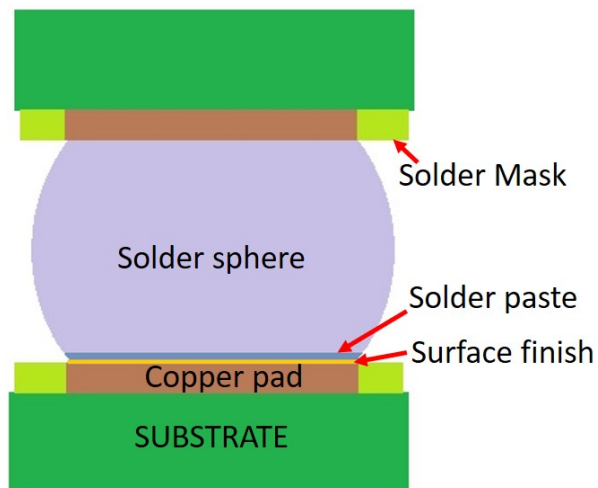
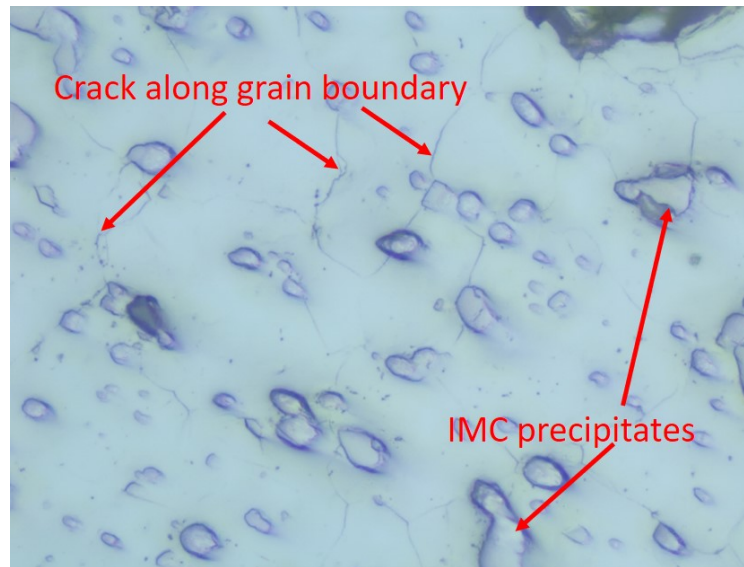
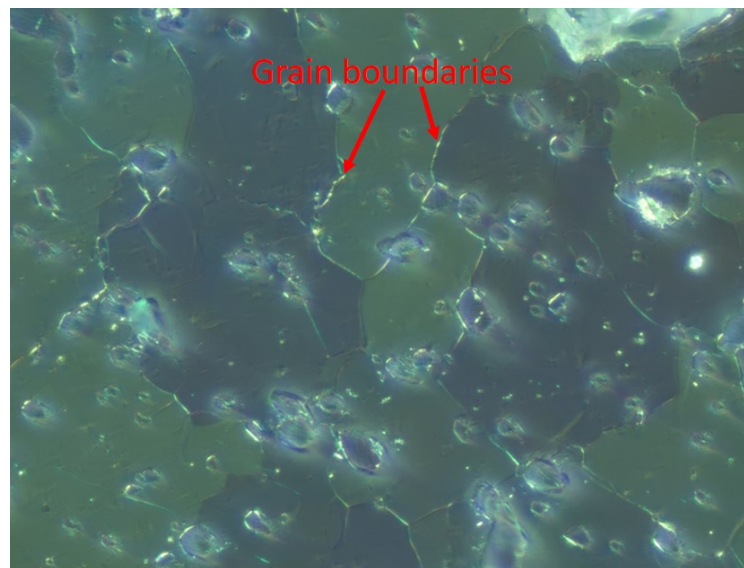


Figure 6.2: Typical solder joint.

Figures 6.3a and 6.3b show the dark field and polarized image of a typical solder alloy after thermal cycling. During thermal cycling, thermally induced inelastic strain is developed due to the thermal expansion mismatches between materials and a crack is initiated, which propagates where there is inelastic strain concentration. This is close to the interface between solder and the component [86–91].



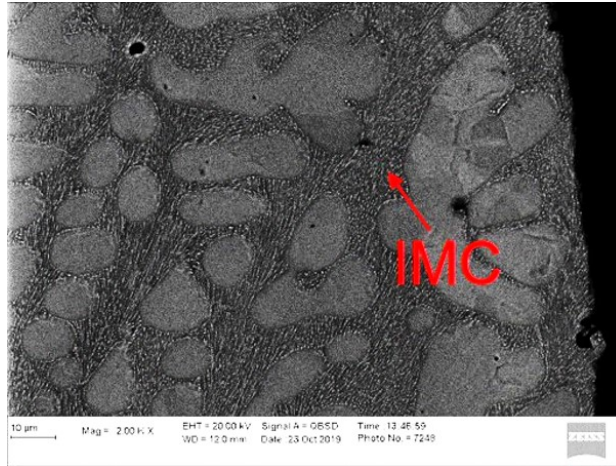
(a) Dark field image



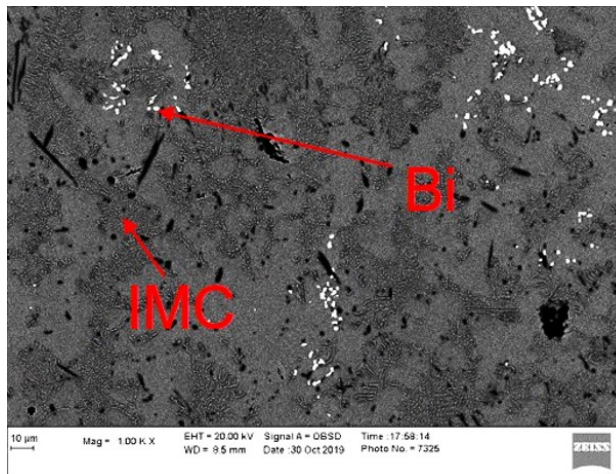
(b) Polarized image

Figure 6.3: Recrystallization after thermal cycling.

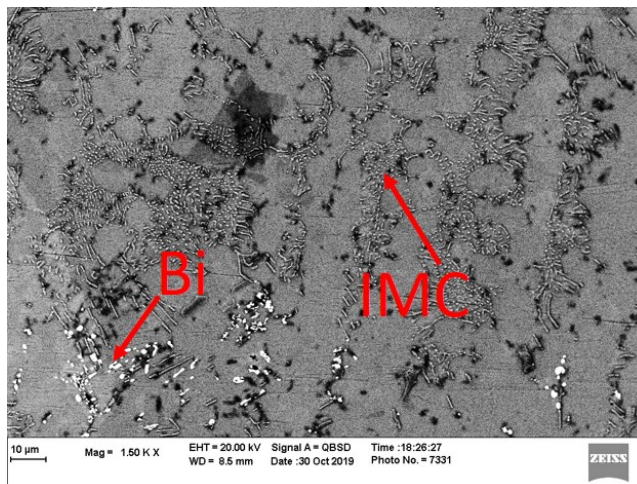
Figure 6.4a, Figure 6.4b and Figure 6.4c show the microstructure of the corresponding alloys after assembly. After assembly, the precipitates are fine and spread evenly. In the case of SAC305, the IMC precipitates form an interlaced network. The microstructure in the case of SAC-Bi and Innolot appear similar to IMC precipitates forming a network with Bi precipitates. These fine precipitates with Bi are effective in blocking the dislocation movements. The figure shows the microstructure of the alloys after months of aging. After aging the fine IMC precipitates coalesce and get coarsened. This microstructure is not as effective in blocking the dislocation movements.



(a) SAC305



(b) SAC-Bi



(c) Innolot

Figure 6.4: Comparison of microstructure of different solder alloy.

Figure 6.5 shows Weibull analysis for different solder alloys under study for ENIG surface finish and Figure 6.6 shows the summary of characteristic life. It could be clearly observed that

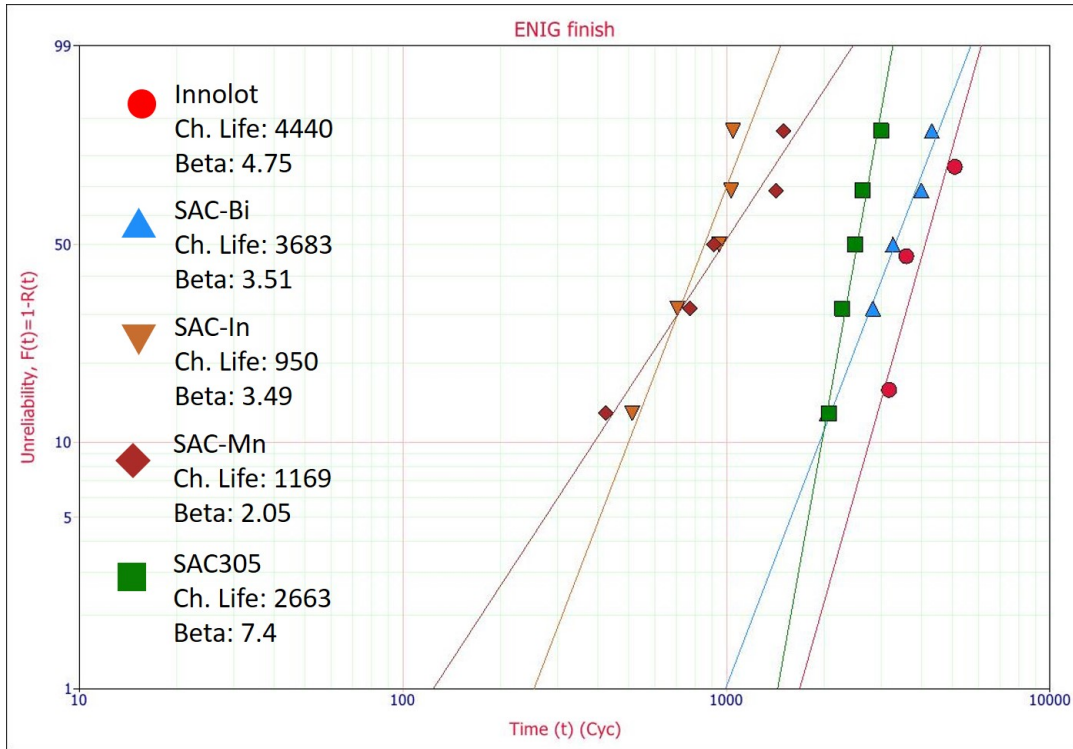


Figure 6.5: Weibull analysis for different alloys with ENIG finish.

the SAC alloys with Bi performed better in the lot. Innolot performed the best with fewer failures, followed by SAC-Bi, and followed by SAC305. The alloys without Bi, but with Mn and In did not perform well. Figure 6.7 shows the summary of B10 life that could be used to

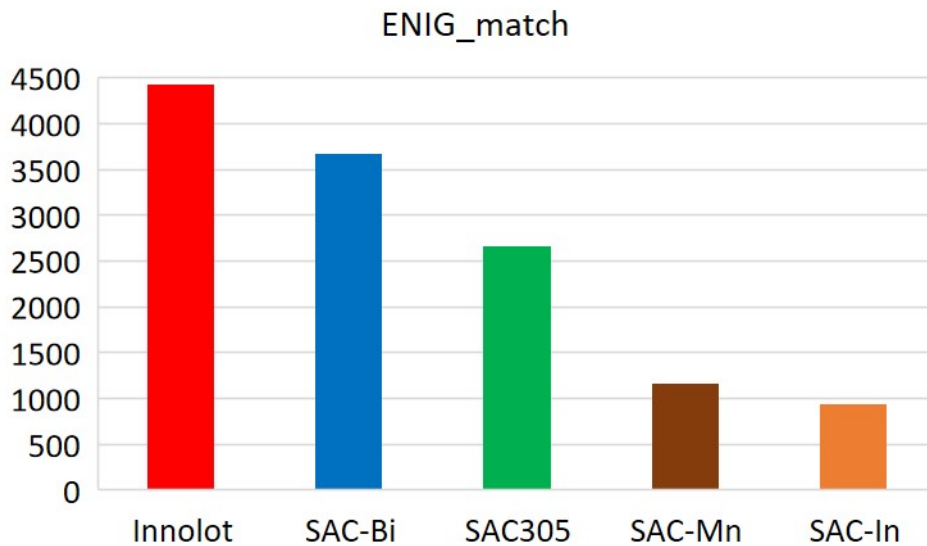


Figure 6.6: Summary of characteristic life for different alloys with ENIG finish.

study early failures. Early failure in the case of SAC-Bi ties it with SAC305 and Innolot has the highest B10 life as well.

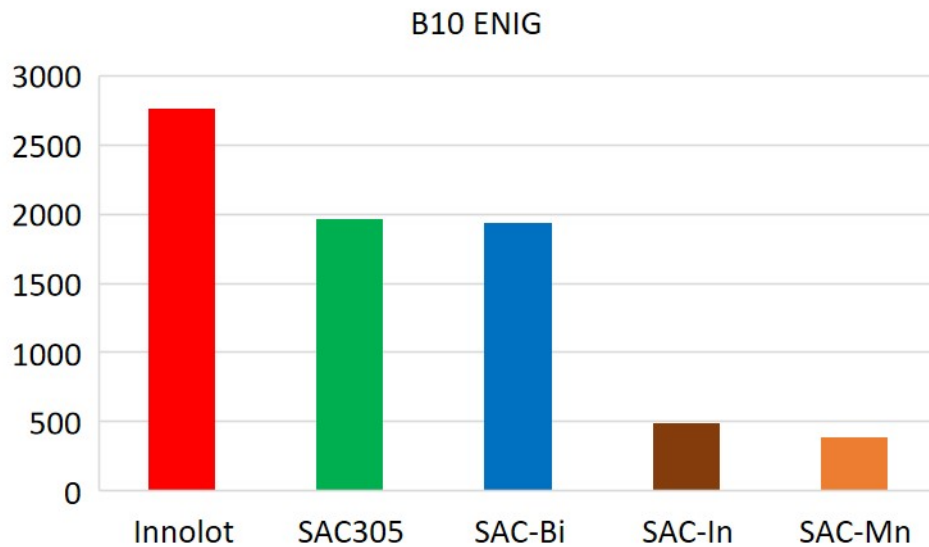


Figure 6.7: Summary of B10 life for different alloys with ENIG finish.

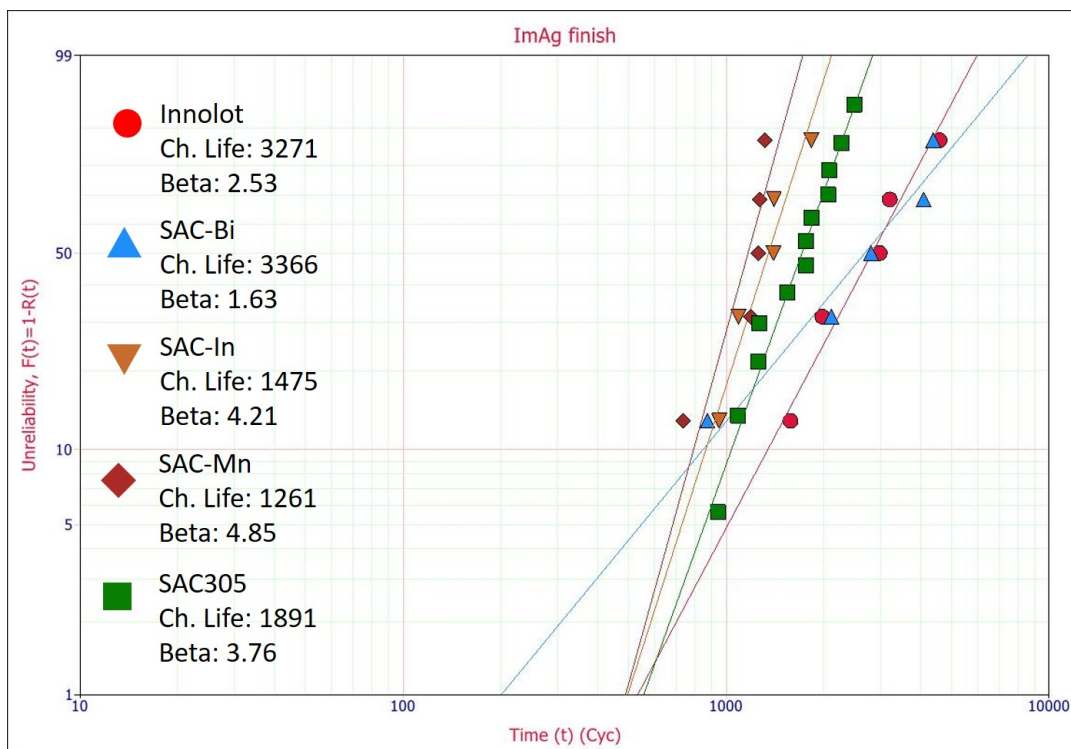


Figure 6.8: Weibull analysis for different alloys with ImAg finish.

Figure 6.8 shows the Weibull analysis for different alloys in the case of ImAg surface finish. Figure 6.9 and Figure 6.10 summarize the characteristic life and B10 life in the case of

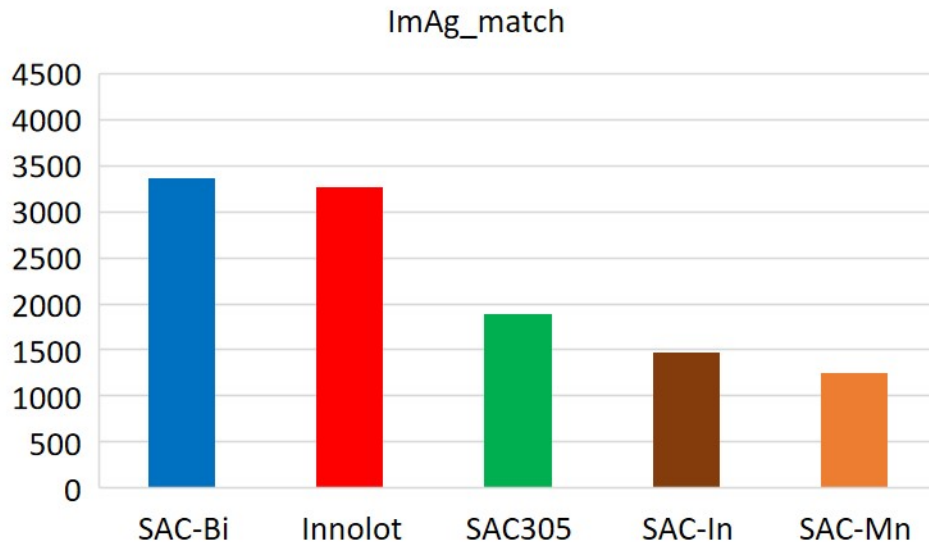


Figure 6.9: Summary of characteristic life for different alloys with ImAg finish.

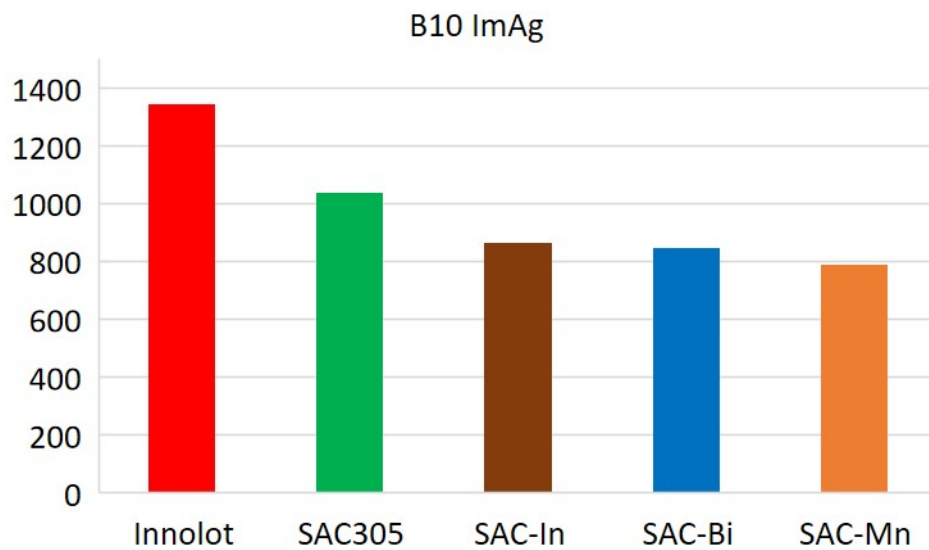


Figure 6.10: Summary of B10 life for different alloys with ImAg finish.

ImAg. With respect to characteristic life, Innolot and SAC-Bi perform closely with SAC-Bi performing slightly better. These alloys are followed by SAC305, which is then followed by non Bi alloys. As can be observed in the Weibull plot, SAC-Bi paste is pulled down in the case of B10 life due to early failure. Except for SAC-Bi, other alloys are observed to follow the same trend as in the case of characteristic life.

Weibull analysis in the case of OSP is presented in Figure 6.11. SAC-Bi leads the pack with characteristic life around 3,000 cycles followed by Innolot. In the case of OSP, SAC305

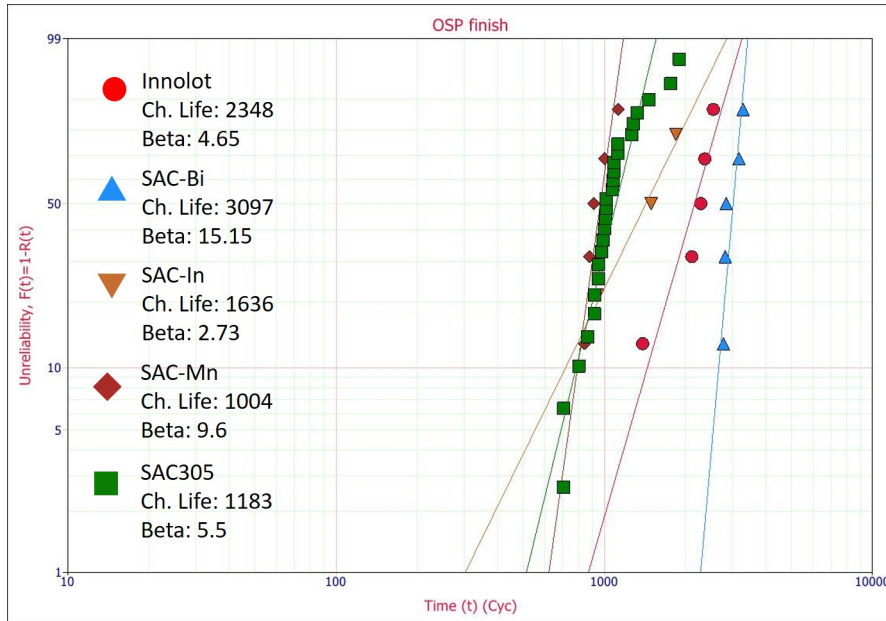


Figure 6.11: Weibull analysis for different alloys with OSP finish.

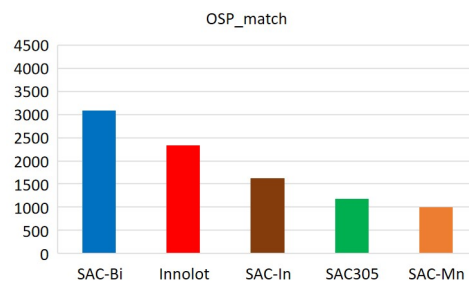


Figure 6.12: Summary of characteristic life for different alloys with OSP finish.

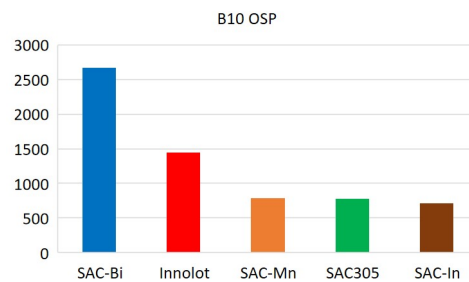


Figure 6.13: Summary of B10 life for different alloys with OSP finish.

falls behind SAC-In unlike ENIG and ImAg finishes. Figure 6.12 shows the characteristic life. B10 life, shown in Figure 6.13, follows the same pattern as the characteristic life.

Figure 6.14 shows the main effect plot considering the factors, solder paste, elements (other than Sn) and finish, and Figure 6.15 shows the interaction of different factors. Elements were grouped into three categories based on their composition as shown in Table 6.3. Solder

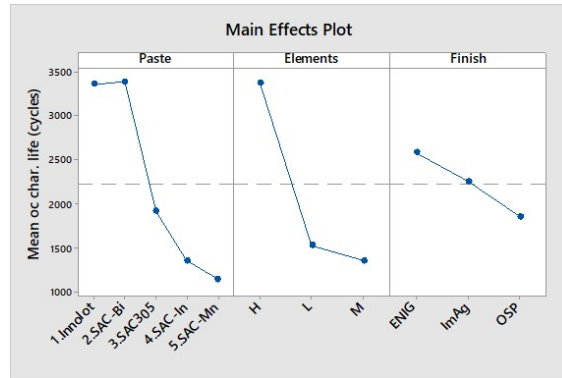


Figure 6.14: ANOVA analysis - Main effects plot.

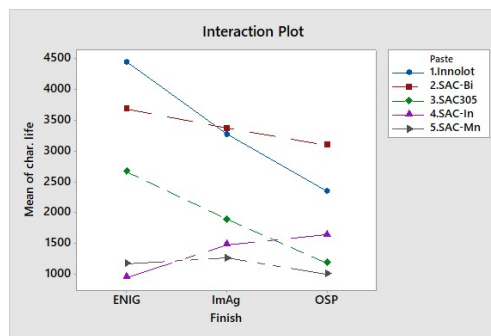


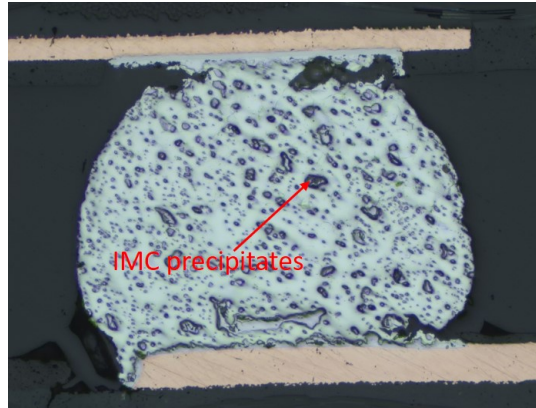
Figure 6.15: ANOVA analysis - Interaction effects plot.

Alloy	(100-Sn)%	High/Med/Low
Innolot	9.05	H
SAC-Bi	7.2	H
SAC-In	5.03	M
SAC-Mn	1.53	L
SAC305	3.5	L

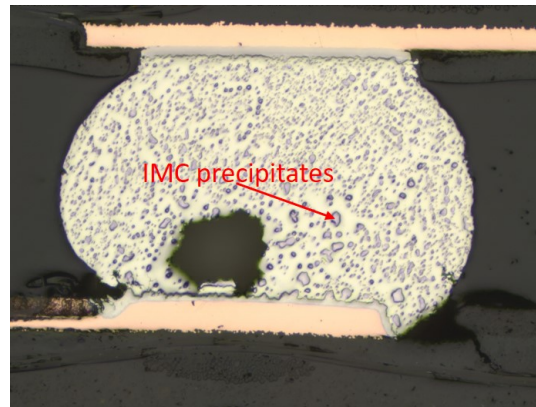
Table 6.3: Element content.

alloys with elements less than 4% are grouped as low, between 4% and 7% is considered as medium, and between 7% and 10% is categorized as high.

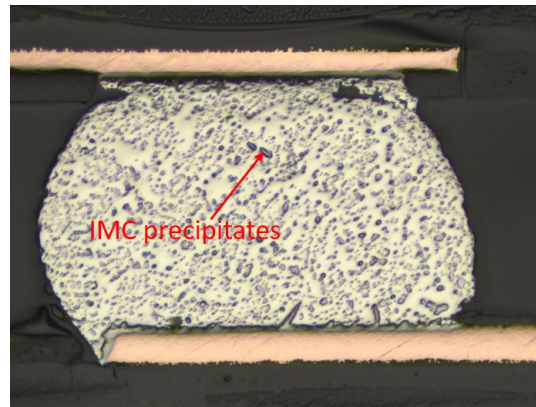
From the main effects plot, it could be clearly seen that reliability improves drastically with addition of Bi in the alloy. Other elements do not appear to improve reliability in the absence of Bi. It could also be seen that the reliability improves with the content of other elements even though it doesn't hold true for low and medium alloys, probably due to the absence of Bi. ENIG appears to perform the best in the case of surface finish, which could be attributed to the Ni layer that blocks the diffusion of Cu from the pads to the bulk as we saw in the previous chapter. When it comes to the interaction plot, it could be seen that for SAC alloys with Bi



(a) Cross-section of SAC-In alloy



(b) Cross-section of SAC-Bi alloy

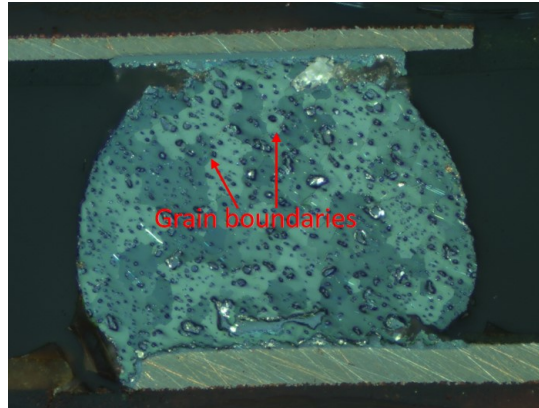


(c) Cross-section of Innolot alloy

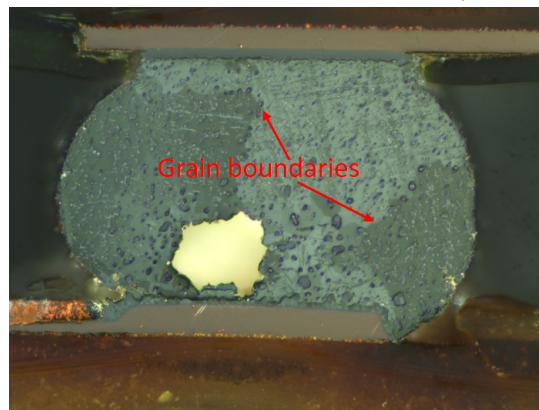
Figure 6.16: Cross-section images of different alloys.

and SAC305, combination with ENIG appears to perform the best. But for the other alloys, the trend seems to be reversed where OSP and ImAg performs better than ENIG.

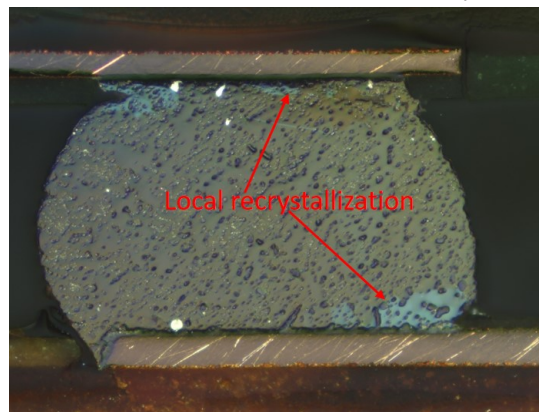
Figure 6.16a, Figure 6.16b and Figure 6.16c show the cross section of solder joints with SAC-In, SAC-Bi and Innolot alloy, respectively. Aging has caused the IMC precipitates to coarsen and from the images, it could be seen that the coarsening varies according to the alloy.



(a) Cross-section of SAC-In alloy



(b) Cross-section of SAC-Bi alloy



(c) Cross-section of Innolot alloy

Figure 6.17: Polarized cross-section images of different alloys.

SAC with Bi has less coarsening when compared to SAC-In. Fine uniformly spread precipitates are more effective in blocking dislocation movements and this variation in the amount of coarsening is also reflected in the characteristic life of these alloys.

Figure 6.17a, Figure 6.17b and Figure 6.17c present the polarized images of SAC-In, SAC-Bi and Innolot alloys, respectively. During the thermal cycling, several sub-grains are formed

due to thermally induced strain [86]. In the case of a solder joint, these strains are concentrated near the solder/component interface, which has NSMD pads. Gradually a crack is initiated in this region, propagates along the grain boundaries, and results in a failure. The composition and precipitates play a major role in blocking the grain sliding and crack propagation. From the polarized images, it could be seen that the amount of recrystallization depends on the alloy composition. SAC-In appears to have the most recrystallization followed by SAC-Bi and Innolot appears to have the least amount of re-crystallization.

It has been reported by Terashima et al. [86] that addition of 0.05 mass%Ni has reduced the amount of coarsening and recrystallization in SAC based alloys. In another study by Terashima [89], recrystallization in thermal fatigue was studied in Sn-1.2Ag-0.5Cu-0.05Ni and Sn-1.2Ag-0.5Cu solders and it was concluded that the increase of thermal fatigue life due to addition of Ni was not from fine Sn grain formation before thermal fatigue, but from suppression of Sn grain growth after recrystallization. These conclusions align with the observation in the study that Ni content in Innolot has contributed to minimizing of recrystallization. In addition, the micro-alloying of elements such as Bi, Sb and Ni is done to provide solid strengthening to compensate for the loss of strength after coarsening of Ag_3Sn [92]. This difference in microstructure is also reflected in the fatigue life of the alloys in the study.

6.4 Conclusion

Component reliability of four different alloys were studied under three different surface finishes using CABGA208 package. It could be concluded that with alloys with higher amount of micro-alloyed elements (other than Sn) performed better. Innolot with elements Bi, Sb and Ni showed high reliability in thermal cycling, followed by SAC-Bi. SAC-Bi was found to have more early failures than Innolot. Surface finish was also found to have a significant impact on component reliability. SAC-Mn and SAC-In performed better with OSP than with ENIG, unlike the other alloys.

Chapter 7

Effect of Aging on Thermal Cycling Reliability of Micro-Alloyed Solders

7.1 Introduction

Since the beginning of the tests conducted in this study, several manufacturers have come up with new solder materials adding Indium (In), Antimony (Sb) and Bismuth (Bi) in increased amounts (>4%). The study in this chapter is based on these solder alloys solicited from leading manufacturers around the globe. The test profile has been changed to induce failure at a faster rate. The details of the test are described in the following sections.

7.2 Setup and Procedure

The test vehicle used in this study is the same as the one used in the previous studies. All solder alloys involved are mentioned in Table 7.1.

OSP surface finish and SAC305 solder spheres were selected for the study. Only one level was included in each factor, in order to reduce the variability. The components populated on the test vehicle are three $15mm \times 15mm$ CABGA208s with SAC305 solder spheres, CABGA36 - LGAs and a series of six 2512SMRs. Both aged and non-aged boards were included in the study and the set of aged boards was exposed to 125°C for a period of three months. For each solder paste, there were five aged and five non-aged boards included in the test as shown in Table 7.2.

Both sets of boards were thermal cycled with the thermal profile shown in Figure 7.1. The temperature range was from -40°C to +125°C with ramp rate of 10°C per minute and dwell times of 15 minutes at both extreme temperatures. As in previous studies, a failure was defined as occurrence of increase in resistance of hundred ohms for five consecutive measurements.

Paste	Manufacturer	Commercial Name	Label	Composition
1	Alpha	SAC305	A	Sn-3.0Ag-0.5Cu
2	Alpha	INNOLOT	B	Sn-3.8Ag-0.7Cu-3.0Bi-1.4Sb-0.15Ni
3	Indium	Violet	C	Sn-2.25Ag-0.5Cu-6.0Bi
4	Indium	818-70-1	D	Sn-3.2Ag-0.7Cu-5.5Sb-0.1Ni
5	Indium	845-27-4	E	Sn-Ag-Cu-Sb-Bi-In-Ni
6	AIM	REL 61	F	Sn-Ag-Cu-Bi ++
7	Accurus	Cyclomax	G	Sn-4.0Ag-0.5Cu-3.0Bi
8	Senju	M794	H	Sn-3.4Ag-0.7Cu-3.2Bi-3.0Sb
9	KOKI	SB6NX58	I	Sn-3.5Ag-0.8Cu-0.5Bi-6.0In
10	Nihon Superior	LF-C2 P608	J	Sn-3.5Ag-1.0Cu-3.0Bi
11	Heraeus	Innotot	K	Sn-3.5Ag-0.7Cu-3.0Bi-1.5Sb-0.15Ni
12	Inventec	EcoRel HTO150-16LVD	L	Sn-Ag-Cu ++
13	Kester	NP505-HR	M	Sn-3.5Ag-0.8Cu-Bi-Sb-Co
14	AIM	REL 22	N	Sn-Ag-Cu ++

Table 7.1: Solder alloys in the study.

Solder paste	Aging (months)	Components	# of components
Solder Alloy (A...N)	0	CABGA 208	15
		CABGA 36 - LGAs	15
		2512SMR	30
	3	CABGA 208	15
		CABGA 36 - LGAs	15
		2512SMR	30

Table 7.2: Test matrix.

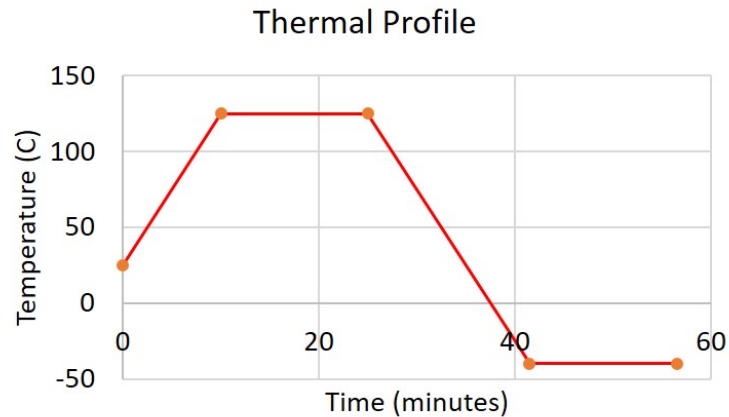


Figure 7.1: Thermal profile used for test.

7.3 Results

Currently, 7,000+ thermal cycles are completed and all larger BGAs (CABGA 208) failed while some of the SMR2512s and few LGAs failed. In the case of SMRs and LGAs, the data was not sufficient for Weibull analysis. Only the data regarding large BGAs is considered in this study.

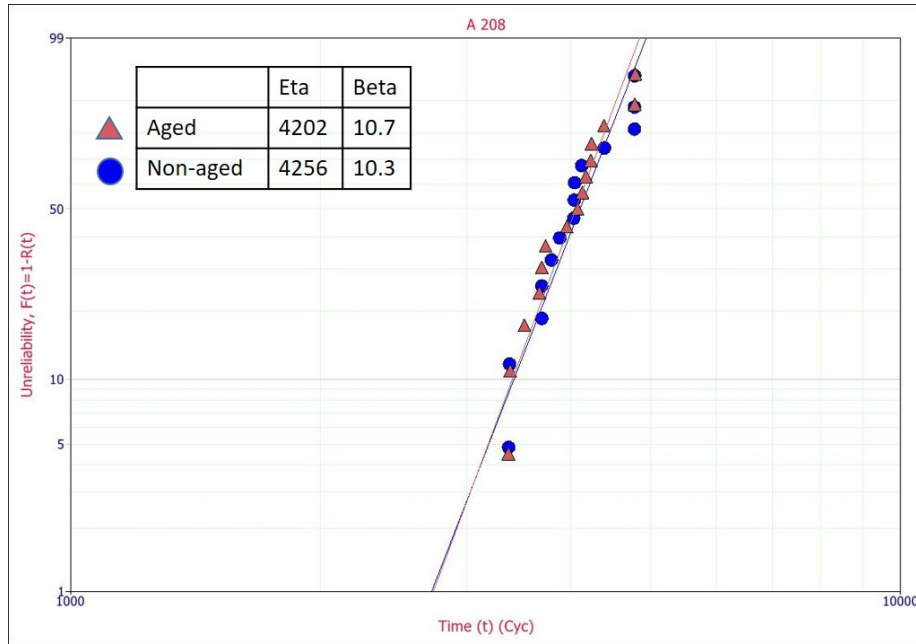


Figure 7.2: Weibull analysis for paste A (SAC305).

Weibull analysis was used as preliminary analysis of the data. Each Weibull plot compares aged and non-aged fatigue life for each alloy.

Figures 7.2 through 7.15 show the Weibull plot for different alloys included in the study. All cases follow a general trend in which the life deteriorates after aging. Considering the period of aging and the type of component, not all alloys had significant difference between aged and non-aged fatigue life. The ANOVA analysis tables for different alloys are provided in Appendix A.

From the characteristic life (Eta) obtained from the Weibull analysis of different solder alloys, it could be seen that the effect of aging for a period of three months is not significant in the case of CABGA 208. It could be of significance for components with longer life, SMR2512 and LGAs in this study. From a statistical point of view, alloys D, F, G and M had significant differences between aged and non-aged samples with $p < 0.05$.

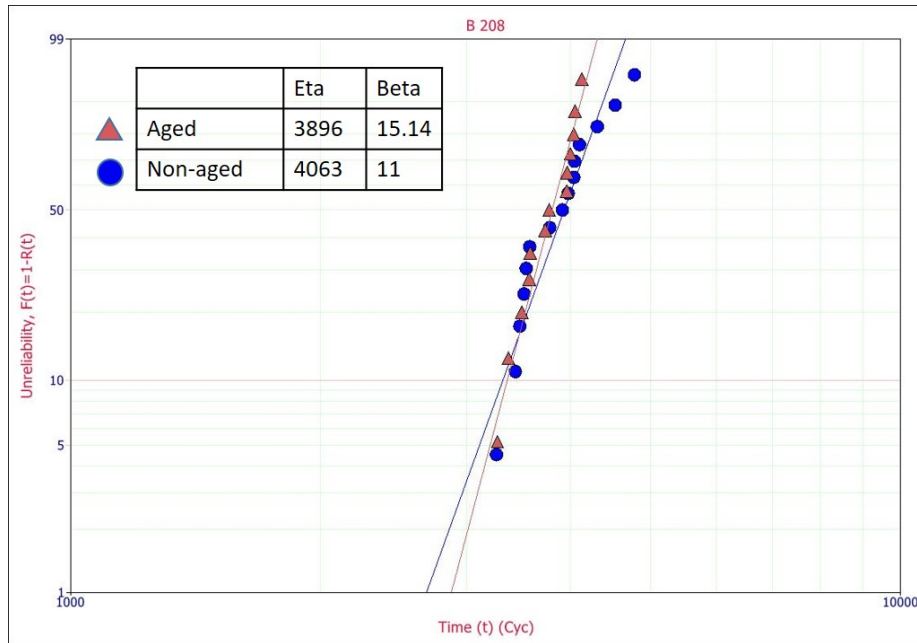


Figure 7.3: Weibull analysis for paste B (Innolot-A).

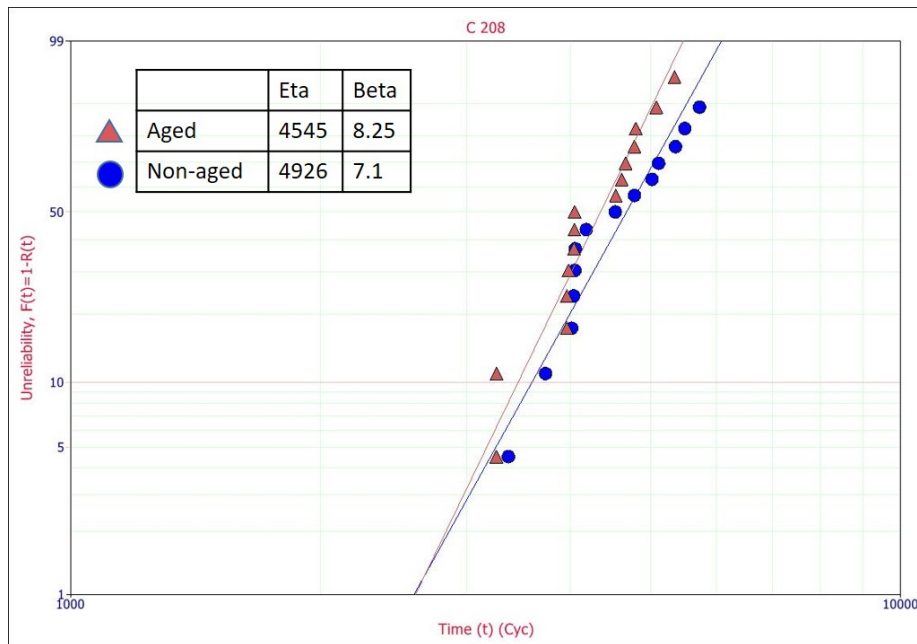


Figure 7.4: Weibull analysis for paste C (SAC-6.0Bi).

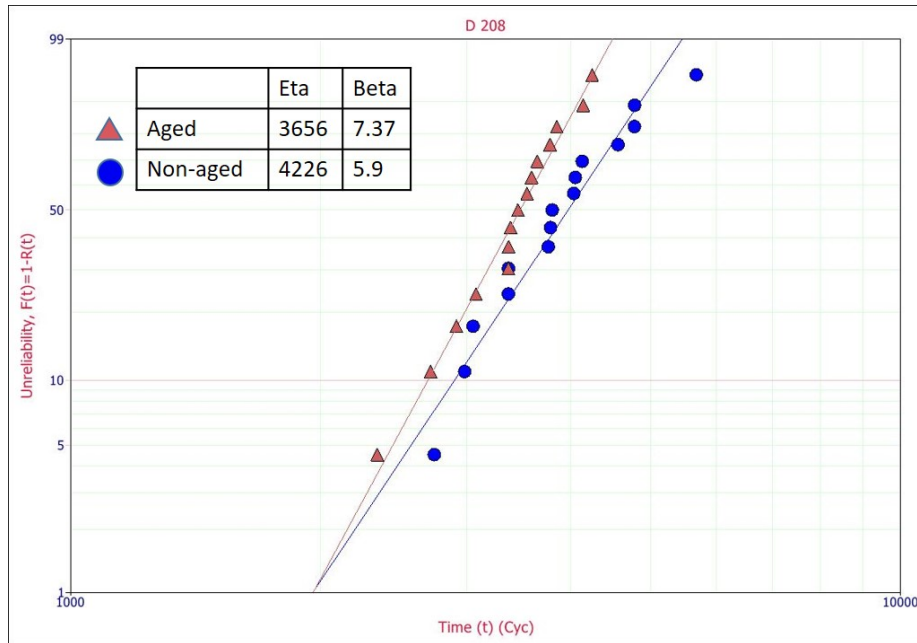


Figure 7.5: Weibull analysis for paste D (SAC-5.5Sb-Ni).

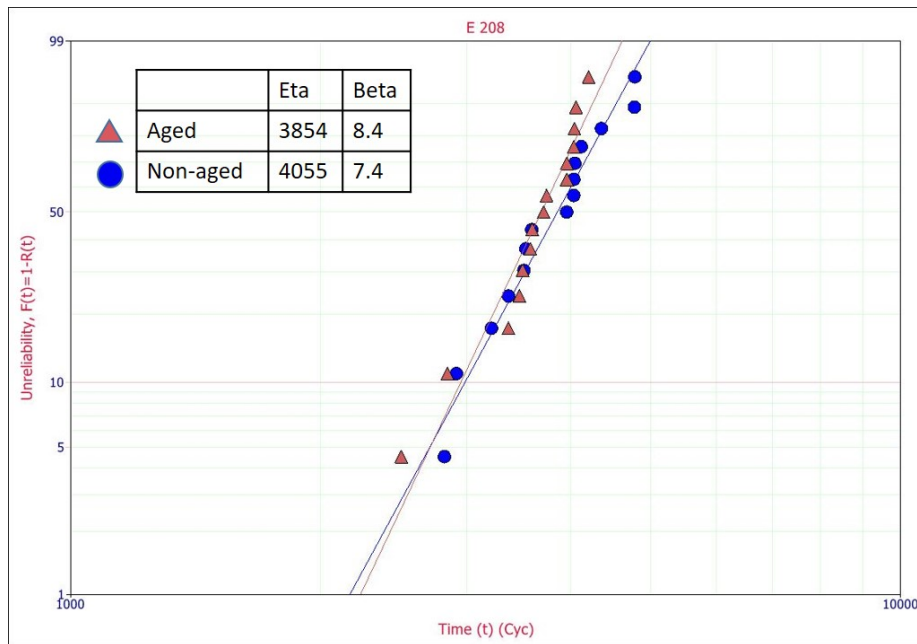


Figure 7.6: Weibull analysis for paste E (SAC-Sb-Bi-In-Ni).

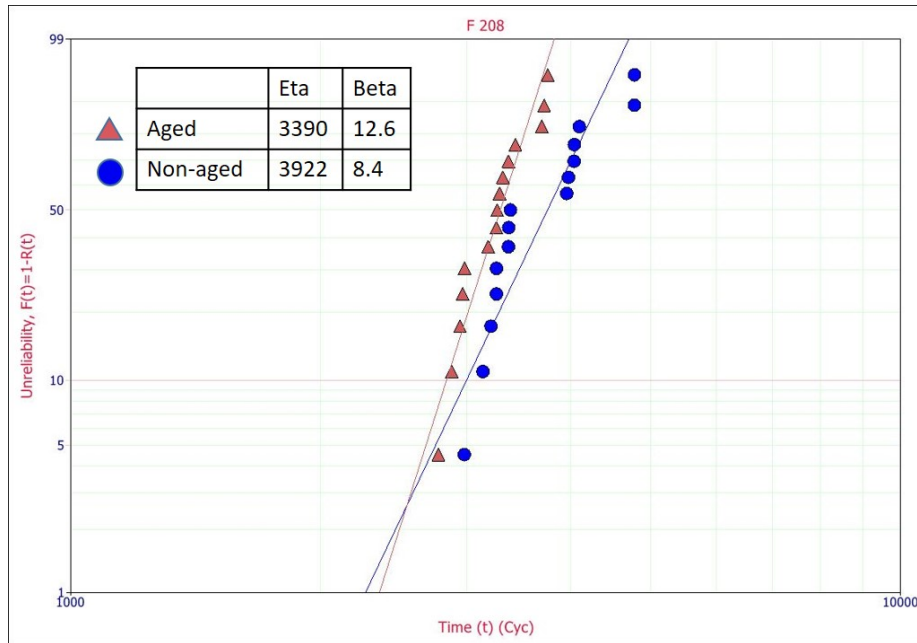


Figure 7.7: Weibull analysis for paste F (SAC-Bi++).

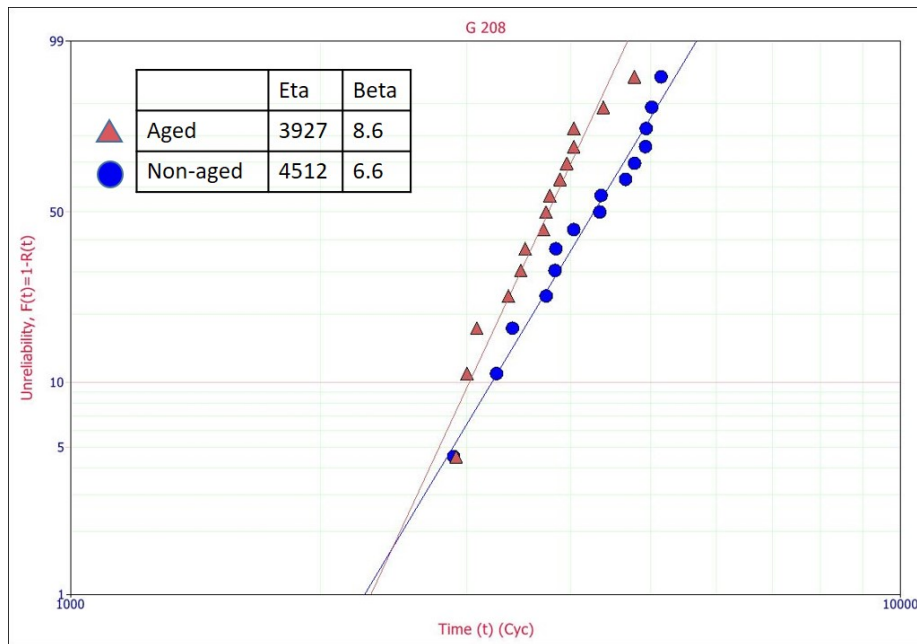


Figure 7.8: Weibull analysis for paste G (SAC-Bi).

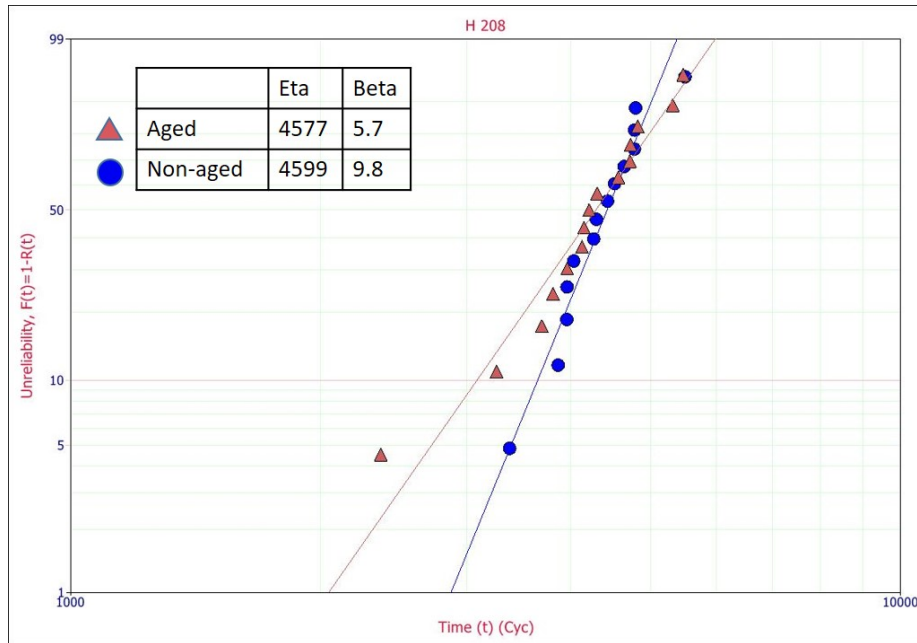


Figure 7.9: Weibull analysis for paste H (SAC-Bi-Sb).

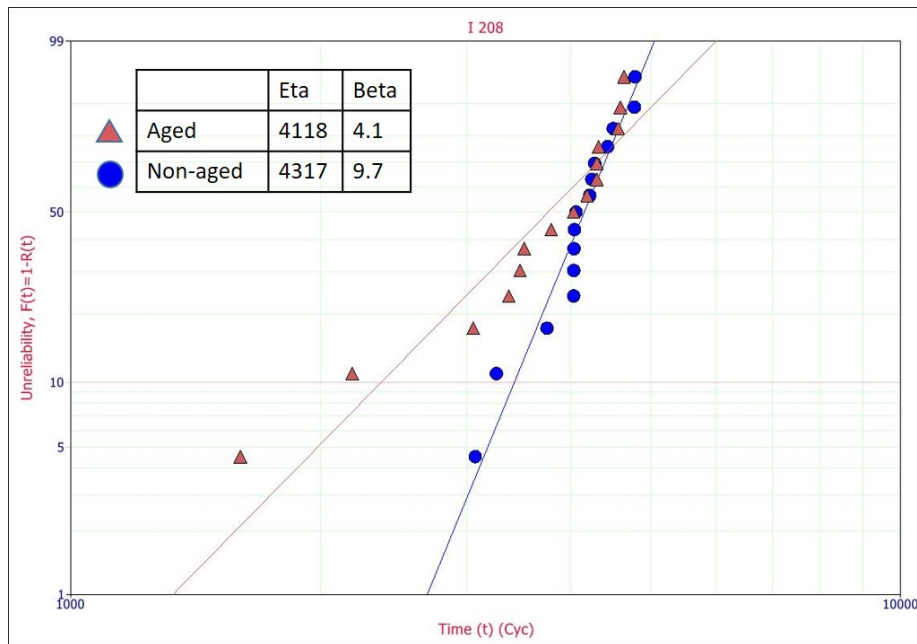


Figure 7.10: Weibull analysis for paste I (SAC-0.5Bi-6.0In).

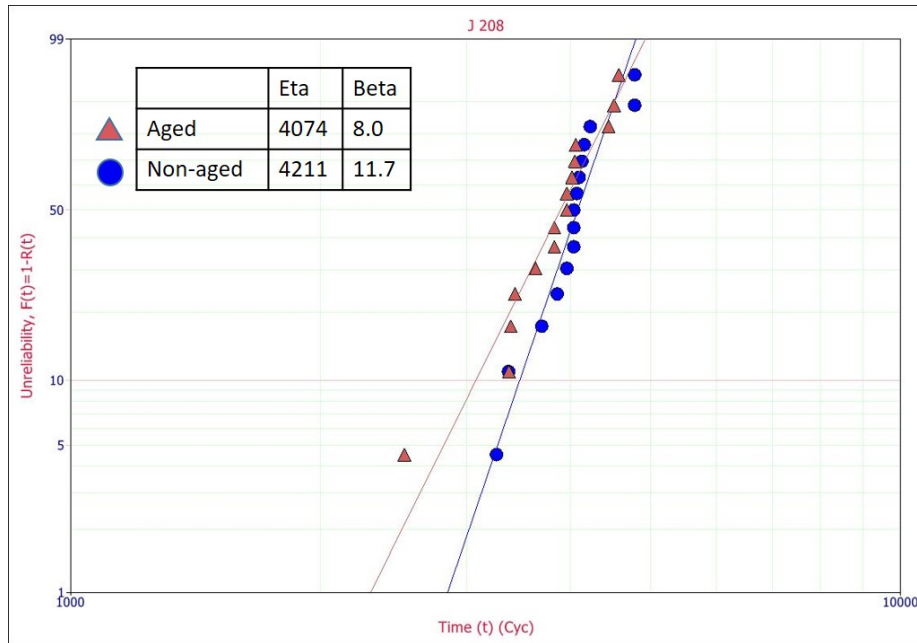


Figure 7.11: Weibull analysis for paste J (SAC-Bi).

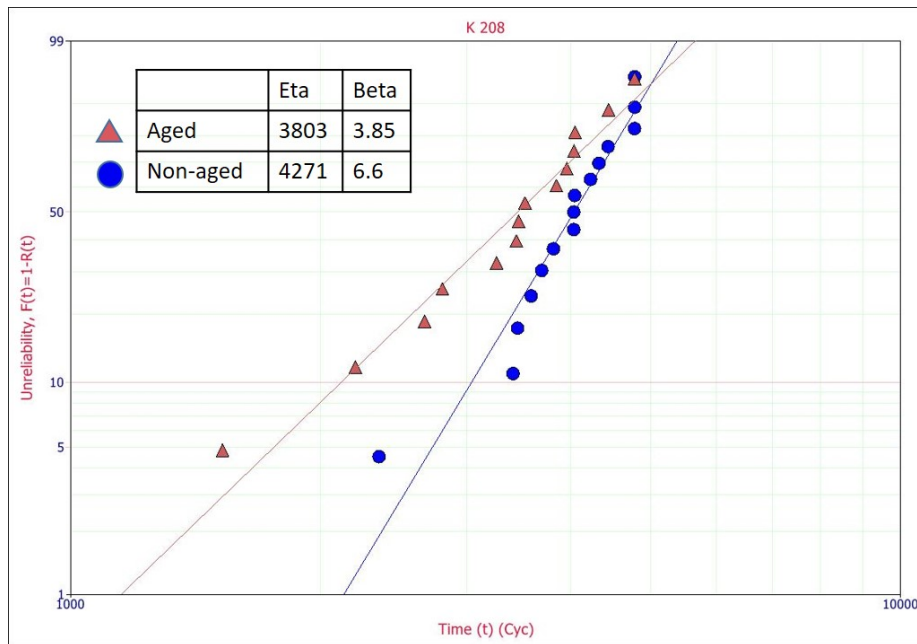


Figure 7.12: Weibull analysis for paste K (Innolot-H).

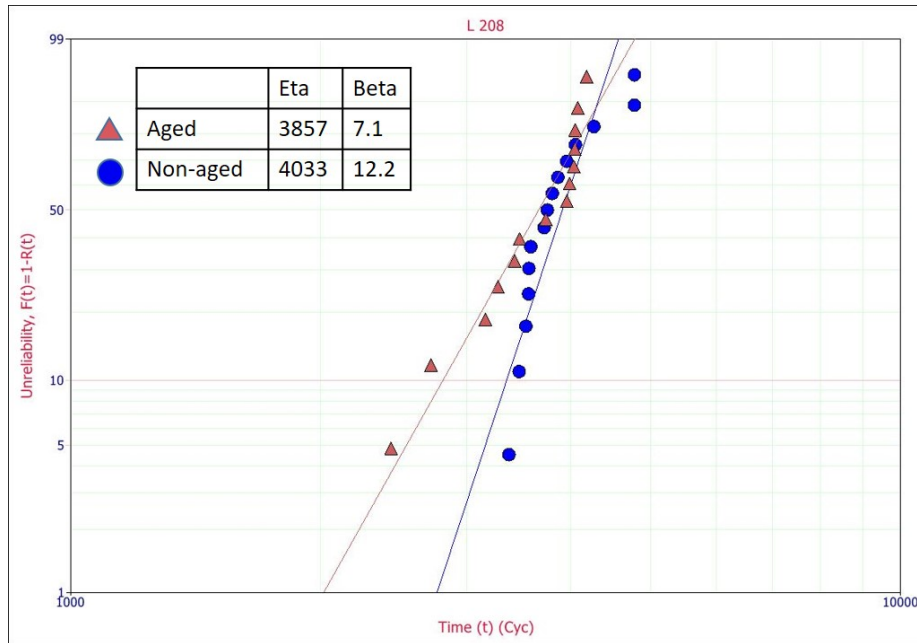


Figure 7.13: Weibull analysis for paste L (SAC++).

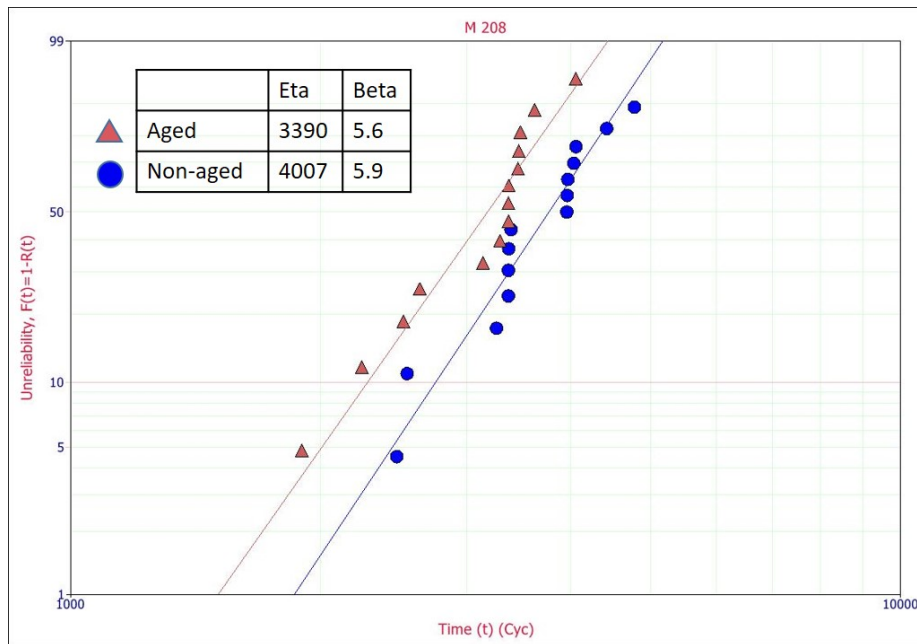


Figure 7.14: Weibull analysis for paste M (SAC-Bi-Sb-Co).

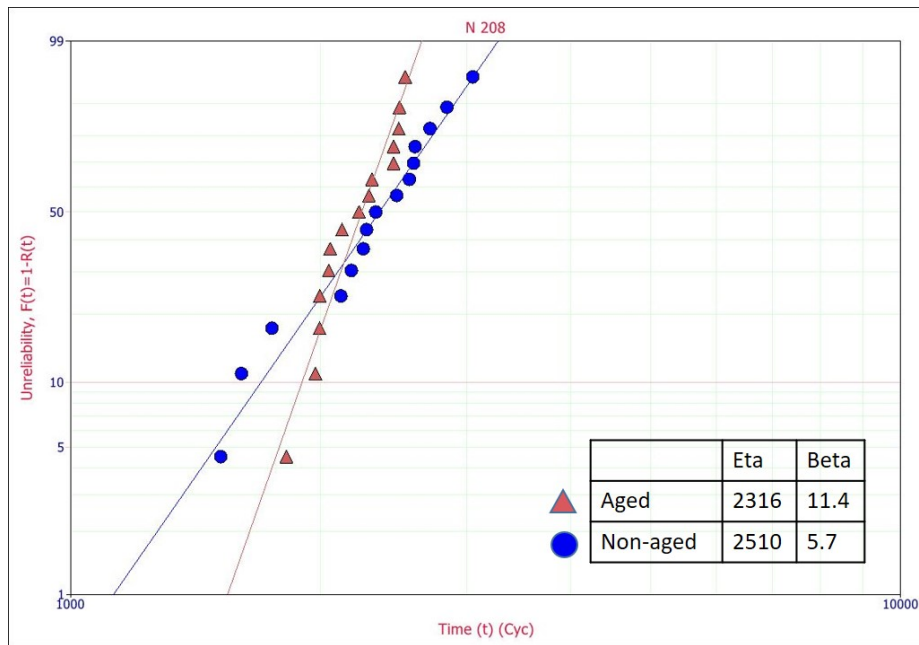


Figure 7.15: Weibull analysis for paste N (SAC++).

Chapter 8

Conclusion and Future Work

8.1 Conclusion

Two main studies were done in this project. Thermal cycling test was done in order to study the component reliability. In depth analysis of the effect of surface finish (ENIG, ImAg, OSP) and Bi content in solder paste on the component reliability was conducted and the following conclusions could be drawn:

- ENIG surface finish was the most reliable, followed by ImAg and OSP.
- ENIG finish was also associated with the least IMC layer thickness due to additional layer of Ni.
- Joints with ENIG had finer micro-structure as the finish prevented diffusion of Cu from the pads.
- Among the alloys considered in the study, micro-alloyed solders had higher reliability than SAC305 after aging.
- Higher reliability was associated with alloys with more micro-alloyed elements (Bi, Sb, and Ni).
- Crack propagation was along the grain boundaries formed by re-crystallization.

8.2 Future Work

It was found that in the test where samples were aged for a period of three months, the differences in fatigue life between aged and non-aged samples were not that significant for CABGA208s when compared to CABGA36 - LGAs and SMRs. It would be interesting to study whether the effect of aging comes into play for larger components, which fail quicker than the smaller components. The best five solder materials from the study could be selected for further testing with longer aging periods.

In most of the high reliability applications, high temperature is accompanied with continuous vibration. Combining thermal cycling and vibration reliability tests could narrow down the differences between lab conditions and real world conditions.

References

- [1] P. Towashiraporn, K. Gall, G. Subbarayan, B. McIlvanie, B. C. Hunter, D. Love, and B. Sullivan, "Power Cycling Thermal Fatigue of Sn-Pb Solder Joints on a Chip Scale Package," *International Journal of Fatigue*, vol. 26, no. 5, pp. 497–510, 2004.
- [2] G. J. S. Chou, "Microstructure Evolution of SnPb and SnAg/Cu BGA Solder Joints During Thermal Aging," in *Proc. 8th International Advanced Packaging Materials Symposium*, pp. 39–46, 2002.
- [3] R. Coyle, H. McCormick, J. Osenbach, P. Read, R. Popowich, D. Fleming, and J. Manock, "The Effect of Silver Content on the Solder Joint Reliability of a Pb-Free PBGA Package," in *Proc. SMTA International*, SMTAi, 2010.
- [4] E. George, D. Das, M. Osterman, and M. Pecht, "Thermal Cycling Reliability of Lead-Free Solders (SAC305 and Sn3.5Ag) for High-Temperature Applications," *IEEE Transactions on Device and Materials Reliability*, vol. 11, no. 2, pp. 328–338, 2011.
- [5] Y. Zhang, Z. Cai, J. C. Suhling, P. Lall, and M. J. Bozack, "The Effects of Aging Temperature on SAC Solder Joint Material Behavior and Reliability," in *Proc. 58th Electronic Components and Technology Conference*, pp. 99–112, 2008.
- [6] J. Dally, P. Lall, and J. Suhling, *Mechanical Design of Electronic Systems*. College House Enterprises, 2008.
- [7] "www.digikey.com."
- [8] "spinningnumber.org."

- [9] “www.innofour.com.”
- [10] J. Evans, “Lectures given at Auburn University.”
- [11] “www.kurtzsa.com.”
- [12] “www.pcbcart.com.”
- [13] T. Burnette, “Introduction to the Plastic Ball Grid Array (PBGA) Q1, 2008.”
- [14] “AN-1126 BGA (Ball Grid Array).”
- [15] C. Zhao, *Board Level Reliability of Lead-Free Solder Interconnections with Solder Doping Under Harsh Environment*. PhD thesis, Auburn University, 2017.
- [16] “www.tutorialsworld.com.”
- [17] “<http://www.bestpcbs.com>.”
- [18] L. J. Turbini, G. C. Munie, D. Bernier, J. Gamalski, and D. W. Bergman, “Examining the environmental impact of lead-free soldering alternatives,” in *Proc. IEEE International Symposium on Electronics and the Environment (Cat. No.00CH37082)*, pp. 46–53, 2000.
- [19] D. A. Shnawah, M. F. M. Sabri, and I. A. Badruddin, “A review on thermal cycling and drop impact reliability of sac solder joint in portable electronic products,” *Microelectronics Reliability*, vol. 52, no. 1, pp. 90–99, 2012. 2011 Reliability of Compound Semiconductors (ROCS) Workshop.
- [20] “hellerindustries.com.”
- [21] “www.cambridge-sensotec.co.uk.”
- [22] “www.pcbway.com.”
- [23] R. Coyle, J. Osenbach, M. N. Collins, H. McCormick, P. Read, D. Fleming, R. Popowich, J. Punch, M. Reid, and S. Kummerl, “Phenomenological Study of the Effect of Microstructural Evolution on the Thermal Fatigue Resistance of Pb-Free Solder Joints,”

- IEEE Transactions on Components, Packaging and Manufacturing Technology*, vol. 1, no. 10, pp. 1583–1593, 2011.
- [24] J. W. R. Teo, “Thermal Cycling Aging Effect on the Reliability and Morphological Evolution of SnAgCu Solder Joints,” *IEEE Transactions on Electronics Packaging Manufacturing*, vol. 30, pp. 279–284, Oct 2007.
- [25] J. Zhang, Z. Hai, S. Thirugnanasambandam, J. L. Evans, M. J. Bozack, Y. Zhang, and J. C. Suhling, “Thermal Aging Effects on the Thermal Cycling Reliability of Lead-Free Fine Pitch Packages,” *IEEE Transactions on Components, Packaging and Manufacturing Technology*, vol. 3, no. 8, pp. 1348–1357, 2013.
- [26] Y. Lei, J. Yang, J. Lin, H. Fu, B. Liu, H. Bai, and J. Qin, “The influence of silver content on the reliability of lead-free solder joints under drop condition,” in *Proc. 14th International Conference on Electronic Packaging Technology*, no. 20101103120023, pp. 826–829, 2013.
- [27] F. Liu and G. Meng, “Random Vibration Reliability of BGA Lead-Free Solder Joint,” *Microelectronics Reliability*, vol. 54, no. 1, pp. 226–232, 2014.
- [28] H. W. Zhang, Y. Liu, J. Wang, and F. L. Sun, “Effect of Elevated Temperature on PCB Responses and Solder Interconnect Reliability under Vibration Loading,” *Microelectronics Reliability*, vol. 55, no. 11, pp. 2391–2395, 2015.
- [29] S. Hamasha, S. Su, F. Akkara, A. Dawahdeh, P. Borgesen, and A. Qasaimeh, “Solder Joint Reliability in Isothermal Varying Load Cycling,” in *Proc. 16th IEEE Intersociety Conference on Thermal and Thermomechanical Phenomena in Electronic Systems (ITherm)*, pp. 1331–1336, IEEE, May 2017.
- [30] J. Gu, J. Lin, Y. Lei, and H. Fu, “Experimental Analysis of Sn-3.0Ag-0.5Cu Solder Joint Board-Level Drop/Vibration Impact Failure Models After Thermal/Isothermal Cycling,” *Microelectronics Reliability*, vol. 80, pp. 29–36, Jan 2018.

- [31] Y. Kariya, T. Hosoi, S. Terashima, M. Tanaka, and M. Otsuka, "Effect of Silver Content on the Shear Fatigue Properties of Sn-Ag-Cu Flip-Chip Interconnects," *Journal of Electronic Materials*, vol. 33, no. 4, pp. 321–328, 2004.
- [32] N. Fu, J. C. Suhling, and P. Lall, "Cyclic Stress-Strain Behavior of SAC305 Lead Free Solder: Effects of Aging, Temperature, Strain Rate, and Plastic Strain Range," in *Proc. IEEE 66th Electronic Components and Technology Conference (ECTC)*, pp. 1119–1127, IEEE, May 2016.
- [33] G. Y. Li and X.-q. Shi, "Effects of Bismuth on Growth of Intermetallic Compounds in Sn-Ag-Cu Pb-Free Solder Joints," *Transactions of Nonferrous Metals Society of China*, vol. 16, pp. s739–s743, Jun 2006.
- [34] A. A. El-Daly, A. M. El-Taher, and S. Gouda, "Development of New Multicomponent Sn-Ag-Cu-Bi Lead-Free Solders for Low-Cost Commercial Electronic Assembly," *Journal of Alloys and Compounds*, vol. 627, pp. 268–275, 2015.
- [35] G. Y. Li, X. B. Jiang, B. Li, P. Chen, and R. Liao, "Influence of Dopant on IMC Growth and Mechanical Properties of Sn-3.5Ag-0.7Cu Solder Joints," pp. 1–4, 2007.
- [36] F. Gao, T. Takemoto, H. Nishikawa, and A. Komatsu, "Microstructure and mechanical properties evolution of intermetallics between Cu and Sn-3.5Ag solder doped by Ni-Co additives," *Journal of Electronic Materials*, vol. 35, no. 5, pp. 905–911, 2006.
- [37] S. L. Tay, A. S. Haseeb, and M. R. Johan, "Effect of addition Cobalt nanoparticles on Sn-Ag-Cu lead-free solder," *Proc. 12th Electronics Packaging Technology Conference, EPTC 2010*, pp. 433–436, 2010.
- [38] F. Cheng, H. Nishikawa, and T. Takemoto, "Estimation of the Thermal Fatigue Resistance and Creep Properties of the Co/Ni-Bearing SAC305 Lead-Free Solders by the Strain Rate Change Tensile Test," *Materials Transactions*, vol. 49, no. 7, pp. 1503–1507, 2008.

- [39] S. Su, S. Hamasha, and K. Hamasha, "Effect of Surface Finish on the Shear Properties of SnAgCu-Based Solder Alloys," *IEEE Transactions on Components, Packaging and Manufacturing Technology*, vol. 9, pp. 1473–1485, Jul 2019.
- [40] S. Su, N. Fu, F. John Akkara, and S. Hamasha, "Effect of Long-Term Room Temperature Aging on the Fatigue Properties of SnAgCu Solder Joint," *Journal of Electronic Packaging*, vol. 140, no. 3, pp. 31005–31009, 2018.
- [41] H. Black, "Getting the Lead Out of Electronics.," *Environmental Health Perspectives*, vol. 113, pp. A682–5, Oct 2005.
- [42] C. Basaran and R. Chandaroy, "Mechanics of Pb40/Sn60 Near-Eutectic Solder Alloys Subjected to Vibrations," *Applied Mathematical Modelling*, vol. 22, pp. 601–627, Aug 1998.
- [43] D. Frear, D. Grivas, M. McCormack, D. Tribula, and J. W. Morris Jr., "Fatigue and Thermal Fatigue of Pb-Sn Solder Joints," 1987.
- [44] C. E. Ebeling, *An Introduction to Reliability and Maintainability Engineering*. Waveland Press, 2010.
- [45] K. C. Otiaba, R. Bhatti, N. Ekere, S. Mallik, and M. Ekpu, "Finite Element Analysis of the Effect of Silver Content for Sn–Ag–Cu Alloy Compositions on Thermal Cycling Reliability of Solder Die Attach," *Engineering Failure Analysis*, vol. 28, pp. 192–207, Mar 2013.
- [46] F. J. Akkara, C. Zhao, R. Athamenh, S. Su, M. Abueed, S. Hamasha, J. Suhling, and D. P. Lall, "Effect of Solder Sphere Alloys and Surface Finishes on the Reliability of Lead-Free Solder Joints in Accelerated Thermal Cycling," in *Proc. 17th IEEE Intersociety Conference on Thermal and Thermomechanical Phenomena in Electronic Systems (ITherm)*, pp. 1374–1380, IEEE, May 2018.

- [47] F. J. Akkara, C. Zhao, M. Abueed, S. Su, S. Hamasha, J. Suhling, and P. Lall, "Effects of Mixing Solder Sphere Alloys with Bismuth-based Pastes on the Component Reliability in Harsh Thermal Cycling," in *Proc. SMTA International*, SMTA, Oct 2018.
- [48] Y. Zhang, Z. Cai, J. C. Suhling, P. Lall, and M. J. Bozack, "The Effects of Aging Temperature on SAC Solder Joint Material Behavior and Reliability," in *Proc. 58th Electronic Components and Technology Conference*, pp. 99–112, 2008.
- [49] T. T. Mattila, H. Xu, O. Ratia, and M. Paulasto-Krockel, "Effects of thermal cycling parameters on lifetimes and failure mechanism of solder interconnections," in *Proc. 60th Electronic Components and Technology Conference (ECTC)*, pp. 581–590, IEEE, Jun 2010.
- [50] R. Jaeger, *Introduction to Microelectronic Fabrication*. Pearson, 2002.
- [51] R. P. Prasad, "Introduction to Surface Mount Technology," in *Surface Mount Technology*, pp. 3–50, Boston, MA: Springer US, 1997.
- [52] K. H. J. Buschow, *Encyclopedia of Materials: Science and Technology*. Elsevier, 2001.
- [53] M. Arra, D. J. Xie, and D. Shangguan, "Performance of lead-free solder joints under dynamic mechanical loading," in *Proc. Electronic Components and Technology Conference*, pp. 1256–1262, 2002.
- [54] B. C. Baker, "Smaller Packages = Bigger Thermal Challenges," *Microchip Technology*, 2003.
- [55] G. Zweig, "Inspect the process, not the product," 1994.
- [56] C. A. Harper, *Electronic Assembly Fabrication: Chips, Circuit Boards, Packages, and Components*. McGraw-Hill, 2002.
- [57] A. R. Djordjević, R. M. Biljić, V. D. Likar-Smiljanić, and T. K. Sarkar, "Wideband frequency-domain characterization of FR-4 and time-domain causality," *IEEE Transactions on Electromagnetic Compatibility*, vol. 43, no. 4, pp. 662–667, 2001.

- [58] D. A. Benson, R. T. Mitchell, M. R. Tuck, D. R. Adkins, and D. W. Palmer, "Micro-Machined Heat Pipes in Silicon MCM Substrates," in *Proc. IEEE Multi-Chip Module Conference (Cat. No.96CH35893)*, pp. 127–129, 1996.
- [59] L. Criscuolo, B. Technology, and S. Ave, "Using Silicon Contacts to Test and Burn-In FLASH Memory, Microprocessors, and FPGAs," in *Proc. International Conference on Multichip Modules and High Density Packaging (Cat. No.98EX154)*, pp. 388–392, 1998.
- [60] M. Ortolani, M. Leoni, P. Scardi, and M. Golshan, "Residual Stress Profile in Ceramic Laminates," *Zeitschrift fur Kristallographie, Supplement*, vol. 1, no. 26, pp. 91–96, 2007.
- [61] N. Kumbhat, P. Raj, S. Bansal, R. Doraiswami, S. Bhattacharya, R. Tummala, S. Hayes, and S. Atmur, "New Package/Board Materials Technology for Next-Generation Convergent Microsystems," in *Proc. 5th Electronics Packaging Technology Conference (EPTC 2003)*, pp. 331–335, IEEE.
- [62] H. Nakahara, *Types of Printed Wiring Boards*, ch. 2, pp. 19–30. McGraw-Hill, 2007.
- [63] J. S. Hwang, *Lead-Free Implementation and Production: A Manufacturing Guide*. McGraw-Hill, 2004.
- [64] M. Sona and K. N. Prabhu, "Review on Microstructure Evolution in Sn–Ag–Cu Solders and Its Effect on Mechanical Integrity of Solder Joints," *Journal of Materials Science: Materials in Electronics*, vol. 24, pp. 3149–3169, Sep 2013.
- [65] Z. Cai, Y. Zhang, J. C. Suhling, P. Lall, R. W. Johnson, and M. J. Bozack, "Reduction of lead free solder aging effects using doped SAC alloys," in *Proc. 60th Electronic Components and Technology Conference (ECTC)*, pp. 1493–1511, IEEE, 2010.
- [66] M. Ford, "A History of Placement Programming and Optimization," *Printed Circuit Design & Fab Circuits Assembly*, 2015.
- [67] "Reflow Ovens - Convection Reflow Oven System."

- [68] E. W. Kamen, A. Goldstein, O. Asarangchai, A. Fraser, K. Klatka, J. Belmonte, and R. Huber, "Analysis of Factors that Affect Yield in SMT Assembly," *NEPCON West*, vol. 3, pp. 1423–1430, 01 1999.
- [69] Y. Liu, G. Tian, S. Gale, R. W. Johnson, and L. Crane, "Lead-Free Chip Scale Packages: Assembly and Drop Test Reliability," *IEEE Transactions on Electronics Packaging Manufacturing*, vol. 29, no. 1, pp. 1–9, 2006.
- [70] T. Laurila, V. Vuorinen, and M. Paulasto-Kröckel, "Impurity and alloying effects on interfacial reaction layers in Pb-free soldering," *Materials Science and Engineering R: Reports*, vol. 68, no. 1-2, pp. 1–38, 2010.
- [71] I. E. Anderson and J. L. Harringa, "Suppression of void coalescence in thermal aging of tin-silver-copper-X solder joints," *Journal of Electronic Materials*, vol. 35, no. 1, pp. 94–106, 2006.
- [72] E. P. Leng, M. Ding, W. T. Ling, N. Amin, I. Ahmad, M. Y. Lee, and A. Haseeb, "A Study of SnAgNiCo vs Sn3.8AgO. 7Cu C5 Lead Free Solder Alloy on Mechanical Strength of BGA Solder Joint," in *Proc. 10th Electronics Packaging Technology Conference*, pp. 588–594, IEEE, Dec 2008.
- [73] M. Miner, "Cumulative Damage in Fatigue," *Journal of Applied Mechanics*, vol. 12, 1945.
- [74] A. Fatemi and L. Yang, "Cumulative fatigue damage and life prediction theories: a survey of the state of the art for homogeneous materials," *International Journal of Fatigue*, vol. 20, pp. 9–34, Jan 1998.
- [75] Z. Lv, H.-Z. Huang, S.-P. Zhu, H. Gao, and F. Zuo, "A modified nonlinear fatigue damage accumulation model," *International Journal of Damage Mechanics*, vol. 24, pp. 168–181, Mar 2015.
- [76] R. R. Gatts, "Application of a Cumulative Damage Concept to Fatigue," *Journal of Basic Engineering*, vol. 83, p. 529, Dec 1961.

- [77] H. J. Grover, "An Observation Concerning the Cycle Ratio in Cumulative Damage," in *Symposium on Fatigue of Aircraft Structures*, pp. 120–120–5, 100 Barr Harbor Drive, PO Box C700, West Conshohocken, PA 19428-2959: ASTM International.
- [78] P. Borgesen, S. Hamasha, M. Obaidat, V. Raghavan, X. Dai, M. Meilunas, and M. Anselm, "Solder joint reliability under realistic service conditions," *Microelectronics Reliability*, vol. 53, pp. 1587–1591, Sep 2013.
- [79] S. Hamasha, Y. Jaradat, A. Qasaimeh, M. Obaidat, and P. Borgesen, "Assessment of Solder Joint Fatigue Life Under Realistic Service Conditions," *Journal of Electronic Materials*, vol. 43, pp. 4472–4484, Dec 2014.
- [80] H. Corten and T. Dolan, "Cumulative fatigue damage," in *International conference on fatigue of metals*, 1956.
- [81] S.-P. Zhu, H.-Z. Huang, Y. Liu, L.-P. He, and Q. Liao, "A Practical Method for Determining the Corten-Dolan Exponent and Its Application to Fatigue Life Prediction," *Int. J. Turbo Jet-Engines*, vol. 29, pp. 79–87, Jan 2012.
- [82] G. Cheng and A. Plumtree, "A fatigue damage accumulation model based on continuum damage mechanics and ductility exhaustion," *International Journal of Fatigue*, vol. 20, pp. 495–501, Aug 1998.
- [83] M. Wang, Q. Fei, and P. Zhang, "A Modified Fatigue Damage Model for High-Cycle Fatigue Life Prediction," *Advances in Materials Science and Engineering*, vol. 2016, pp. 1–7, Feb 2016.
- [84] M. N. Collins, J. Punch, and R. Coyle, "Surface finish effect on reliability of SAC 305 soldered chip resistors," *Soldering & Surface Mount Technology*, vol. 24, no. 4, pp. 240–248, 2012.
- [85] A. Syed, T. S. Kim, Y. M. Cho, C. W. Kim, and M. Yoo, "Alloying Effect of Ni, Co, and Sb in SAC solder for Improved Drop Performance of Chip Scale Packages with Cu OSP

- Pad Finish,” in *Proc. 8th Electronics Packaging Technology Conference*, pp. 404–411, 2006.
- [86] S. Terashima, K. Takahama, M. Nozaki, and M. Tanaka, “Recrystallization of Sn grains due to thermal strain in Sn-1.2Ag-0.5Cu-0.05Ni solder,” *Materials Transactions*, vol. 45, no. 4, pp. 1383–1390, 2004.
- [87] S. Terashima, Y. Kariya, and M. Tanaka, “Improvement on thermal fatigue properties of Sn-1.2Ag-0.5Cu flip chip interconnects by nickel addition,” *Materials Transactions*, vol. 45, pp. 673–680, Mar 2004.
- [88] J. J. Sundelin, S. T. Nurmi, and T. K. Lepistö, “Recrystallization behaviour of SnAgCu solder joints,” *Materials Science and Engineering A*, vol. 474, pp. 201–207, Feb 2008.
- [89] S. Terashima and M. Tanaka, “Thermal Fatigue Properties of Sn-1.2Ag-0.5Cu-xNi Flip Chip Interconnects,” *Materials Transactions*, vol. 45, pp. 681–688, 2004.
- [90] T. T. Mattila, V. Vuorinen, and J. K. Kivilahti, “Impact of printed wiring board coatings on the reliability of lead-free chip-scale package interconnections,” *Journal of Materials Research*, vol. 19, pp. 3214–3223, Nov 2004.
- [91] D. W. Henderson, J. J. Woods, T. A. Gosselin, J. Bartelo, D. E. King, T. M. Korhonen, M. A. Korhonen, L. P. Lehman, E. J. Cotts, S. K. Kang, P. Lauro, D. Y. Shih, C. Goldsmith, and K. J. Puttlitz, “The microstructure of Sn in near-eutectic Sn-Ag-Cu alloy solder joints and its role in thermomechanical fatigue,” *Journal of Materials Research*, vol. 19, pp. 1608–1612, Jun 2004.
- [92] R. J. Coyle, K. Sweatman, and B. Arfaei, “Thermal Fatigue Evaluation of Pb-Free Solder Joints: Results, Lessons Learned, and Future Trends,” *JOM*, vol. 67, pp. 2394–2415, Oct 2015.

Appendix A

.1 Tables to check for statistical significance

Analysis of Variance

Source	DF	Adj SS	Adj MS	F-Value	P-Value
Aging	1	15698	15698	0.07	0.790
Error	27	5838556	216243		
Total	28	5854254			

Table 1: ANOVA analysis table for paste A (SAC305).

Analysis of Variance

Source	DF	Adj SS	Adj MS	F-Value	P-Value
Aging	1	102882	102882	0.74	0.398
Error	26	3618212	139162		
Total	27	3721094			

Table 2: ANOVA analysis table for paste B (Innolot-A).

Analysis of Variance

Source	DF	Adj SS	Adj MS	F-Value	P-Value
Aging	1	808028	808028	1.68	0.206
Error	28	13496655	482023		
Total	29	14304684			

Table 3: ANOVA analysis table for paste C (SAC-6.0Bi).

Analysis of Variance

Source	DF	Adj SS	Adj MS	F-Value	P-Value
Aging	1	1852816	1852816	4.17	0.051
Error	28	12436702	444168		
Total	29	14289518			

Table 4: ANOVA analysis table for paste D (SAC-5.5Sb-Ni).

Analysis of Variance

Source	DF	Adj SS	Adj MS	F-Value	P-Value
Aging	1	207085	207085	0.71	0.406
Error	28	8133731	290490		
Total	29	8340816			

Table 5: ANOVA analysis table for paste E (SAC-Sb-Bi-In-Ni).

Analysis of Variance

Source	DF	Adj SS	Adj MS	F-Value	P-Value
Aging	1	1556785	1556785	7.25	0.012
Error	28	6009813	214636		
Total	29	7566598			

Table 6: ANOVA analysis table for paste F (SAC-Bi++).

Analysis of Variance

Source	DF	Adj SS	Adj MS	F-Value	P-Value
Aging	1	1867757	1867757	4.93	0.035
Error	28	10616596	379164		
Total	29	12484353			

Table 7: ANOVA analysis table for paste G (SAC-Bi).

Analysis of Variance

Source	DF	Adj SS	Adj MS	F-Value	P-Value
Aging	1	139413	139413	0.31	0.584
Error	27	12275369	454643		
Total	28	12414782			

Table 8: ANOVA analysis table for paste H (SAC-Bi-Sb).

Analysis of Variance

Source	DF	Adj SS	Adj MS	F-Value	P-Value
Aging	1	55747	55747	0.22	0.639
Error	26	6452644	248179		
Total	27	6508391			

Table 9: ANOVA analysis table for paste I (SAC-0.5Bi-6.0In).

Analysis of Variance

Source	DF	Adj SS	Adj MS	F-Value	P-Value
Aging	1	283630	283630	1.26	0.270
Error	28	6279999	224286		
Total	29	6563629			

Table 10: ANOVA analysis table for paste J (SAC-Bi).

Analysis of Variance

Source	DF	Adj SS	Adj MS	F-Value	P-Value
Aging	1	2241908	2241908	3.75	0.063
Error	27	16125061	597224		
Total	28	18366970			

Table 11: ANOVA analysis table for paste K (Innolot-H).

Analysis of Variance

Source	DF	Adj SS	Adj MS	F-Value	P-Value
Aging	1	487771	487771	1.98	0.171
Error	27	6667867	246958		
Total	28	7155637			

Table 12: ANOVA analysis table for paste L (SAC++).

Analysis of Variance

Source	DF	Adj SS	Adj MS	F-Value	P-Value
Aging	1	3434689	3434689	5.37	0.028
Error	27	17263835	639401		
Total	28	20698525			

Table 13: ANOVA analysis table for paste M (SAC-Bi-Sb-Co).

Analysis of Variance

Source	DF	Adj SS	Adj MS	F-Value	P-Value
Aging	1	86941	86941	0.70	0.411
Error	28	3499672	124988		
Total	29	3586613			

Table 14: ANOVA analysis table for paste N (SAC++).